SSI-BRIDGE: SOIL-BRIDGE INTERACTION DURING LONG-DURATION EARTHQUAKE MOTIONS

FINAL PROJECT REPORT

by

Andre R. Barbosa, Ph.D.
H. Benjamin Mason, Ph.D.
and
Kyle Romney, M.S.

Oregon State University

for
Pacific Northwest Transportation Consortium (PacTrans)
USDOT University Transportation Center for Federal Region 10
University of Washington
More Hall 112, Box 352700
Seattle, WA 98195-2700

Disclaimer

The contents of this report reflect the views of the authors, who are responsible for the facts and the accuracy of the information presented herein. This document is disseminated under the sponsorship of the U.S. Department of Transportation's University Transportation Centers Program, in the interest of information exchange. The Pacific Northwest Transportation Consortium and the U.S. Government assumes no liability for the contents or use thereof.

Technical Report Documentation Page

1. Report No.	2. Government Accession No.	3. Recipient's Catalog No.
2012-S-OSU-0008	01538103	

4. Title and Subtitle	5. Report Date
SSI-BRIDGE: SOIL-BRIDGE INTERACTION DURING LONG-DURATION EARTHQUAKE	September 15, 2014
	6. Performing Organization Code

7. Author(s)	8. Performing Organization Report No.
Andre R. Barbosa, H. Benjamin Mason, and Kyle Romney	8-739437

9. Performing Organization Name and Address		10. Work Unit No. (TRAIS)
PacTrans Pacific Northwest Transportation Consortium, University Transportation Center for Region 10 University of Washington More Hall 112 Seattle, WA 98195-2700	School of Civil and Construction Engineering Oregon State University 101 Kearney Hall, Corvallis, OR 97331-3271	**11. Contract or Grant No.** DTRT12-UTC10

12. Sponsoring Organization Name and Address	13. Type of Report and Period Covered
United States of America Department of Transportation Research and Innovative Technology Administration	Research 9/1/2012-7/31/2014
	14. Sponsoring Agency Code

15. Supplementary Notes

Report uploaded at www.pacTrans.org

16. Abstract

The seismic response of a complete soil-bridge system during shallow, crustal and subduction zone earthquakes is the topic of this report. Specifically, the effects of earthquake duration on the seismic performance of soil-bridge systems are examined.

This topic is important, because many bridges worldwide are located in tectonic regions characterized by a subducting plate boundary, where high-intensity, long-duration earthquake motions are possible. To date, the effects of earthquake duration are not widely considered during seismic design of bridges. In this report, a model of a soil-bridge system is developed in the finite element framework OpenSees. The soilbridge system is subjected to earthquake motions of varying durations using the direct method. Comparative results show that the number of inelastic excursions in the bridge column and pile increase significantly with earthquake duration, even though other traditional measures of damage such as maximum bending moments and peak column drifts are independent of duration. The results also indicate that the number of inelastic excursions is strongly correlated with earthquake intensity measures that incorporate earthquake duration, such as significant duration, and cumulative absolute velocity. The results imply that earthquake duration needs to be considered when designing and retrofitting bridge superstructures, especially when these are designed to fail in flexure, which is the desired mode of failure in current design methodologies.

17. Key Words	18. Distribution Statement
Seismic response, seismic performance, soil-bridge system	No restrictions.

19. Security Classification (of this report)	20. Security Classification (of this page)	21. No. of Pages	22. Price
Unclassified.	Unclassified.		NA

Form DOT F 1700.7 (8-72) **Reproduction of completed page authorized**

Table of Contents

List of Figures

List of Tables

Acknowledgements

The funding for the research completed in the past year on soil-structure interaction analysis of bridges to long-duration motions is provided by PacTrans small projects grant funded through Oregon State University. Additional support was provided by Oregon State University through start-up funds of the PI. The views and conclusions contained in this document are those of the authors and should not be interpreted as representing official policies, either expressed or implied, of PacTrans or Oregon State University. The authors gratefully acknowledge the financial support of these organizations. Further acknowledgements are available in a Master's thesis produced by the third author, who was funded through the project, which was presented to Oregon State University in June 2013.

Executive Summary

Earthquake engineering analyses are often performed using shallow, crustal earthquake motions (e.g., 1940 El Centro). However, large areas of the world are subject to subduction zone earthquake motions (e.g., the Pacific Northwest, PNW). A subduction zone (SZ) earthquake motion is characterized by its long duration (e.g., strong shaking lasts for more than a minute). Observations of unexpected bridge damage following the recent SZ earthquakes in Chile and Japan highlight the importance of understanding soil-bridge interaction during long-duration earthquake motions. Accordingly, the main objective of this report is to compute the seismic response of a soil-bridge system during long-duration earthquake motions to provide new knowledge to the effects of these types of motions on these systems.

A double span bridge, which was supported on a monoshaft foundation, was considered herein. A nonlinear finite element model of the soil-bridge system was modeled within OpenSees. The pile foundation was modeled using fiber-section elements (representing a reinforced concrete pile), which was attached to a soil continuum. The soil was specified as a dense, non-liquefiable sand. The bridge column was modeled using force-based fiber-section elements attached to the linear elastic bridge deck. Gap-spring elements were used at the ends of the bridge deck to represent abutment backfill response. The soil-bridge system was subjected to seven selected SZ motions and seven selected shallow, crustal motions. For each motion, the number of inelastic excursions was based on the yield rotation. The number of inelastic excursions was plotted against five earthquake intensity measures: peak ground acceleration (PGA), cumulative absolute velocity (CAV), significant duration (D_{5-95}), Arias intensity (I_A), and spectral acceleration (S_a).

Results show a definite distinction between the two types of earthquake motions and long-duration earthquake motions are more damaging to soil-bridge systems than shallow, crustal earthquake motions with similar amplitudes and frequency contents because of the

increased number of cycles of loading. Results of this study highlight the importance of considering SSI in the analysis of PNW bridges due to the effects of duration on soil-bridge systems when subjected to SZ ground motions. In its totality the report presents significant advancement to the knowledge for analysis of soil-structure systems subjected to long-duration motions, which has significant implications for improving seismic resiliency plans in the PNW.

Chapter 1 Introduction

1.1 Problem Statement

Transportation systems serve as lifelines in the aftermath of a disastrous earthquake event. Within these transportation systems, bridges are key components to a successful system. Along the Oregon coast, and throughout the Pacific Northwest (PNW), there are many bridges that are crucial to the delivery of relief to coastal cities and towns. Recognizing this fact, the PNW departments of transportation are leading efforts to address seismic mitigation of lifeline bridges to avoid catastrophic failures similar to Figure 1.1. In the PNW, bridge designers have only considered subduction zone earthquake motions, specifically the Cascadia Subduction Zone, during seismic bridge design for just over 20 years. However, a large number of bridges were built before 1990. As a result, in the past two decades, considerable effort has gone into the evaluation of effects of PNW earthquakes, on existing bridge stock.

Recent earthquakes in Chile and Japan have shown the destructive power of subduction zone events. These earthquakes have provided invaluable amounts of ground motion data and research motivation. The main objective of this report is to highlight the importance of soil-structure interaction (SSI) on the seismic response of critical infrastructure, such as bridges, to long-duration, large intensity, subduction zone earthquakes. Understanding SSI effects due to subduction zone events will allow engineers, and specifically engineers in the PNW, to devise retrofit strategies for our current infrastructure and design our future infrastructure effectively.

To evaluate the SSI effects on the seismic response of bridges due to subduction zone earthquakes, a two-dimensional finite element (FE) model of a soil-foundation-bridge (SFB) system was subjected to multiple subduction zone and shallow, crustal earthquake motions. Significant research has been conducted on the seismic response of bridges due to near-

Figure 1.1 Failed bridge column due to the 1994 Northridge, California shallow, crustal earthquake (ACE-MRL, 2013).

fault shallow, crustal earthquake motions (Somerville et al., 1997) due to their dominance in California. Comparison of the SSI effects on the soil-foundation-bridge system due to both shallow, crustal and subduction zone earthquake motions will provide important information to better understand the demands placed upon current infrastructure.

Specific to the PNW, this research topic is the first of its kind in Oregon and is an important step in understanding the effects of a Cascadia Subduction Zone earthquake for the entire PNW.

1.2 Overview

The research presented in this report includes a review of current literature on the topic of SSI related to bridges. The literature review is followed by the methodology chapter which presents the earthquake motion selection method, soil and structural models used,

and the analyses performed. The results are presented, along with their respective conclusions, in the final two chapters to conclude this research. Appendices are included to provide the scripts used for model development and analysis, post-processing of the output response parameters, and model validation for the proposed soil-foundation-bridge system.

Chapter 2 Literature Review

Consideration of soil-structure interaction (SSI) effects has become increasingly important when determining the seismic response of bridges. Considering SSI effects allows researchers and practicing engineers to design more seismically resilient bridges. In particular, the consideration of SSI effects on soil-bridge systems subjected to long-duration earthquake motions (i.e. earthquake motions created by a mega-thrust event on the Cascadia Subduction Zone) has become a viable research topic. In this chapter, a literature review of SSI is presented. Soil-bridge interaction is a specific focus. In addition, important earthquake motion intensity measures are defined. The literature review is not exhaustive, but focuses on important work for developing this study. For interested readers, Kausel (2010) presents a history of SSI research.

2.1 Earthquake Motion Intensity Measures

There are multiple earthquake motion intensity measures used by engineers to describe the characteristics of earthquake motions (Kramer, 1996). In this study, the five earthquake motion intensity measures that will be discussed are: peak ground acceleration (PGA), pseudo-spectral acceleration (S_a), cumulative absolute velocity (CAV), Arias Intensity (I_A), and significant duration (D_{5-95}). Each earthquake motion intensity measure is used to characterize input earthquake motions and correlate damage due to the effects of earthquake motion duration.

Peak ground acceleration is defined as the peak absolute acceleration value for a given earthquake motion and is the most commonly used earthquake motion measure of amplitude (Kramer, 1996). PGA has been correlated by a number of authors to earthquake intensity (Trifunac and Brady, 1975; Murphy and O'Brien, 1977; Krinitzsky and Chang, 1987). The spectral accelerations are obtained from a response spectrum, which describes the peak response quantity (acceleration, velocity, and displacement) of a single-degree-of-

freedom system as a function of the natural vibration period of the system (Chopra, 2012). In this study, focus will be placed on the pseudo-spectral acceleration at the fundamental period of the examined soil-foundation-bridge system. Cumulative absolute velocity is found by computing the area under the absolute acceleration-time series, as shown below in Equation 2.1, and has been found to correlate well with damage (Kramer, 1996). Arias Intensity is the integration over the entire acceleration-time series (Arias, 1970), shown in Equation 2.2, and therefore, is a universal measure of duration (Kramer, 1996).

$$CAV = \int_0^{T_d} |a(t)|dt \tag{2.1}$$

$$I_A = \frac{\pi}{2g} \int_0^{\infty} [a(t)]^2 dt \tag{2.2}$$

Significant duration, in this study, is defined by Trifunac and Brady (1975) as the time interval between 5% and 95% of the total recorded energy calculated from Arias Intensity. The duration of strong ground motion is a function of the rupture length and time required to release strain energy. The larger the rupture length, the larger the rupture time (Kramer, 1996).

2.2 Soil-structure interaction

Soil-structure interaction (SSI) effects need to be considered in to effectively predict soil-bridge system response. For simplicity, in seismic structural analysis, it is common for engineers to assume a fixed-base condition (Figure 2.1). In many cases, the fixed-base condition does not reflect reality. Bridge superstructures are supported by foundations. The soil surrounding the foundation is compliant and thus, allows rotation and/or translation — this is usually referred to as a flexible-base condition. Accordingly, the typically used fixed-base assumption neglects the effects of SSI, whereas the flexible-base assumption includes

the effects of SSI.

Mylonakis and Gazetas (2000) examined the difference between fixed-base structures and flexible-base structures. An example of the two types of structures is shown in Figure 2.1. The two structures have different vibrational characteristics and therefore different seismic responses. For the flexible-base structure, the soil-foundation interface is deformable; accordingly, the fundamental period, $\tilde{T}$, of the flexible-base structure is longer and its damping ratio, $\tilde{\beta}$, is greater compared to the same parameters for the corresponding fixed-base structure.

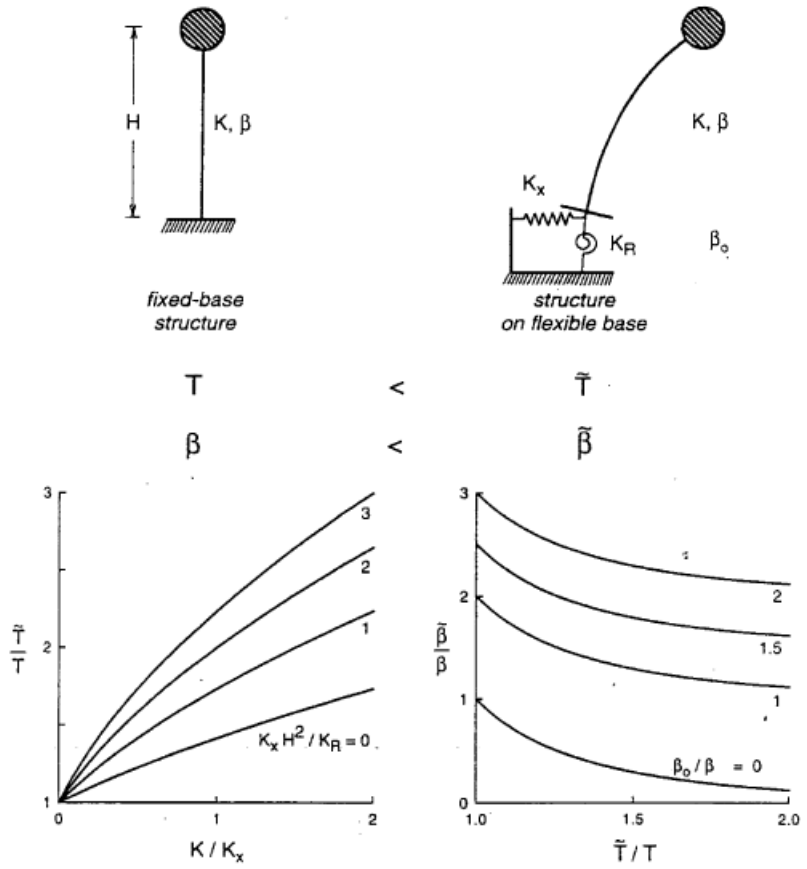

Figure 2.1 Effect of soil-structure interaction (SSI) on fundamental period and damping ratio of a structure on flexible foundation according to NEHRP-97 provisions (Mylonakis and Gazetas, 2000).

Figure 2.2 depicts a general idealized smooth design response spectrum commonly produced in accordance with seismic codes. When considering the effects of SSI, (e.g. the increase in fundamental period and effective damping), the accelerations and stresses within the structure and foundation are generally smaller, which is depicted by the dashed line in Figure 2.2.

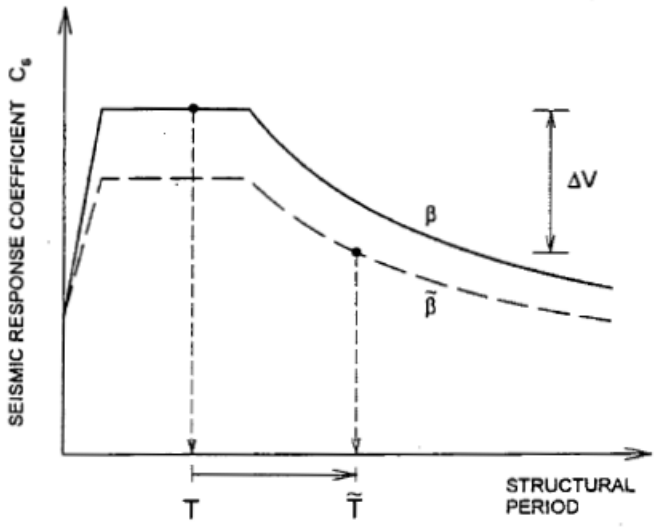

Figure 2.2 Reduction in design base shear due to soil-structure interaction according to NEHRP-97 seismic code (Mylonakis and Gazetas, 2000).

Although the statement above is true for many structures and seismic environments, there are multiple documented case histories that have proved this not to be the case. Mylonakis and Gazetas (2000) documented a case history in Kobe, Japan following the 1995 Kobe earthquake where an elevated highway (the Hanshin Expressway) failed catastrophically during the earthquake because SSI effects were not considered during the design. After examining the details of this case history, Mylonakis and Gazetas (2000) concluded that "as a result of soil or seismological factors, an increase in the fundamental period due to SSI may lead to increased response (despite a possible increase in damping), which contradicts the expectation incited by the conventional design spectrum (pg. 238)."

SSI effects were particularly evident in the 1986 Mexico City earthquake (e.g., Seed et al., 1988; Resendiz and Roesset, 1987). Buildings 10- to 12-stories tall (building height group most damaged), founded on soft soil, experienced an increase in period by roughly double the period of the fixed-base assumption (1.0 second). It should be noted that relatively tall and rigid buildings, constructed on soft soil, commonly experience an increase in natural period, approximately 1.25, due to SSI effects (Mylonakis and Gazetas, 2000). Therefore, careful assessment of earthquake motion inputs and soil conditions is required to obtain the true response and not the conventional response.

2.3 Soil-bridge interaction

2.3.1 Importance of soil-bridge interaction

Figure 2.3 shows a simple structural idealization of a single bridge pier connected 1) monolithically to the bridge deck and 2) with an array of nonlinear translational and rotational soil springs. It is assumed that the bridge system in Figure 2.3 is subjected to a horizontal ground motion. Using this idealization, the inelastic response and SSI effects of the system can be analyzed. The following equation can be used to describe the lateral displacement, $\tilde{U}$, of the deck relative to the far-field soil (Mylonakis and Gazetas, 2000):

$$\tilde{U} = \Delta_f + \theta_f H + \Delta_y + \Delta_p \tag{2.3}$$

where Δ_f and $\theta_f \times H$ represent the rigid body displacements of the deck due to swaying (Δ_f) and rocking (θ_f) of the foundation, Δ_y is the yield displacement of the pier, and Δ_p is the plastic displacement of the pier due to yielding concentrated at the base of the column (i.e. plastic hinge).

From the lateral displacement equation (2.3), the relationship for the ductility capacity of the column, μ_c, and ductility demand of the SSI system, μ_s, is derived (assuming elastic

perfectly plastic pier) as:

$$\mu_s = \frac{c + \mu_c}{c + 1} \tag{2.4}$$

where,

$$c = \frac{\Delta_f + \theta_f H}{\Delta_y} \tag{2.5}$$

and where the dimensionless coefficient, c, describes the foundation to structure displacement.

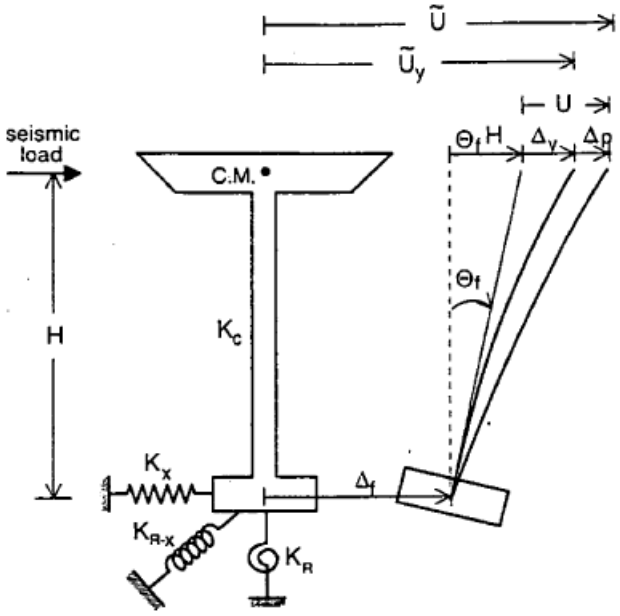

Figure 2.3 The model used to investigate the significance of SSI in the inelastic seismic performance of cantilever bridge piers (Mylonakis and Gazetas, 2000).

Plotting the ductility demand of the SSI system, μ_s, as a function of the ductility capacity of the column, μ_c, for different values of the foundation to structure displacement coefficient, c, yields Figure 2.4. For the fixed-base assumption ($c = 0$), the slope of the line is 1 to 1 meaning $\mu_s = \mu_c$. Furthermore, for all cases where $c > 0$, μ_s is always less than μ_c, interpreted that for a given ductility capacity of the column, μ_c, ($\mu_c > 1$), the ductility

capacity of the SSI system, μ_s, is less than the ductility capacity of the fixed-base cantilever [Priestley and Park (1987); Ciampoli and Pinto (1995)].

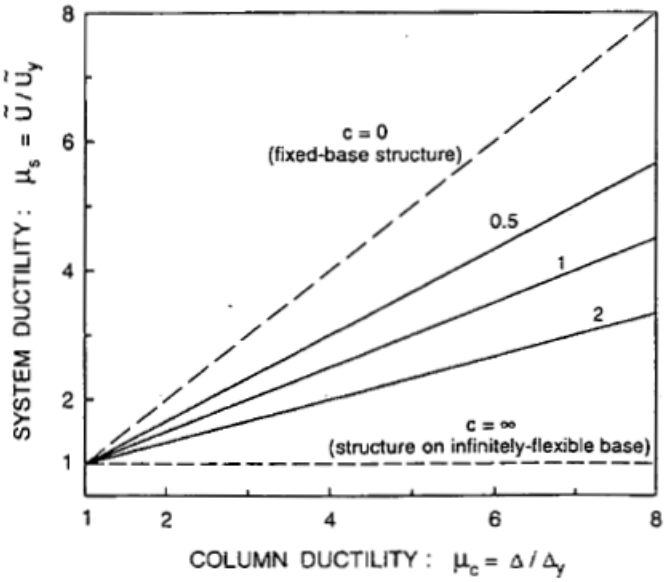

Figure 2.4 Relation between pier ductility, μ_c, and SSI system ductility, μ_s, for a bridge model (perfectly elastic plastic pier column behavior) (Mylonakis and Gazetas, 2000).

From another perspective, to attain a desired ductility capacity of a system for $c > 0$, a significant increase in deformation may be required. As a conclusion to the above statement, Mylonakis and Gazetas (2000) concluded that "soil-structure interaction has a detrimental effect on the inelastic performance of a bridge-foundation system by reducing its ductility capacity. Strictly speaking, the changes in both capacity and demand should be considered to conclude whether SSIs role in beneficial or detrimental. Nevertheless, the reduction in ductility capacity suggested by Eq. 2.4 is obviously detrimental." This conclusion contradicts the traditionally-thought beneficial role SSI effects has on a system.

The above conclusions were drawn from inelastic static analyses. From a dynamic analysis perspective, Mylonakis and Gazetas (2000) reviewed a similar investigation performed

Table 2.1 Differences in analysis assumptions between the Ciampoli and Pinto (1995) and Mylonakis and Gazetas (2000) studies.

	Ciampoli and Pinto (1995)	Mylonakis and Gazetas (2000)
EQ Motion	Artificial	Actual
Soil Type	Intermediate	Soft
DOF System	Single DOF	Two DOF

by Ciampoli and Pinto (1995) and modified some of their methods to more closely match a realistic system. The differences are shown below in Table 2.1.

The results presented by Mylonakis and Gazetas (2000), in this section, were obtained applying the 1997 Bucharest Brancea earthquake motion. Figure 2.5 illustrates the column ductility demands as a function of fixed structural period, T, for four different foundation-to-structure flexibility ratios: c = 0 (fixed-base), 0.25, 0.5, and 1.0. It should be noted that when c = 1 the fixed-base structural period of the flexibly-supported system is $\sqrt{1+c} = 1.4$ times larger than that of the equivalent fixed-base system. It is apparent that the SSI effects increase the ductility demand in the bridge pier in the period range of 0.5 to 1.5 seconds and decrease the ductility demand in the bridge pier at longer periods.

Comparing the system ductility demand to the pier ductility demands, it is apparent in Figure 2.6 that the SSI effects are nearly negligible and would not indicate any reason to believe that SSI is detrimental. When only considering the system ductility demand, it would appear harmless to neglect SSI, especially at longer periods, where the demand is decreased dramatically. Conversely, it is apparent that the SSI effects increase the ductility demand in the bridge pier and should therefore not be neglected.

2.3.2 Previous soil-bridge interaction models

Shamsabadi et al. (2007) developed a 3D nonlinear dynamic bridge model to analyze two abutment backfill soil hyperbolic models. Two earthquake motions, with a strong velocity pulse, were used to analyze the bridge model: 1994 Northridge, California, Rinaldi

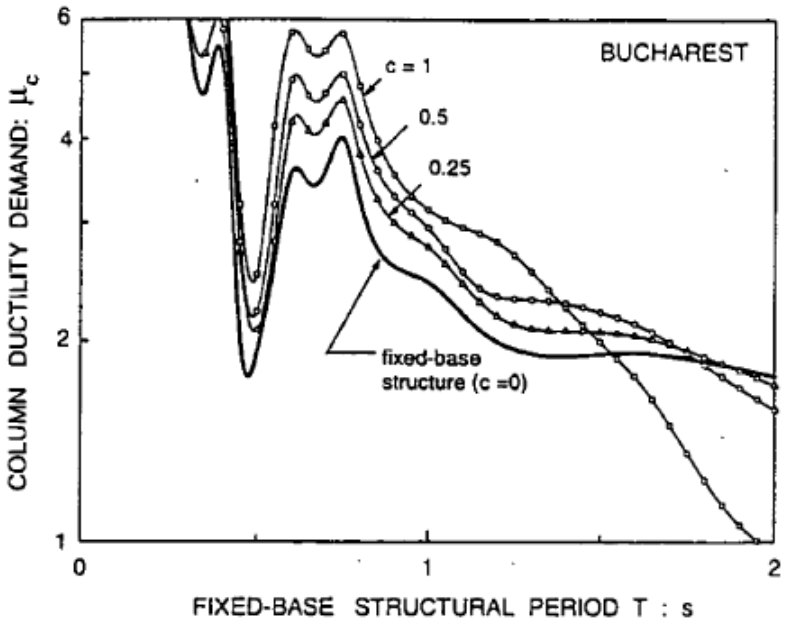

Figure 2.5 SSI effects on the ductility demand of a bridge pier subjected to the Bucharest (1977) N-S motion; R = 2 (Mylonakis and Gazetas, 2000).

Station and 2005 Kobe, Japan, Takarazu Station.

The bridge deck dimensions and backfill soil properties were used as a reference to develop the bridge deck and backfill soil properties for model development and analysis in this study. A schematic of the 3D bridge model, developed in SAP 2000, is shown in Figure 2.7.

Shamsabadi et al. (2007) conclude that the resistance of the abutment backfill soil has a significant influence on the maximum displacement of the bridge superstructure. Therefore, realistic seismic bridge response for performance-based bridge design, analysis requires the analysis of bridge abutments.

Zhang et al. (2008) developed a 2D advanced nonlinear finite-element model of the Humboldt Bay Middle Channel (HBMC) Bridge, as shown in Figure 2.8, in the finite element (FE) program OpenSees, to evaluate the seismic response of bridges including the

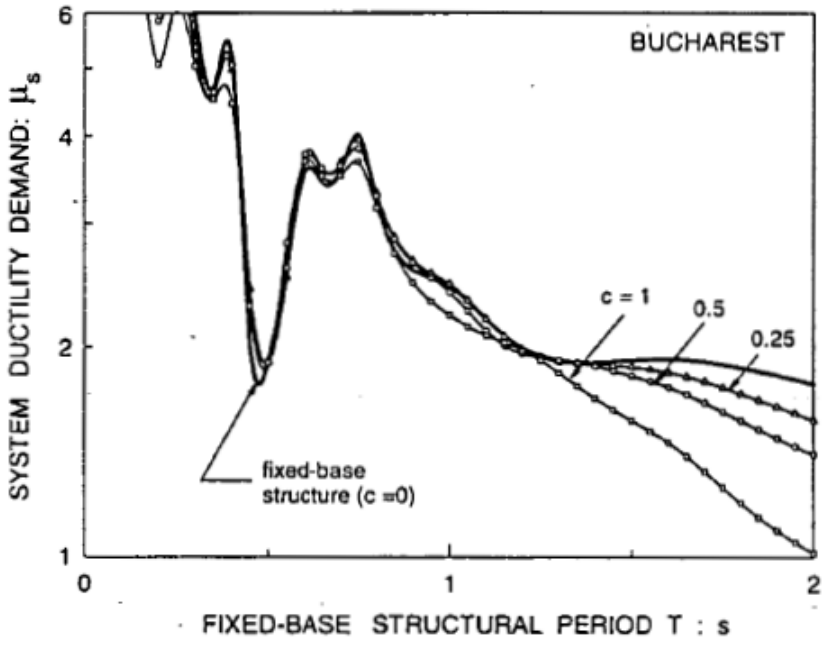

Figure 2.6 SSI effects on the system ductility demand of a bridge pier subjected to the Bucharest (1977) N-S motion; R = 2. Note the reduced values and differences in spread compared to Figure 2.5 (Mylonakis and Gazetas, 2000).

effects of soil-structure interaction (SSI). The FE model includes the structure, pile group foundations, approach embankments, and foundation soil.

The HBMC Bridge superstructure consists of precast pre-stressed concrete I-girders and cast-in-place concrete slabs, supported by eight bents founded on pile group foundations. The foundation soil varies from soft organic silt with clay to dense alluvial deposits, as shown in Figure 2.9. The inclusion of the foundation soil, modeled using multi-yield-surface plasticity models (Elgamal et al., 2002) that assimilate the effects of liquefaction, captures the response due to SSI. Boundary conditions were set to resemble the response of a shear soil column (i.e. shear beam assumption) and to only consider the horizontal accelerations, velocities, and displacements (i.e. the vertical component of a given simulated nonlinear soil response remains negligible compared to the horizontal component). The soil was discretized by four-node, bi-linear, isoparametric elements. The superstructure

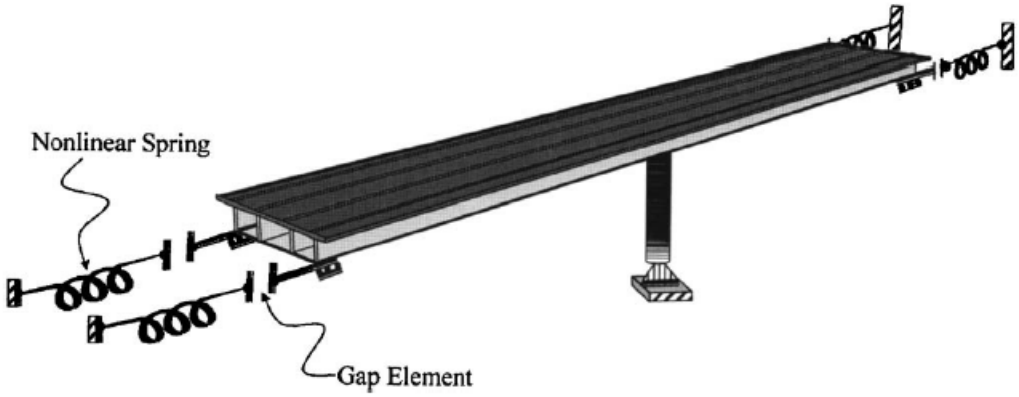

Figure 2.7 Schematic of the double span 3D bridge model developed in SAP 2000 (Shamsabadi et al., 2007)

Figure 2.8 View from shoreline of the Humboldt Bay Middle Channel Bridge (courtesy of California Department of Transportation (Caltrans, 2000)).

(abutments and girders) were modeled using linear elastic beam-column elements. The bridge piers were modeled using fiber-section beam-column elements. The pile foundations and pile caps were modeled using force-based, fiber-section beam-column elements. The final bridge-foundation-ground OpenSees model used by Zhang et al. (2008) is shown in Figure 2.9.

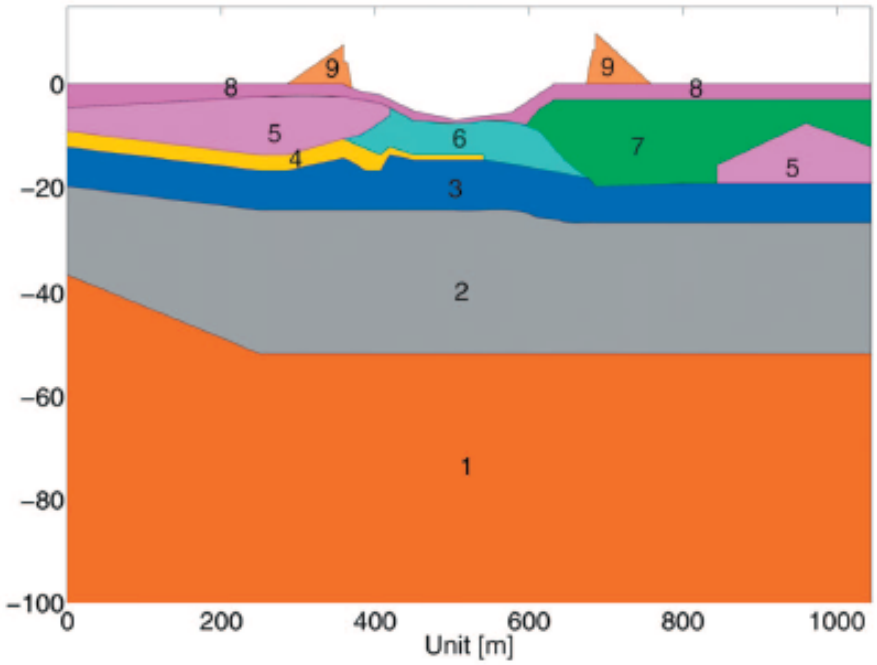

Figure 2.9 Two-dimensional soil profile of HBMC Bridge site (layer 1: Tertiary and Quaternary Alluvial deposits; layer 2: medium dense organic silt, sandy silt and stiff silty clay; layer 3: dense sand; layer 4: silt; layer 5: medium dense to dense silty sand and sand with some organic matter; layer 6: dense silty sand and sand; layer 7: soft or loose sandy silt or silty sand with organic matter; layer 8: soft to very soft organic silt with clay; and layer 9: abutment fill (Zhang et al., 2008).

Based on the simulation results, Zhang et al. (2008) concluded that the response of the bridge superstructure is significantly affected by inelastic deformations of the supporting soil. These findings coincide with other analytical studies that have been performed by a number of researchers that have shown, for short-span overpass bridges, that the seismic

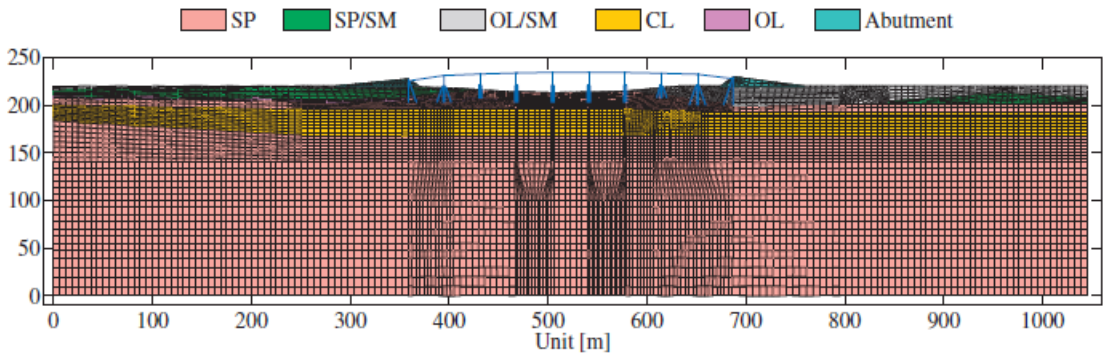

Figure 2.10 OpenSees finite element model of bridge-foundation-ground system (Zhang et al., 2008).

response of the bridge superstructure is integrated with the response of the abutments and embankment soil and is largely influenced by the response of the soil foundation (Werner et al., 1987, 1990, 1994; Wilson and Tan, 1990a,b).

Aygün et al. (2010) developed new fragility relationships that capture the conditional probability of coupled bridge-soil-foundation (CBSF) system components to reach or exceed predefined performance levels as a function of earthquake hazard intensity and liquefaction potential for the central and eastern United States. The CBSF system included 3D bridge components and 2D soil foundation connected by 1D p-y soil springs, as shown in Figure 2.11. The finite element bridge system was modeled in OpenSees as a multi-span continuous steel girder bridge.

Based on regional empirical information, five idealized soil profiles and three foundation types were used to construct the finite element models with realistic structural details and soil profile data. The structural elements used in the CBSF model are (Neuenhofer and Filippou, 1998): a) nonlinear beam-column elements with distributed plasticity fiber sections for the piles and columns and b) linear elastic beam-column elements for the bridge deck. The soil was modeled using the pressure dependent multi yield material for sand and pressure independent multi yield material for clay (Zhang et al., 2003). To simulate a sat-

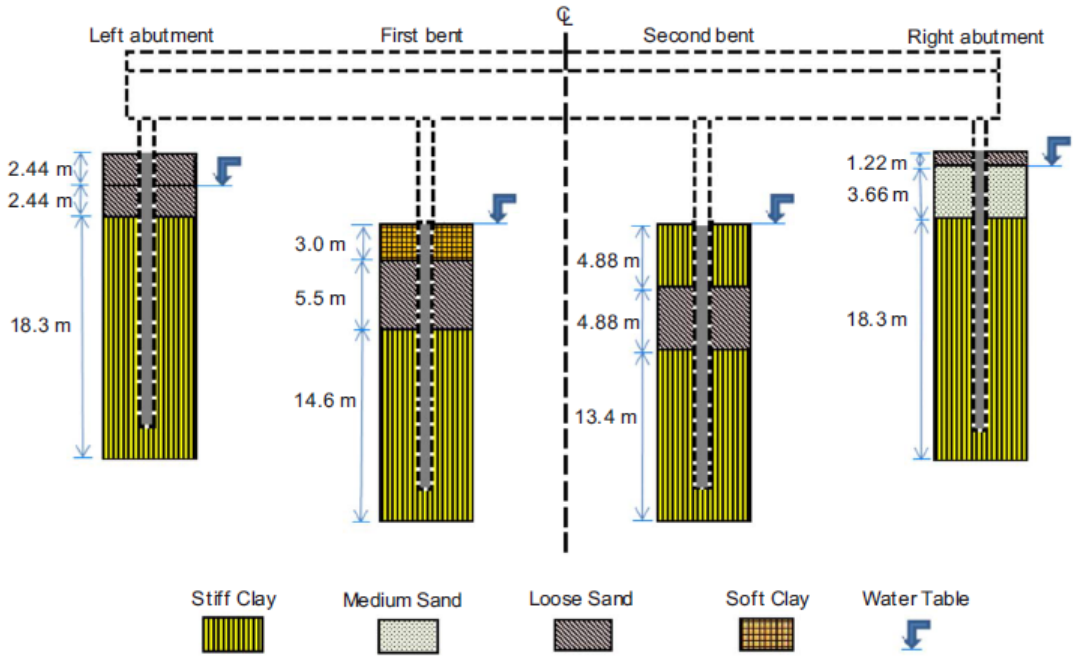

Figure 2.11 Schematic of one of the coupled bridge-soil-foundation systems developed by Aygün et al. (2010).

urated and undrained state both soil material types were embedded in a fluid solid porous material (Zhang et al., 2003). The width of bridge deck was used for the out-of-plane thickness of the 2D soil column based on past soil-structure interaction research conducted by Zhang et al. (2008); Bowers (2007); Aygün et al. (2010). The soil column and pile were connected using 1D nonlinear p-y soil springs, which were calibrated based on centrifuge tests performed by Boulanger et al. (1999). The p-y soil springs were modeled in OpenSees using the PySimple1 material for non-liquefiable soil and PyLiq1 material for liquefiable soil (Boulanger et al., 1999). Figure 2.12 illustrates the finite element model developed in OpenSees with the various structural and soil components. Aygün et al. (2010) used a synthetic rock outcrop accelerogram to simulate shallow, crustal-type earthquake events, developed by Andrus et al. (2006) for Charleston, South Carolina, to determine the seismic response of the CBSF system.

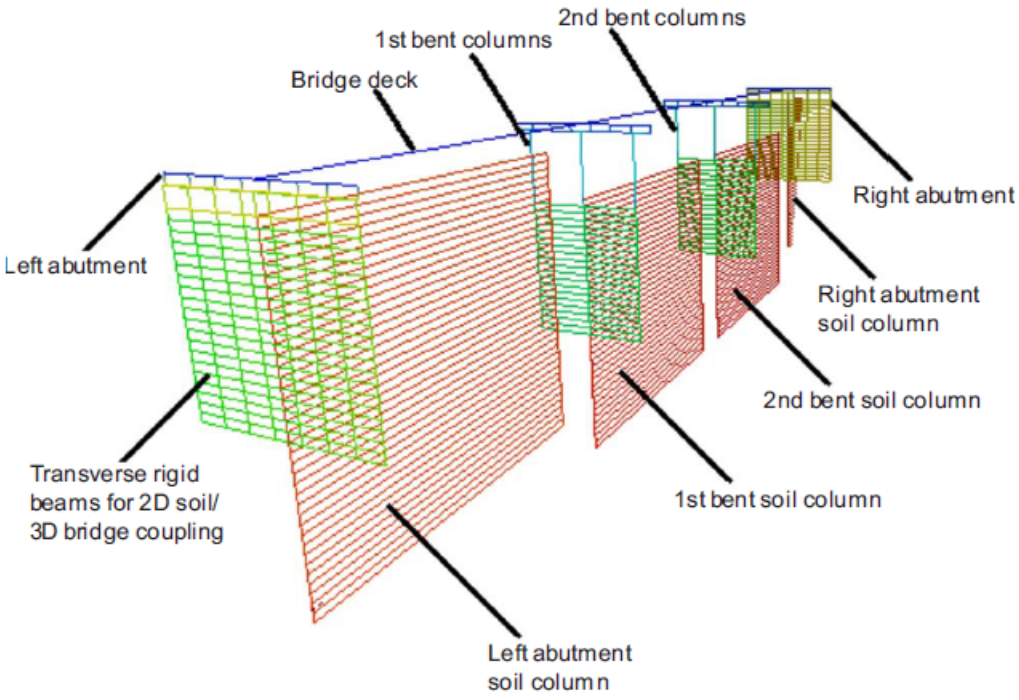

Figure 2.12 Finite element model for the coupled bridge-soil-foundation system developed by Aygün et al. (2010). The 3D bridge structure (pile, column, and deck) and 2D soil mesh are connected by 1D soil spring (not visible).

The results of the Aygün et al. (2010) study demonstrate the importance of incorporating the effects of soil-structure interaction on the seismic response of the CBSF system (3D bridge-foundation system with 2D soil mesh connected by 1D p-y soil springs) and provided an efficient and adequate framework to evaluate bridge failure mechanisms. Using this approach of developing a detailed probabilistic analyses of a given soil-bridge system allows users to efficiently determine the seismic hazard and incorporate the system fragility into future network reliability studies.

Khosravifar (2012) developed a 2D finite element model in OpenSees to evaluate the effects of lateral spreading and liquefaction on the inelastic structural response of extended pile shaft foundations. Figure 2.13 illustrates the various components of the soil-structure finite element model.

The soil-structure system incorporates a single nonlinear pile shaft foundation, single nonlinear bridge column, bridge deck, and a layered, nonlinear soil column connected to the pile by horizontal, vertical, and end bearing soil springs. It should be noted that Khosravifar (2012) was specifically evaluating the pile response in the transverse direction and a parametric study was conducted to determine the system sensitivity to various parameters.

The soil column consisted of three different soil layers: 1) clay crust, 2) loose liquefiable sand, and 3) dense sand. The soil column was modeled in OpenSees using 9-4 Quad UP elements (Elgamal et al., 2002) and used the pressure dependent multi yield02 and pressure independent multi yield materials to define the constitutive models for sand and clay, respectively (Elgamal et al., 2002). The soil column was constrained in OpenSees to remain in a state of plane strain and to produce pure shear behavior. The selected out-of-plane thickness was chosen to be large enough to remove the pile kinematic effects on the soil column. The Type 1 reinforced concrete pile shaft and column section were modeled in OpenSees using flexibility-based nonlinear beam-column elements. The confined and unconfined concrete stress-strain behavior were modeled after Mander et al. (1988). The

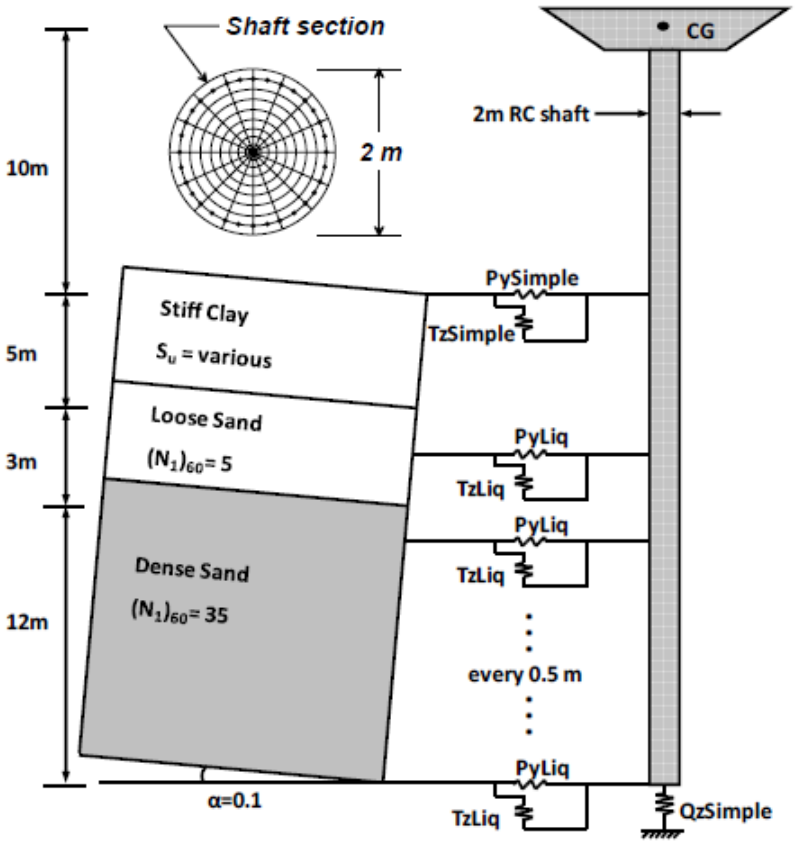

Figure 2.13 Illustration of the 2D FE model developed by Khosravifar (2012) to determine the response of the pile due to the effects of lateral spreading and liquefaction.

capacity of the shaft was determined by performing a moment-curvature analysis and was defined by crushing in the confined concrete or snapping of the reinforcing steel. The pile and column have the same cross-sectional properties with similar plastic moment capacities. The column-deck connection was modeled as a free and fixed connection. The bridge deck was modeled as a lumped mass system. The soil column and pile were connected using 1D horizontal (p-y), vertical (t-z), and end bearing (q-z) soil springs to model the pile-soil interface. Materials PyLiq1 and TzLiq1 were used to model the behavior of the horizontal and vertical soil springs, respectively in sand and PySimple1 and TzSimple1 in clay (Boulanger et al., 1999). Soil spring parameters were selected based on recommendations from API (1993). The horizontal soil spring stiffness was modified with depth after Boulanger et al. (1999). Forty earthquake motions (Baker et al., 2011) were selected based on magnitude, source-to-site distance, shear wave velocity, and earthquake mechanism.

The FE model was analyzed in OpenSees using a phased analysis procedure to simulate pre- and post-construction conditions. First, a gravity load (self-weight) was applied to the soil column to simulate hydrostatic pore water pressure, initial effective stress, and K_o conditions. Second, the pile and soil column were then connected by the soil springs. Third, a gravity load (self-weight) was applied to the bridge deck, column, and pile. Lastly, the nonlinear dynamic analysis was performed by shaking the system with an input excitation.

The results of the Khosravifar (2012) study, although largely related to the effects of lateral spreading and liquefaction, highlight the effects of soil-structure interaction on the seismic response of soil-bridge system.

Chiaramonte (2011) developed a series of analytical 2D finite element models, in OpenSees, of a pile supported wharf structure in Oakland, California. The structure consists of a reinforced concrete deck supported by pre-stressed concrete piles. Figures 2.14 and 2.15 illustrate the various structural and soil components and the plan and elevation views of the wharf structure.

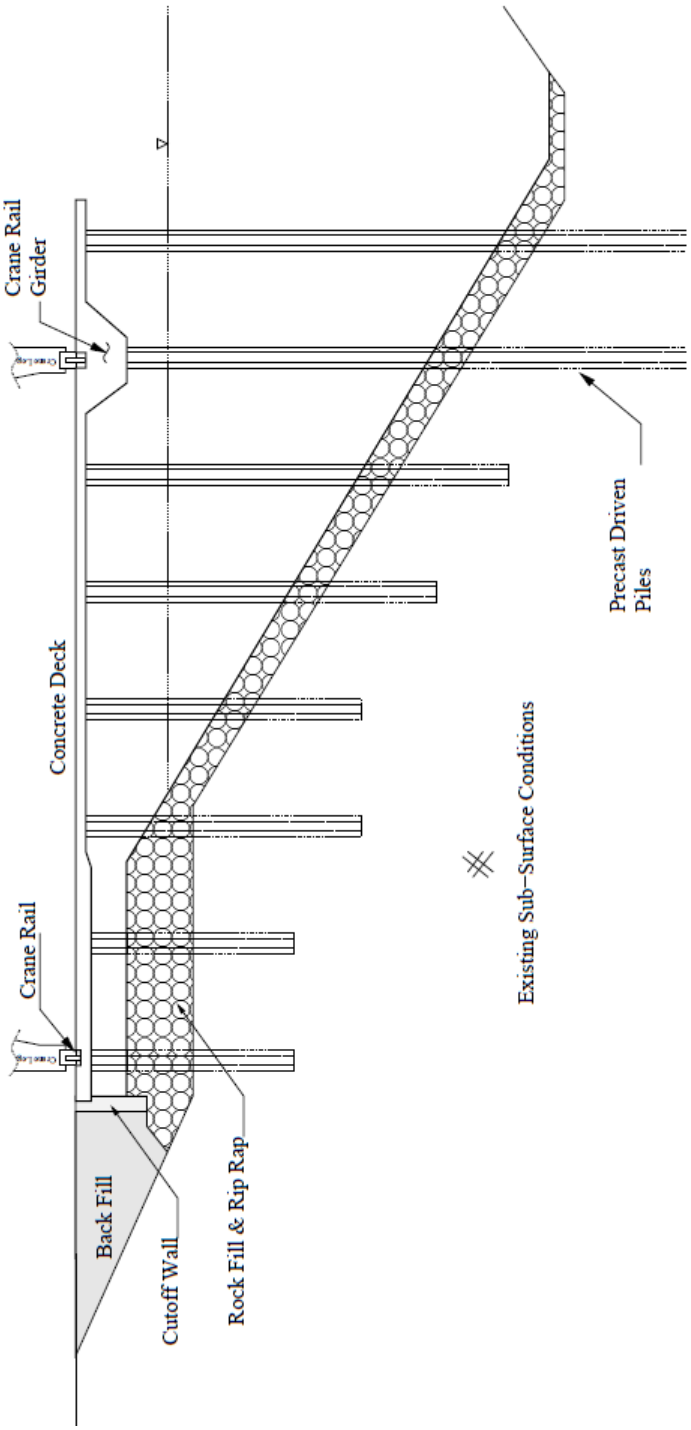

Figure 2.14 Schematic of the marginal wharf structure (Chiaramonte, 2011).

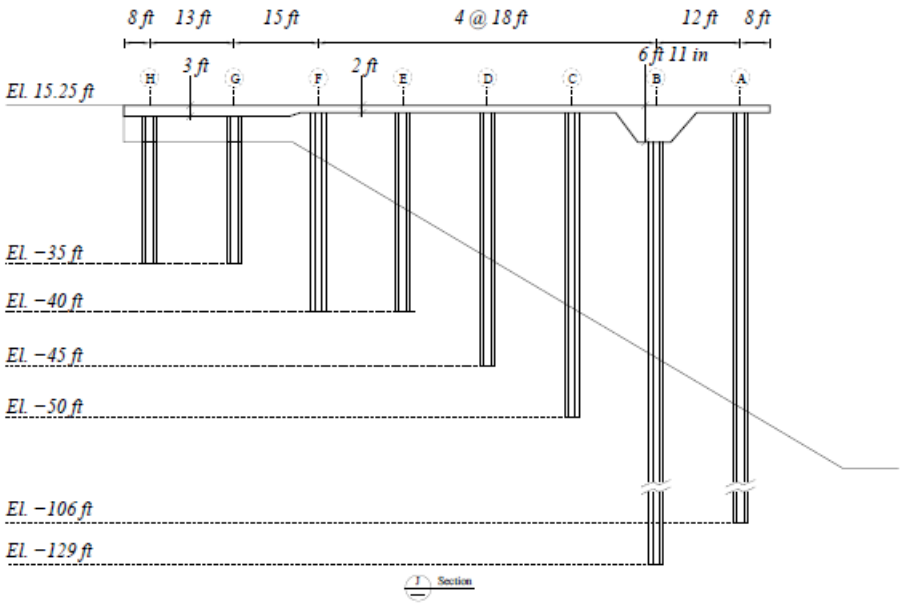

(a) Elevation (Not to scale)

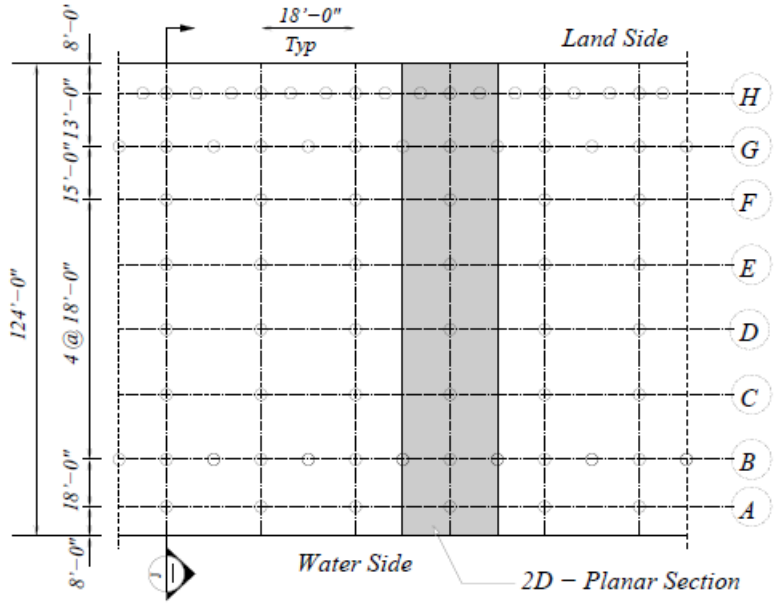

(b) Plan View (Not to scale)

Figure 2.15 Plan (a) and elevation (b) views of the marginal wharf structure (Chiaramonte, 2011).

The wharf deck was modeled in OpenSees as a rigid elastic beam-column element (with rigid offset) and was connected to the pile supports. Nonlinear distributed plasticity force-based beam-column elements (Neuenhofer and Filippou, 1998), discretized with 1 ft elements, were used to represent the piles. The fiber section pile cross-section consisted of unconfined and confined concrete and pre-stressed and mild steel reinforcing bars. The constitutive models used for both confined and unconfined concrete were Concrete02 material (Mander et al., 1988). Steel02 was used to define the constitutive model for both the mild and pre-stressed steel reinforcement (Filippou et al., 1983).

The soil continuum was modeled to represent existing soil conditions to a depth of bedrock. The soil mesh was modeled in OpenSees using quadrilateral elements in a two degree of freedom domain with four integration points (Zhang et al., 2003). Figure 2.16 illustrates the final soil mesh used in the analysis. The soil mesh grid size was determined based on the shear wave velocity of the softest material. To prevent important frequencies being filtered out during analysis, a maximum frequency, f_{max}, of 40 Hz was used. The soil column elements were constrained in horizontal and vertical directions to capture only the shear wave propagation and prevent any unrealistic distortion of the soil column section. Pressure Dependent Multi Yield02 and Pressure Independent Multi Yield materials were used to define the constitutive behavior of the granular and cohesive soil types, respectively.

To capture the effects of soil-structure interaction, nonlinear soil-interface springs were used. Horizontal (p-y), vertical (t-z), and end bearing (q-z) soil-interface springs were modeled in OpenSees using PySimple1, TzSimple1, and QzSimple1, respectively (Boulanger et al., 1999). The capacity and stiffness of the p-y soil springs were defined based on the recommendations of API (1993) for sand and Matlock (1970) for clay. The response of the vertical (t-z) soil springs was defined after Mosher (1984) for sand and Reese and O'Neill (1975) for clay. Similarly, the end bearing (q-z) soil spring was defined after Vijayvergiya (1977) for sand and Reese and O'Neill (1975) for clay.

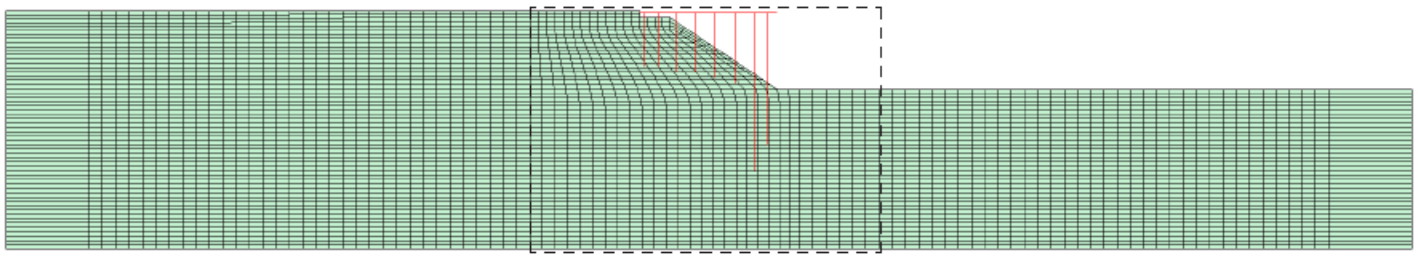

(a) Full finite element mesh

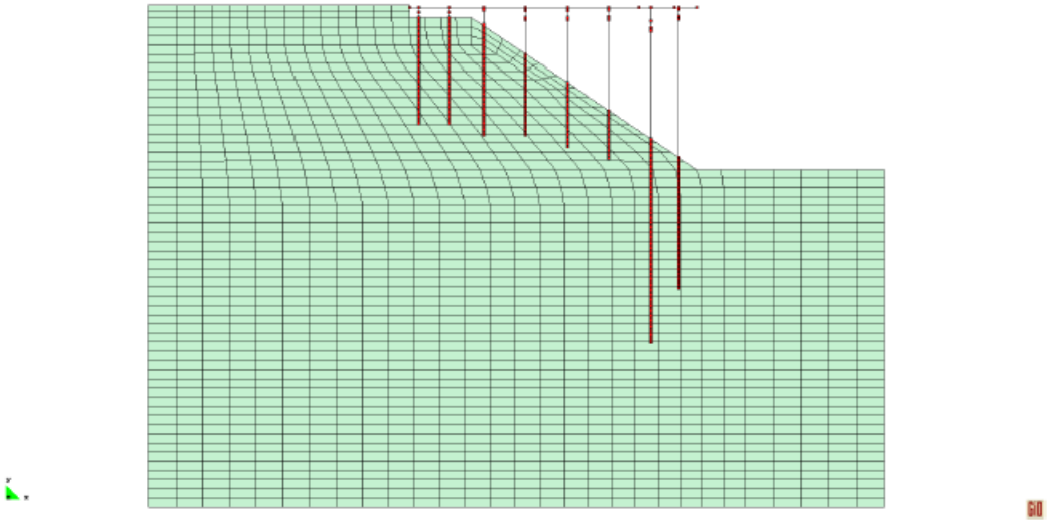

(b) Slope finite element mesh enlargement

Figure 2.16 Schematic of the final model used in the analysis (Chiaramonte, 2011).

Thirteen earthquake motions were selected from the Next-Generation Attenuation of Ground Motions (NGA) project (Power et al., 2008) based on magnitude, closest distance to rupture, shear wave velocity, peak ground acceleration (PGA), and earthquake mechanism. The vertical component of all earthquake motions were neglected and only the horizontal component with the largest PGA was used. Three target spectra were developed for a 2% in 50 year event, a 5% in 50 year event, and a 10% in 50 year event. Each earthquake motion was linearly scaled over a range of $0.2T_n$ to $1.5T_n$.

Chiaramonte (2011) followed a series of steps to avoid introducing fictitious forces into the system before the application of gravity loads and then the dynamic forces. The following steps were:

1. The pile elements are created and fixed at their base and analyzed statically so that pile shortening from pre-stress can be freely accommodated.

2. The pile constraints are removed.

3. The deck elements and soil springs are created and connected. The springs' slave nodes are fixed in all of their degrees of freedom at this time.

4. The soil mesh is then generated and not yet connected to the soil springs.

5. Elastic static gravity analysis is conducted to obtain confining pressures for the non-cohesive soils.

6. The soil material state is then updated to inelastic and a few dynamic analysis steps are conducted to accommodate the values of the internal variable.

7. The springs slave node constraints are removed and the nodes are connected to the closest soil mesh node.

Comparing the results from static pushover analysis (no soil column) and thirteen dynamic analyses indicate the effects of soil-structure interaction.

Although various components from each the authors presented in this literature review chapter were used to develop the methodology and finite element model discussed hereafter in this report, the effects of earthquake motion duration was not considered in any of the aforementioned references. The objective of this report is to show how long-duration earthquakes effect the seismic response of a soil-bridge system.

Chapter 3 Methodology

3.1 Introduction

This study focuses on the seismic response of soil-foundation-bridge systems subjected to long-duration earthquake motions. Development of the two-dimensional (2-D) finite element (FE) model and all analyses coinciding with this research were performed using the Open System for Earthquake Engineering Simulations finite element framework, more commonly referred to as OpenSees (McKenna et al., 2000). Users can model structural and geotechnical problems using the OpenSees framework. Accordingly, OpenSees is particularly useful for examining SSI problems.

A structural model of a double-span reinforced concrete bridge and foundation, connected to a nonlinear soil column by nonlinear soil springs, was subjected to seven shallow, crustal earthquake motions and seven subduction zone earthquake motions. The foundation system corresponds to a Caltrans Type-I (Caltrans, 2006) shaft and is an example of a column-pile section that is built with the same diameter and concrete cover. A model of this soil-foundation-bridge system is developed in OpenSees. The modeling approach involves a 2-D nonlinear material and nonlinear geometry model of the superstructure, a 2-D soil domain, and 1-D springs (p-y, t-z, and q-z) at the interface between the bridge-foundation sub-system and the soil domain. A nonlinear staged construction algorithm is used for application of setting the initial stress and strain conditions in the soil domain and for application of the gravity loads in the superstructure. The soil-foundation-bridge system is then subjected to 14 earthquake motions (7 shallow, crustal and 7 subduction zone earthquake motions). The engineering output response quantities that were chosen to characterize the seismic response of the soil-foundation-bridge system are: (1) nodal displacements and absolute accelerations, (2) bending moment, shear force, and axial force in the column and pile, (3) soil stress and strain profiles, (4) mid-span and abutment gap

horizontal deck displacements, and (5) inelastic deformations (cross-section curvature, and concrete and steel fiber strains) of the column and pile. For each earthquake motion, a derived engineering response parameter was defined. The derived response parameter is the number of inelastic excursions of the cross-section curvature over a reference yield curvature as defined in Pri. Various engineering response parameters were plotted against peak ground acceleration (PGA), cumulative absolute velocity (CAV), arias intensity (I_A), pseudo-spectral acceleration at the fundamental period of the system [$S_a(T_1)$], and significant duration (D_{5-95}) to track the importance of each earthquake motion intensity measure in predicting structural damage.

3.2 Earthquake Motion Selection

The Pacific Northwest (PNW) is prone to large subduction zone earthquakes as well as shallow, crustal earthquakes. Each type of earthquake places unique demands on a soil-foundation-bridge system. Traditionally, bridges have been designed to withstand shallow, crustal earthquakes, because these are predominant in California. However, the subduction zone earthquakes have a longer duration, sometimes have a larger amplitude (depending on source-to-site distance), and often have a lower frequency content (longer period) when compared to shallow, crustal earthquakes. Design codes do not differentiate the expected behavior of structures when subjected to these different earthquake motion types; therefore, it is important to examine and compare how bridges withstand both types of earthquake motions.

Earthquake motion selection is an important process as engineers and researchers seek to establish the effects of a predicted seismic loading for a specific site. During the selection process, the median of several (i.e. usually seven or more) earthquake motions is compared to a site-specific design response spectrum. This selection of multiple earthquake motions is termed as a suite or ensemble of earthquake motions.

A site in Portland, Oregon (45.5200353° N, 122.6743645° W) was chosen for the earthquake motion selection. A target design spectrum was generated using the ASCE7-10 standard for soil type C (i.e. very dense soil and soft rock). Soil type C (360 $<V_s$ (m/s) $<$760) was chosen based on the combined soil-bedrock shear wave velocity of the site to a depth of 30 m (ASCE 7-10, 2010). The linear, 5% damped pseudo-spectral acceleration response spectrum is shown in Figure 3.1.

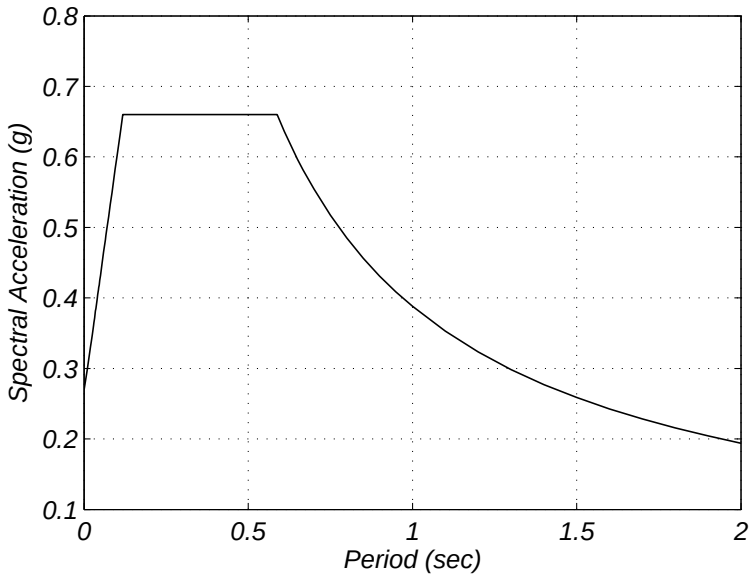

Figure 3.1 ASCE7-10 Design Response Spectrum for downtown Portland, Oregon (45.5200353° N, 122.6743645° W) for soil type C (i.e. very dense soil and soft rock).

The shallow, crustal earthquake motions and the subduction zone earthquake motions were both linearly scaled in the time domain to match the target design response spectrum shown in Figure 3.1. Accordingly, the amplitudes of the earthquake motions from the two different tectonic environments are roughly equivalent, and the frequency contents are also similar, as shown in Figures 3.2 and 3.3. The primary difference between the two types of earthquake motions is the duration, as shown in Table 3.1. This earthquake motion selection strategy allows for the examination of long-duration earthquake motion effects

on soil-foundation-bridge systems.

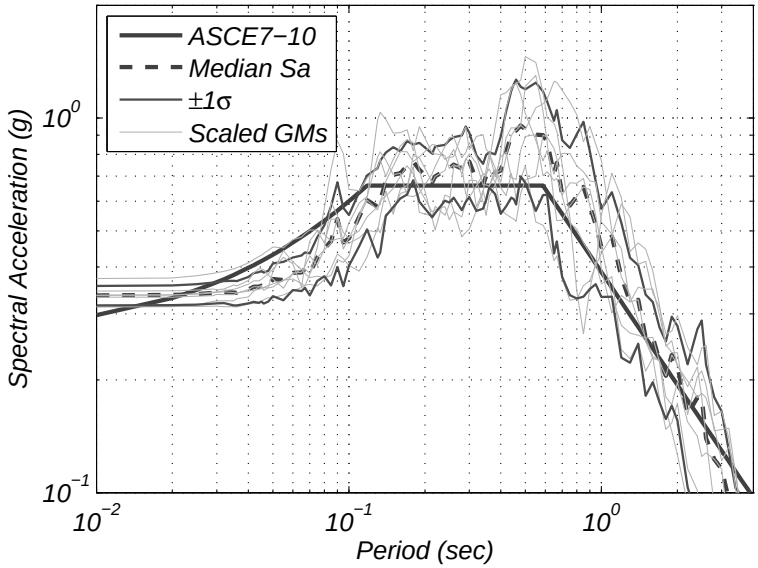

Figure 3.2 Response spectra of selected subduction zone ground motion suite plotted against ASCE7-10 design spectrum for soil type C (i.e. very dense soil and soft rock) in log-log

The suite of seven subduction zone earthquake motions were selected from the Tohoku, Japan (KNET, 2012) and Santiago, Chile (Boroschek et al., 2012) events. The shallow, crustal earthquake motions were selected from the Next-Generation Attenuation of Ground Motions (NGA) earthquake motion database (Power et al., 2008) based on the following parameters, which are representative of magnitudes and distances of shallow, crustal earthquakes that could occur in Portland, Oregon:

- Moment Magnitude = 6.5
- Source-to-Site Distance = 20 to 40 km

Within the NGA earthquake motion database, two orthogonal horizontal acceleration components and one vertical acceleration component were provided for each of the recorded

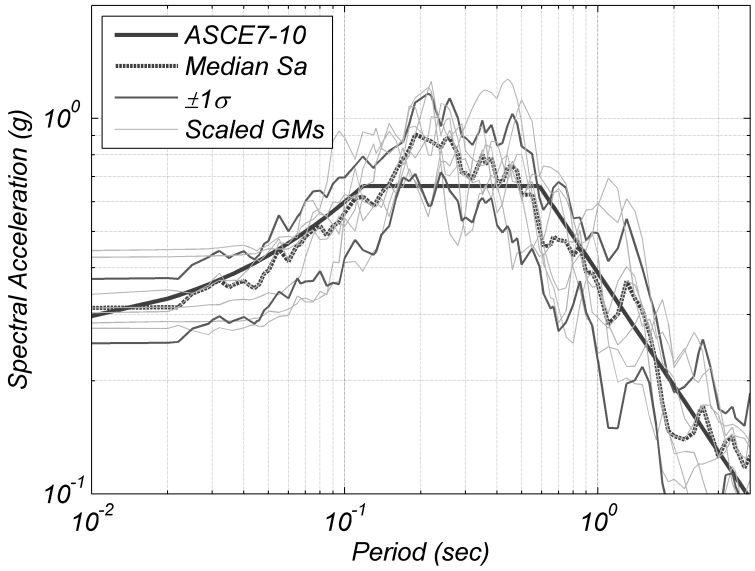

Figure 3.3 Response spectra of selected crustal ground motion suite plotted against ASCE7-10 design spectrum for soil type C (i.e. very dense soil and soft rock) in log-log scale

earthquake motions. In this study, only one of the horizontal components from each selected earthquake motion was considered. The horizontal component that matched the target design spectrum best was selected; therefore, for this study, no preference was given to fault-normal versus fault-parallel earthquake motions. Table 3.1 provides a summary of the fourteen earthquake motions used to analyze the SSI response of the system and their intensity measures.

To automate and simplify the earthquake motion selection process, a MATLAB script was created to calculate the goodness-of-fit and linear scaling factor . Earthquake motion selection was performed by first plotting the original, unscaled response spectrum for each earthquake motion and comparing the spectral accelerations to the design spectral accelerations. Each earthquake motion was then scaled linearly by a scaling factor, SF, within the range of 0.2 $<$SF$<$ 5.0. Weighting, or specifying a range of spectral periods for the

Table 3.1 Summary table of the fourteen scaled crustal and subduction zone earthquake motions. For each earthquake motion the date of occurrence, station, moment magnitude, peak ground acceleration, peak ground velocity, spectral acceleration at the first fundamental period of the system, significant duration, arias intensity, and cumulative absolute velocity are listed.

Type	Earthquake	Year	Station	M_w	PGA (g)	PGV (cm/s)	$D_{5\text{-}95}$ (sec)	I_A (m/s)	S_a @ T_1=0.89s (g)	CAV (m/s)
CRUSTAL	Loma Prieta, CA	1989	Fremont	6.93	0.43	28.47	17.24	1.67	0.56	12.49
	Loma Prieta, CA	1989	Salinas	6.93	0.33	38.65	21.46	1.86	0.42	13.51
	Loma Prieta, CA	1989	Saratoga	6.93	0.40	32.31	9.36	1.19	0.43	8.48
	Loma Prieta, CA	1989	Hollister	6.93	0.29	47.24	28.75	2.00	0.79	16.91
	Landers, CA	1992	Yermo Fire Sta.	7.28	0.27	53.53	18.86	2.26	0.79	15.97
	San Fernando, CA	1971	LA Hollywood	6.61	0.32	26.89	11.17	1.37	0.63	9.04
	Loma Prieta, CA	1989	Gilroy	6.93	0.42	38.76	13.84	1.24	0.50	9.50
SUBDUCTION ZONE	Tohoku, Japan	2011	IWTH1611	9.0	0.35	41.37	95.08	6.08	0.65	60.77
	Tohoku, Japan	2011	FKSH0311	9.0	0.31	27.62	96.33	5.04	0.75	52.64
	Tohoku, Japan	2011	IWTH1111	9.0	0.33	28.29	102.36	6.97	1.04	64.96
	Tohoku, Japan	2011	MYGH0911	9.0	0.31	31.61	104.68	4.91	0.96	50.49
	Tohoku, Japan	2011	AOMH1211	9.0	0.34	32.28	106.04	6.88	0.51	65.95
	Maule, Chile	2010	Maipu	8.8	0.37	29.85	33.77	2.88	0.43	24.91
	Maule, Chile	2010	Viña del Mar	8.8	0.34	32.33	30.62	4.50	1.19	35.86

M_w - moment magnitude
PGA - peak ground acceleration
PGV - peak ground velocity
$D_{5\text{-}95}$ - significant dutation
I_A - arias intensity
S_a - spectral acceleration at the first fundamental period
CAV - cumulative absolute velocity

scaled response spectrum to match the design spectrum (e.g. envelope the first fundamental period, T_1, of the structure), was not used. A root-mean-square-error (RMSE), which measures the goodness-of-fit for the response spectrum to the target spectrum, was calculated for each scale factor (SF), as follows:

$$RMSE = \sqrt{(\log S_{a,Target} - \log (SF \times S_{a,Eqke}))^2} \tag{3.1}$$

where $S_{a,Target}$ is the spectral accelerations for the target spectrum, SF is the scaling factor, and $S_{a,Eqke}$ is the spectral accelerations for the individual original, unscaled earthquake motions.

The minimum RMSE and corresponding SF were recorded for each motion. The seven motions for each type of earthquake with the smallest RMSE values and their corresponding SF were recorded in an output file. The output file was then reviewed to ensure that both components of the same station were not saved. If two components of the same station were saved in the output file, then the component with the largest RMSE value was removed from further consideration. The earthquake motion selection procedure was repeated until the seven selected motions were all from different stations. The semi-automated earthquake motion selection process described in this paragraph is similar to the process devised by Kottke and Rathje (2008). Table 3.2 shows the final selected earthquake motions and the corresponding values of RMSE, scale factor, and component. Figures 3.4 through 3.5 are summary plots of the design spectra and earthquake motion response spectra. Figure 3.6 shows a comparison of the shallow, crustal median response spectrum and the subduction zone median response spectrum.

The mean, μ_Y, and standard deviation, σ_Y, of the combined suite response spectrum is computed by:

$$\mu_Y = \exp(\mu_{lnY} + 0.5{\sigma_{lnY}}^2) \tag{3.2}$$

Table 3.2 Summary of selected suite of earthquake motions and associated RMSE

Type	Earthquake	Year	Station	Component	M_w	R_{rup}/R_{epi} (km)	RMSE (%)
CRUSTAL	Loma Prieta, CA	1989	Fremont	090	6.93	55.2	2.117
	Loma Prieta, CA	1989	Salinas	250	6.93	46.4	2.316
	Loma Prieta, CA	1989	Saratoga	090	6.93	27.2	2.480
	Loma Prieta, CA	1989	Hollister	090	6.93	48.2	2.828
	Landers, CA	1992	Yermo Fire Sta.	360	7.28	86.0	2.831
	San Fernando, CA	1971	LA Hollywood	090	6.61	39.5	2.847
	Loma Prieta, CA	1989	Gilroy	000	6.93	32.4	3.126
SUBDUCTION ZONE	Tohoku, Japan	2011	IWTH1611	E-W	9.0	238	2.181
	Tohoku, Japan	2011	FKSH0311	N-S	9.0	279	2.226
	Tohoku, Japan	2011	IWTH1111	N-S	9.0	260	2.353
	Tohoku, Japan	2011	MYGH0911	N-S	9.0	198	2.428
	Tohoku, Japan	2011	AOMH1211	N-S	9.0	312	2.751
	Maule, Chile	2010	Maipu	E-W	8.8	198	3.424
	Maule, Chile	2010	Viña del Mar	N-S	8.8	205	3.968

M_w - Moment Magnitude
R_{rup}/R_{epi} - Rupture Distance/Epicentral Distance
RMSE - Root Mean Square Error
SF - Scale Factor

and

$$\sigma_Y = \sqrt{\mu_Y{}^2 \exp\left(\sigma_{ln}\right)^2 - 1} \tag{3.3}$$

where μ_Y is the median suite response spectra and σ_Y is the standard deviation ($\pm 1\sigma$) for the median suite response spectra.

3.3 Soil-Foundation-Bridge Model Development

The soil-foundation-bridge (SFB) system was modeled using a 2-D finite element (FE) model developed in the OpenSees framework (McKenna et al., 2000). The two-dimensional FE model of the soil-bridge system includes different components for the foundation and for the superstructure, as shown in Figure 3.7. The work by Khosravifar (2012), Chiaramonte (2011), Shamsabadi et al. (2007), Brandenberg et al. (2005) and Boulanger et al.

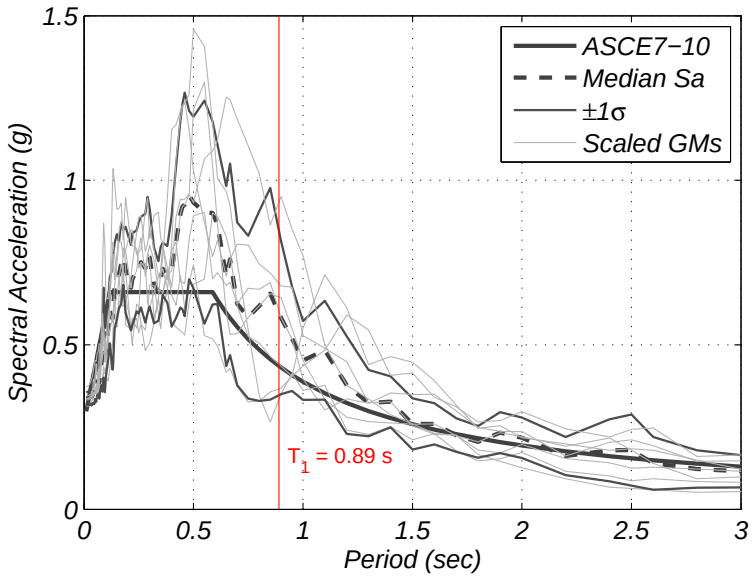

Figure 3.4 Response spectra of selected subduction zone ground motion suite plotted against ASCE7-10 design spectrum for soil type C (Very Dense Soil and Soft Rock) in linear scale. T_1 is the first fundamental period of the system.

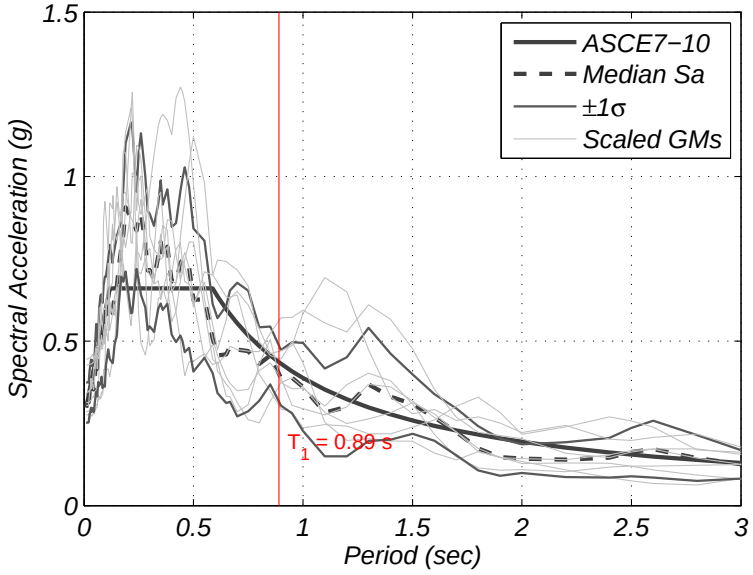

Figure 3.5 Response spectra of selected crustal ground motion suite plotted against ASCE7-10 design spectrum for soil type C (Very Dense Soil and Soft Rock) in linear scale. T_1 is the first fundamental period of the system.

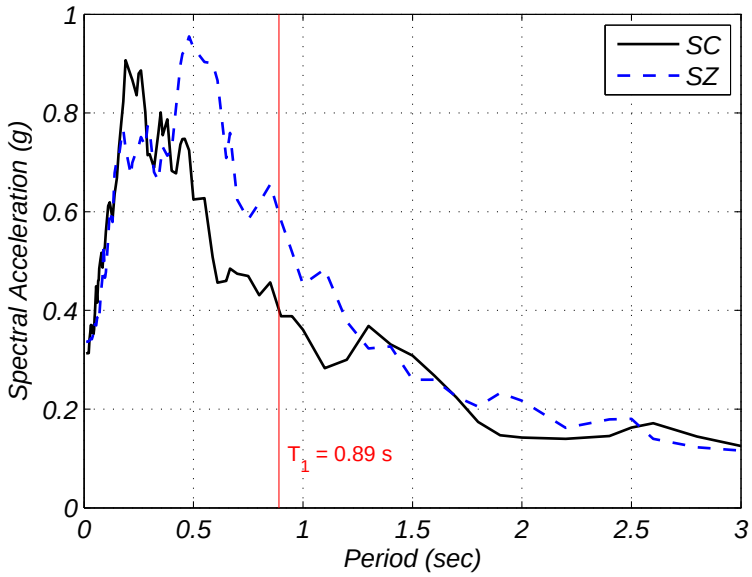

Figure 3.6 Comparison of the median response spectra for the crustal and subduction zone earthquake motion suites.

(1999) was instrumental for creating the models described in this study.

The main components of the soil-foundation-bridge model are shown in Figure 3.7. Important foundation components include, nonlinear structural elements (fiber-section force-based distributed plasticity nonlinear beam-column elements) to model the bridge pile foundation, a far-field nonlinear soil column, and nonlinear, horizontal (p-y), vertical (t-z), and end bearing (q-z) soil-interface springs connecting the pile structural elements to the far-field soil column to model the near-field interaction between the foundation and the soil pile. The soil column (20 m $\times$ 20 m $\times$ 10 m) is fixed at the base, which represents bedrock. The nodes of the soil mesh are constrained to have the same displacements using a nodal algorithm (Cook et al., 2002). The superstructure components include, nonlinear bridge column modeled using distributed plasticity fiber-section force-based nonlinear beam-column elements, linear elastic bridge deck (63.4 m $\times$ 10.36 m $\times$ 1.67 m), bridge abutments modeled using zero-length nonlinear spring gap elements that represent

Table 3.3 Summary of the various OpenSees constitutive models used to model the various components within the soil-foundation-bridge system

Component	OpenSees Model	Reference
Pile & Column	Steel02	Filippou et al., 1983
Pile & Column	Concrete02	Yassin, 1994
Gap	ElasticPPGap	Bozorgzadeh, 2007
Py Spring	PySimple1	Boulanger et al., 1999
Tz Spring	TzSimple1	Boulanger et al., 1999
Qz Spring	QzSimple1	Boulanger et al., 1999
Soil Mesh	PDMY	Elgamal et al., 2002

PDMY - Pressure-Dependent-Multi-Yield

the backfill response. The nonlinear column, having the same cross-sectional properties as the pile, extends 6.1 m from the top of the pile (ground surface) to the base of the linear elastic bridge deck (i.e. the pile is 20 m in length). The elastic deck is restrained against vertical displacements. Table 3.3 summarizes the various constitutive models.

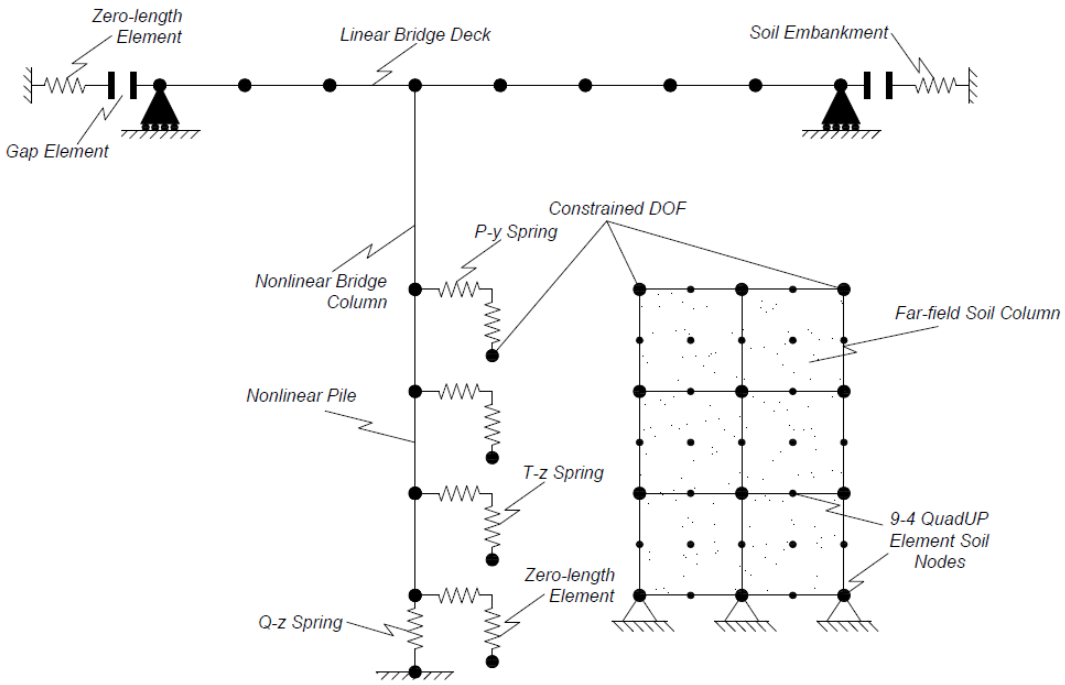

Figure 3.7 Soil-foundation-bridge (SFB) system used for all analyses

3.3.1 Soil Column

Validation of the seismic response of the soil mesh modeled in OpenSees was completed by comparing the surface acceleration-time series predicted using OpenSees with the surface acceleration-time series predicted using DEEPSOIL (Park and Hashash, 2004). The Northridge, California (Alhambra - Fremont School, 090) acceleration-time series was used as the validation input motion.

Figure 3.8 illustrates the surface spectral accelerations for the OpenSees and DEEPSOIL model. The amplitude, frequency content, and duration of the surface acceleration-time series predicted by both models is similar. Figure 3.9 shows the Fourier Amplitude Spectrum for bedrock (input) and ground surface and how the amplitude of the Northridge, California earthquake motion is distributed with respect to frequency content. Notice the peak amplitude for both the bedrock and surface motions occur at the same frequency. Even

so, soil amplification can be seen in the surface FAS at the frequency range 3 to 5 Hz.

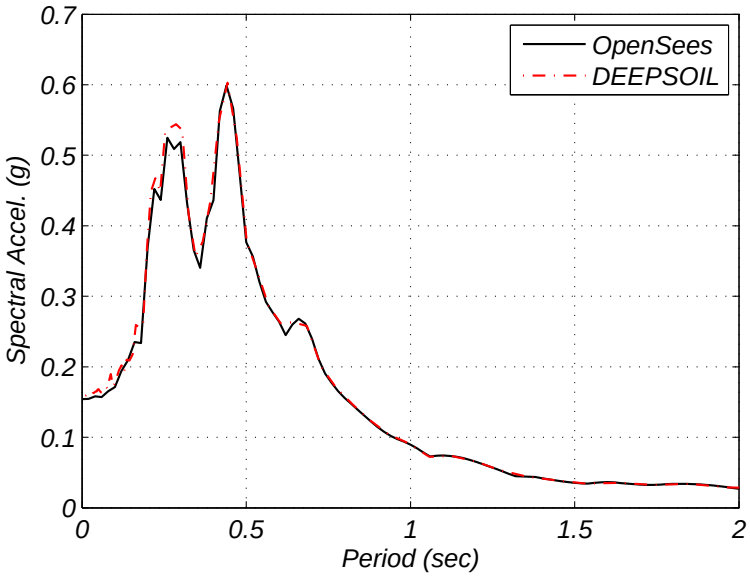

Figure 3.8 Comparison of the surface spectral accelerations for the OpenSees and DEEPSOIL model

The soil column, shown in Figure 3.10, is modeled as 2-D, plane strain, uniform soil mesh fixed at the base in the horizontal, vertical, and rotational directions, representing a rigid bedrock layer assumption directly beneath the soil column. The mesh consists of multiple 9-4 quadrilateral u-p elements, shown in Figure 3.11, with nine Gauss integration points, that couple the soil skeleton displacement, u, and the pore water pressure, p (Elgamal et al., 2002; Zhang et al., 2003, 2008).

In the development of a shear only soil-column, which is a typical assumption for modeling the propagation of the seismic waves across a soil profile, nodes of the soil mesh are constrained to have the same displacements. In OpenSees, this is achieved by setting a multi-point constraint between nodes at the same depth from the surface (this construct is termed equalDOF in OpenSees). This multi-point constraint dictates that the constrained nodes have the same horizontal and vertical displacements at either ends of the soil column.

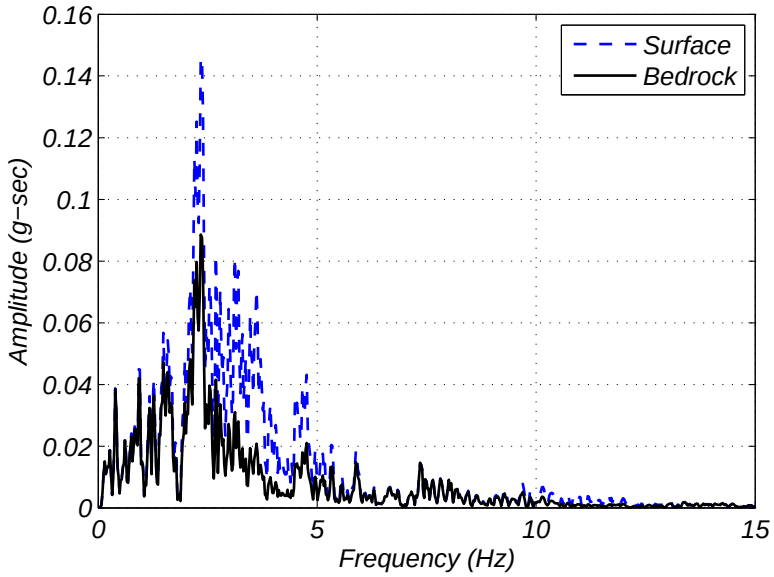

Figure 3.9 Fourier Amplitude Spectra of the bedrock and surface ground motions. Soil amplification at the surface can be seen from about 3 to 5 Hz.

Figure 3.12 (Chiaramonte, 2011) illustrates how the displacement constraints influence the response of the soil column when ground accelerations are applied to the base. The layered shear column behavior labeled "Correct Deformation" in Figure 3.12 illustrates the desired deformation response mode.

The soil column, which was specified as dense, homogeneous, non-liquefiable sand, was used for the soil mesh. A surcharge gravity load of one atmosphere (1 bar or 101 kPa) was applied to the soil column to simulate pre-bridge construction in-situ conditions. Table 3.4 provides a summary of the soil material input parameters specified during analysis.

The Pressure-Dependent-Multi-Yield (PDMY) material model (Elgamal et al., 2002) was used to define the constitutive behavior of cohesionless soils. This 2-D constitutive relation incorporates a number of cone shape surfaces that describe the yield-criteria. The model has a non-associative flow rule, a purely deviatoric kinematic hardening rule, and volumetric dilation and contraction develop due to shear deformation. The PDMY mate-

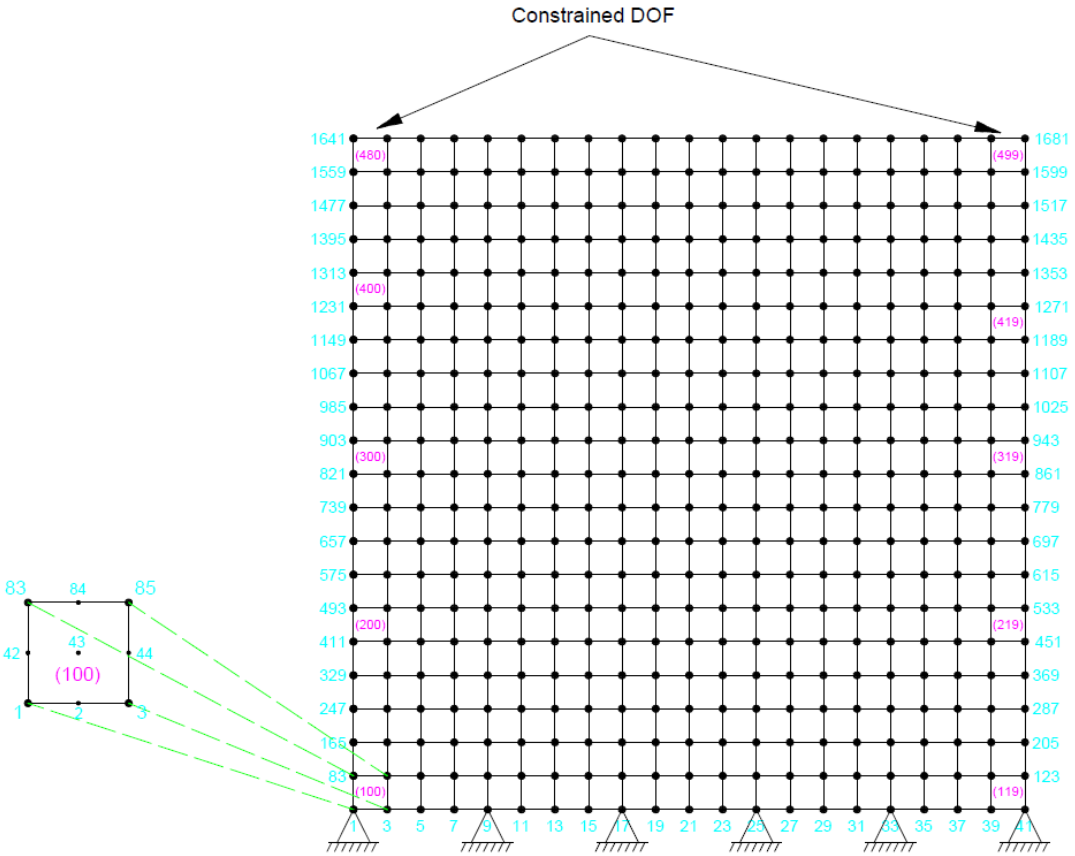

Figure 3.10 Illustration of the 20 m × 20 m 2-D, plane strain, uniform soil mesh modeled using multiple 9-4 quadrilateral u-p elements. Nodes are shown as black circles and labeled with cyan numbers, and elements are shown in pink parentheses.

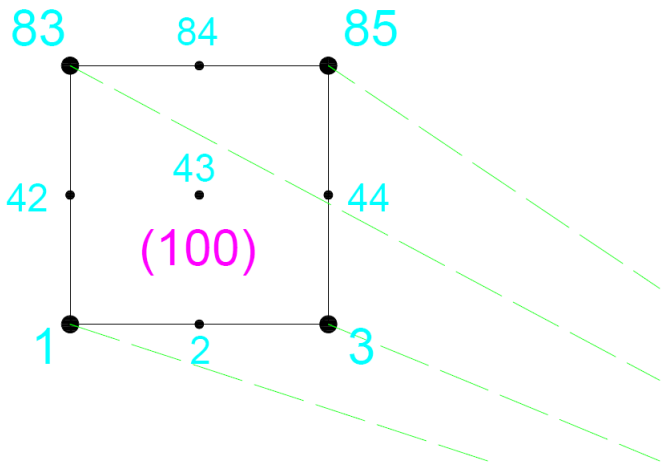

Figure 3.11 Illustration of the 9-4 quadrilateral u-p elements, with nine Gauss integration points, that couple the soil skeleton displacement, *u*, and the pore water pressure, *p*. Nodes and elements are distinguished by the colors cyan and pink, respectively.

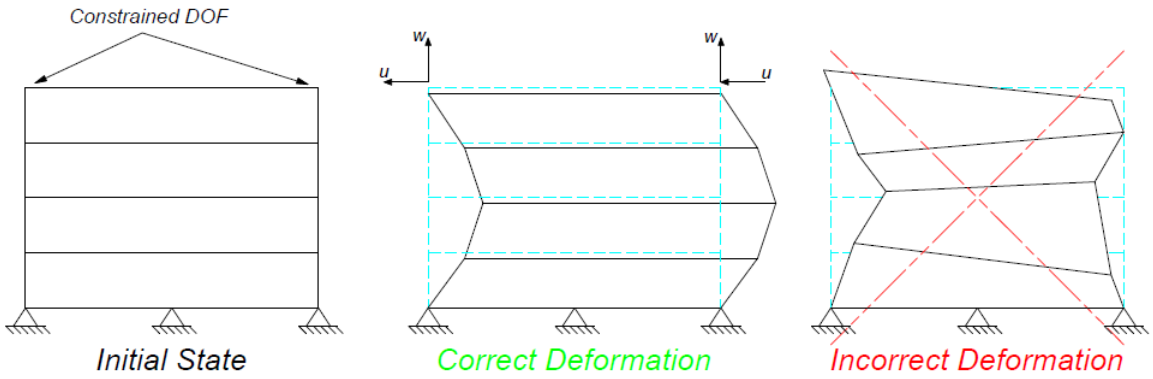

Figure 3.12 Schematic illustrating the OpenSees equalDOF command relating to deformation of the soil column (Chiaramonte, 2011)

Table 3.4 Soil material input parameters for a dense (D_R=90%), saturated, undrained sand modeled after (Yang, 2000)

Model Parameters	Dense Sand	Model Parameters	Dense Sand
Material Type	*PDMY*	*Pressure Dependent Coeff., d*	0.5
Relative Density, D_R	90%	*Friction Angle, φ'*	40.0
Soil Mass Density, ρ_s	2.1 Mg/m^3	*Phase Transformation Angle, φ_{PT}*	27.0
Fluid Mass Density, ρ_w	1.0 Mg/m^3	*Contraction Coeff., c*	0.03
Shear Modulus, G	1.3x10^5 kPa	*Dilation Coeff., d_1*	0.8
Shear Wave Velocity, V_s	250 m/s	*Dilation Coeff., d_2*	5.0
Soil Bulk Modulus, B	3.9x10^5 kPa	*Liquefaction Coeff., L_1*	0.0
Horiz. Permeability, K_h	0.001	*Liquefaction Coeff., L_2*	0.0
Vert. Permeability, K_v	0.001	*Liquefaction Coeff., L_3*	0.0
Peak Shear Strain, γ_p	0.1	*Void Ratio, e*	0.45
Reference Pressure, p'_r	80.0	*Number of Yield Surfaces*	20

rial model is fully implemented in OpenSees. Relative density, D_R, describes the tightness of compaction relative to the maximum density. The unit mass of the soil and water per cubic meter is defined by the soil mass density, ρ_s, and fluid mass density, ρ_w, respectively. The shear modulus, G, describes the soil stiffness and is computed by dividing the shear stress by the shear strain. As stresses vary during loading, the soil bulk modulus, B, relates the change in stress to the volumetric strain. Horizontal and vertical permeability, K_h and K_v, respectively, describe the seepage through the soil material in the horizontal and vertical directions, respectively. Peak shear strain, γ_p, is the shear strain at which the peak shear stress occurs. Reference pressure, p'_r, is the mean effective confining pressure at which shear modulus, soil bulk modulus, and peak shear strain are defined. The pressure dependent coefficient, d, defines variations of the shear modulus and soil bulk modulus during loading as a function of instantaneous effective confinement. The friction angle, ϕ, represents the peak shear strength of the soil. The line that describes the transition from compressive to dilative behavior is referred to as the phase transformation angel, ϕ_{PT}. The contraction and dilation coefficients define the compressive and dilative behavior, respec-

tively and similarly, the liquefaction coefficients define the liquefaction behavior of the sand. Due to the dense configuration of the sand, the liquefaction coefficients were set to be zero to neglect the effects of liquefaction. Void ratio, e, is defined as the volume of the voids over the volume of the solids and is a measure of soil density. The number of yield surfaces, NYS, is the yield-criteria for sands described by the number of cone shape surfaces. For further details on the soil parameters used to describe the soil material model, the reader is referred to the paper by Elgamal et al. (2002).

The total height and width of the soil column are 20 meters. The soil mesh models the soil overlying a rigid bedrock layer. The rigid bedrock layer has a shear wave velocity of (at least) 760 m/s. The out-of-plane thickness is important in determining the mass of the soil column but does not affect the soil elements attached to the soil-interface springs, which are assumed to maintain a state of plane strain throughout the analysis. Other researchers [e.g., Zhang et al. (2008), Bowers (2007), and Aygün et al. (2010)] used an out-of-plane thickness equal to the width of the bridge. A sensitivity analysis was performed by analyzing the model with a 10 m and 100 m thick soil column to test the effects of out-of-plane soil column thickness on the system. It was found that for soil column thicknesses of 100 m and 10 m the axial force and bending moment in the column changed 0.9% and 5.9%, respectively. Therefore, the final out-of-plane thickness of the soil mesh was chosen to be 10 m.

The individual height of the soil elements was selected based on the relationship presented by Seed (1987), and expressed as:

$$h_{max} = \frac{V_s}{8 f_{max}} \tag{3.4}$$

where h_{max} is the maximum height, in meters, of the soil layer, f_{max} equals 15 Hz, and V_S is the shear wave velocity, in m/s, of the softest layer. Using equation 3.4, the height of the

soil elements was calculated to be 1.8 m. The adopted maximum soil element height was defined to be 1 m, thus allowing for capturing, reliably, frequencies below 25 Hz.

3.3.2 Soil-Interface Springs

The soil-interface springs connect the structural elements to the far-field soil column to model the interaction between the pile foundations and the surrounding soil. Three types of soil-interface springs are used to model the soil-pile interface: lateral resistance (p-y), skin friction (t-z), and end bearing resistance (q-z). The parameters defining the soil springs were chosen in accordance with recommendations from API (1993). Additionally, the p-y and t-z element stiffness, were modified at larger depths, according to Boulanger et al. (1999). Thus, the API (1993) stiffness was modified by a factor of $\sqrt{50kPa/\sigma_v}$ to incorporate the overburden effective stress, where the vertical effective overburden stress is the unit weight of soil multiplied by the depth below the ground surface. The horizontal (p-y), vertical (t-z), and end bearing (q-z) soil spring material models by Boulanger et al. (1999) were implemented in OpenSees and are referred to as PySimple1, TzSimple1, and QzSimple1.

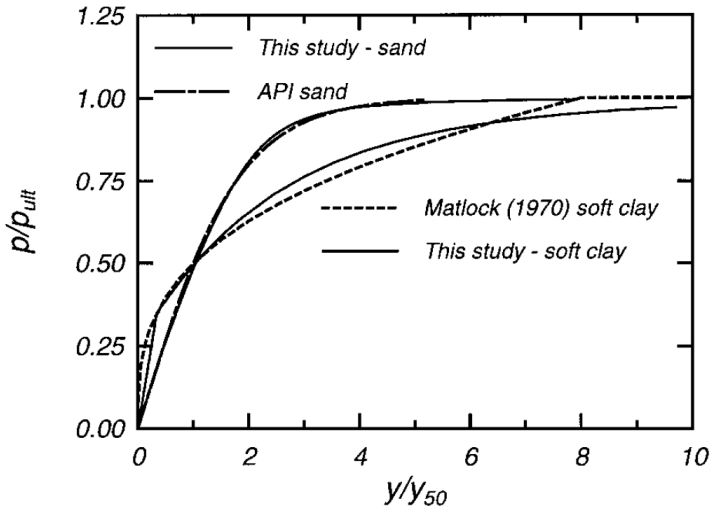

Figure 3.13 Load-displacement curve as defined by Boulanger et al. (1999)

Each spring is defined by an ultimate resistance (p_{ult}, t_{ult}, and q_{ult}) and the displacement at which 50% of the ultimate resistance is mobilized (i.e. y_{50} for p-y and z_{50} for the t-z springs) (Boulanger et al., 1999). The spring parameters vary with depth, and Tables 3.5 and 3.6 summarize how the p-y and t-z spring elements parameters vary with depth. A more in depth discussion of the meaning and contribution of each parameter is provided by Reese et al. (1974) (p-y) and Mosher (1984) (t-z) . Gapping effects are modeled after Boulanger et al. (1999), and the gapping effects incorporate residual resistance or drag force along the sides of the pile. Gapping is described by the formation of an opening between the pile and soil due to residual deformation in the soil. The drag coefficient, C_d, is defined as the ratio of the residual resistance to the ultimate resistance, p_{ult}. A value of 0.3 was used as the drag coefficient to define the drag resistance within a fully mobilized gap . The drag resistance, R_d, is calculated by multiplying the coefficient of drag by the ultimate capacity of the p-y spring (API, 1993).

Validation of the soil-interface springs was completed by extending laterally and vertically the p-y and t-z springs, respectively, and by compressing vertically the q-z spring and verifying the response of the force displacement curves. Results from the push-pull tests are shown below in Figures 3.14 through 3.16. The p-y and t-z springs were extended and the q-z spring was compressed by some load greater than their respective ultimate resistance values to obtain the curves. Each of Figures 3.14 through 3.16 level off at the various ultimate resistance values and y_{50} is verified by picking the displacement at 50% of the ultimate resistance. Figure 3.16 exhibits a “kink” in the initial slope of the curve illustrating the transition from elastic to inelastic behavior.

Table 3.5 Summary table of the calculated p-y soil-interface spring values varying with depth (Reese et al., 1974)

Depth (m)	Element	L_t (m)	σ'_v (kPa)	A_{bar}	c_σ	$p_{u,1}$ (kN)	$p_{u,2}$ (kN)	p_{ult} (kN)	y_{50} (m)
0.5	1041	0.5	5.40	2.52	3.044	99	1585	49	0.0003
1.0	1039	1.0	10.8	2.13	2.153	223	2678	223	0.0011
2.0	1037	1.0	21.6	1.53	1.522	481	3851	481	0.0016
3.0	1035	1.0	32.4	1.15	1.243	725	4347	725	0.0020
4.0	1033	1.0	43.2	0.95	1.076	1000	4795	1000	0.0024
5.0	1031	1.0	54.0	0.88	0.963	1388	5543	1388	0.0030
6.0	1029	1.0	64.7	0.88	0.879	1944	6651	1944	0.0038
7.0	1027	1.0	75.5	0.88	0.814	2592	7760	2592	0.0047
8.0	1025	1.0	86.3	0.88	0.761	3334	8869	3334	0.0057
9.0	1023	1.0	97.1	0.88	0.718	4167	9977	4167	0.0067
10.0	1021	1.0	107.9	0.88	0.681	5094	11086	5094	0.0078
11.0	1019	1.0	118.7	0.88	0.649	6114	12195	6114	0.0089
12.0	1017	1.0	129.5	0.88	0.621	7226	13304	7226	0.0101
13.0	1015	1.0	140.3	0.88	0.597	8431	14412	8431	0.0113
14.0	1013	1.0	151.1	0.88	0.575	9728	15521	9728	0.0125
15.0	1011	1.0	161.9	0.88	0.556	11119	16630	11119	0.0138
16.0	1009	1.0	172.7	0.88	0.538	12602	17738	12602	0.0152
17.0	1007	1.0	183.4	0.88	0.522	14178	18847	14178	0.0166
18.0	1005	1.0	194.2	0.88	0.507	15846	19956	15846	0.0180
19.0	1003	1.0	205.0	0.88	0.494	17607	21065	17607	0.0195
20.0	1001	0.5	215.8	0.88	0.481	19461	22173	9731	0.0105

L_t - tributary length for each spring

σ'_v - vertical effective stress

$\bar{A}$ - empirical adjustment factor

c_σ - empirical adjustment factor (Boulanger et al., 1999)

$p_{u,1,2}$ - ult. resistance accounting for depth effects (Reese et al., 1974)

y_{50} - horiz. displacement at which 50% of the resistance is mobilized

Table 3.6 Summary table of the calculated t-z soil-interface spring values varying with depth (Mosher, 1984)

Depth (m)	Element	L_t (m)	σ'_v (kPa)	t_{ult} (kN)	z_{50} (m)
0.5	2041	0.5	5.40	2.3	0.0007
1.0	2039	1.0	10.8	9.0	0.0007
2.0	2037	1.0	21.6	18	0.0007
3.0	2035	1.0	32.4	27	0.0007
4.0	2033	1.0	43.2	36	0.0007
5.0	2031	1.0	54.0	45	0.0007
6.0	2029	1.0	64.7	54	0.0007
7.0	2027	1.0	75.5	63	0.0007
8.0	2025	1.0	86.3	72	0.0007
9.0	2023	1.0	97.1	81	0.0007
10.0	2021	1.0	107.9	90	0.0007
11.0	2019	1.0	118.7	99	0.0007
12.0	2017	1.0	129.5	108	0.0007
13.0	2015	1.0	140.3	117	0.0007
14.0	2013	1.0	151.1	126	0.0007
15.0	2011	1.0	161.9	135	0.0007
16.0	2009	1.0	172.7	144	0.0007
17.0	2007	1.0	183.4	153	0.0007
18.0	2005	1.0	194.2	162	0.0007
19.0	2003	1.0	205.0	171	0.0007
20.0	2001	0.5	215.8	90	0.0007

z_{50} - vert. displ. at which 50% of the resistance is mobilized

t_{ult} - ult. vert. resistance (Mosher, 1974)

σ'_v - vert. eff. stress

L_t - tributary length

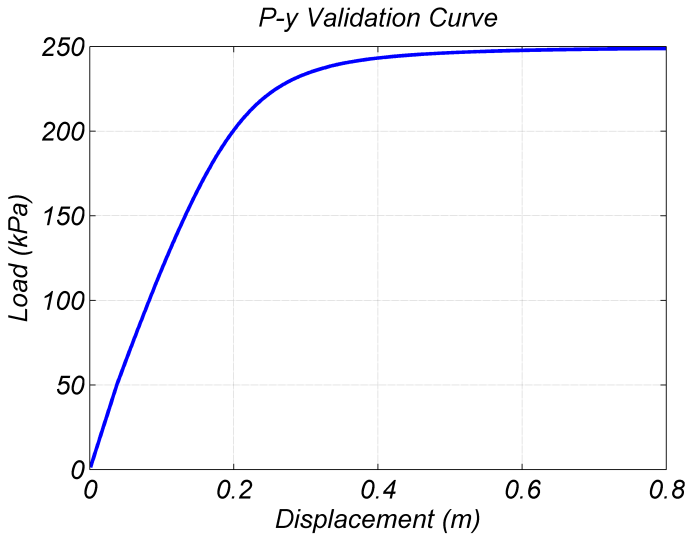

Figure 3.14 Validation curve for p-y soil-interface spring. For validation, p_{ult}=250 kPa and y_{50}=0.1 m, respectively

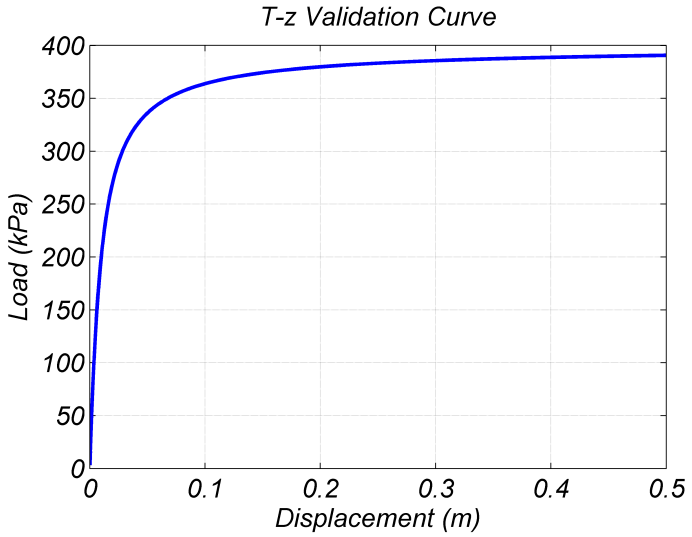

Figure 3.15 Validation curve for t-z soil-interface spring. For validation, t_{ult}=400 kPa and z_{50}=0.01 m, respectively

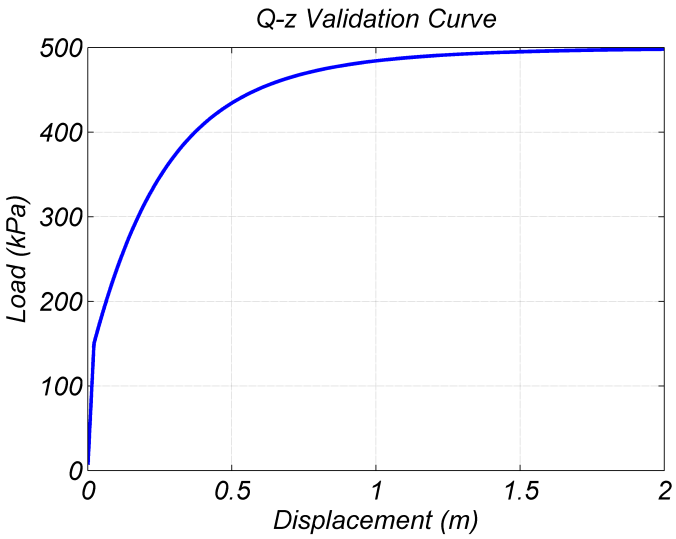

Figure 3.16 Validation curve for q-z soil-interface spring. For validation, q_{ult}=500 kPa and z_{50}=0.1 m, respectively

3.3.3 Pile Foundation and Bridge Column

Figure 3.17 shows the 6.1 meter-tall, 1.10 meter-diameter single pile bridge foundation cross-section. The pile is a reinforced concrete pile, and it is modeled using the flexibility-based nonlinear beam-column element (Neuenhofer and Filippou, 1998), which allows for the formation of a plastic hinge anywhere along the pile. Hinging is allowed because of the distributed plasticity formulation within these elements. The compressive strength, f'_c, was specified based on the Yassin (1994) concrete model (designated as Concrete02 in OpenSees), which is based on the Kent-Scott-Park (Kent and Park, 1971; Scott et al., 1982) model for the compression and includes a linear tension softening for the concrete. Two uniaxial materials models were used to define the unconfined and confined concrete stress-strain behavior. Confined concrete behavior was defined based on Karthik and Mander (2010). The fibers of the reinforcing steel were modeled using the Menegotto and Pinto (1973) model, as modified by Filippou et al. (1983), which is designated in OpenSees as Steel02.

The pile cross-section consists of a confined concrete core, an unconfined concrete cover with a specified concrete strength of 28 MPa, and 16 #10 ASTM A706 Grade 60 (475 MPa) reinforcing steel bars placed at the confined and unconfined concrete interface.

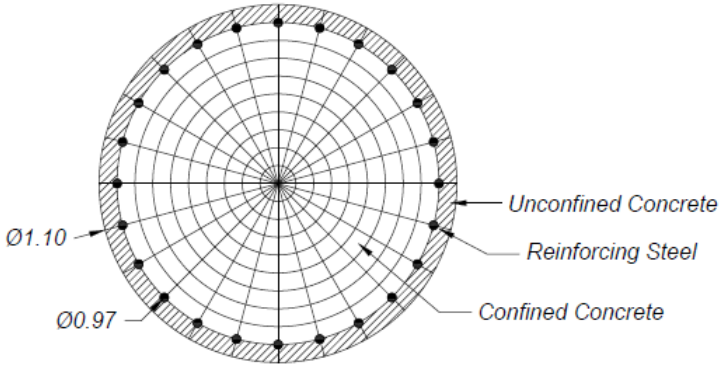

Figure 3.17 Bridge column/pile cross section discretized into a fiber-section with unconfined concrete (cover), confined concrete (core), and longitudinal steel bar reinforcement (all dimensions in meters).

To determine the cracked modal parameters of the structure and the fundamental period of the soil-foundation-abutment-bridge system and mode shape, an eigenvalue analysis was performed within OpenSees, and the first fundamental period was found to be 0.89 seconds. Rayleigh damping was used to model the material damping of the soil-foundation-bridge system, given by:

$$\mathbf{c} = a_0\mathbf{m} + a_1\mathbf{k} \tag{3.5}$$

where **c** is the Rayleigh damping matrix, **m** is the mass matrix, and **k** is the stiffness matrix. Mass-proportional (a_0) and stiffness-proportional (a_1) damping coefficients define the mass proportional and stiffness proportional constituents of the Rayleigh damping matrix, expressed as:

$$a_0 = \zeta \frac{2\omega_i\omega_j}{\omega_i + \omega_j} \tag{3.6}$$

and

$$a_1 = \zeta \frac{2}{\omega_i + \omega_j} \tag{3.7}$$

where ω_i is the natural circular frequency of the lower selected mode, ω_j is the natural circular frequency of the higher mode, and ζ is the baseline damping value, set to 2% at frequencies of 7 rad/s and 125 rad/s, as shown in Figure 3.18. The pseudo-spectral acceleration for each earthquake motion was found at the first fundamental period. The natural circular frequency of 7 rad/s corresponds to the first fundamental natural circular frequency of the soil-foundation-bridge system. The natural circular frequency of 125 rad/sec was set to capture the first three modes of the soil-foundation-bridge system.

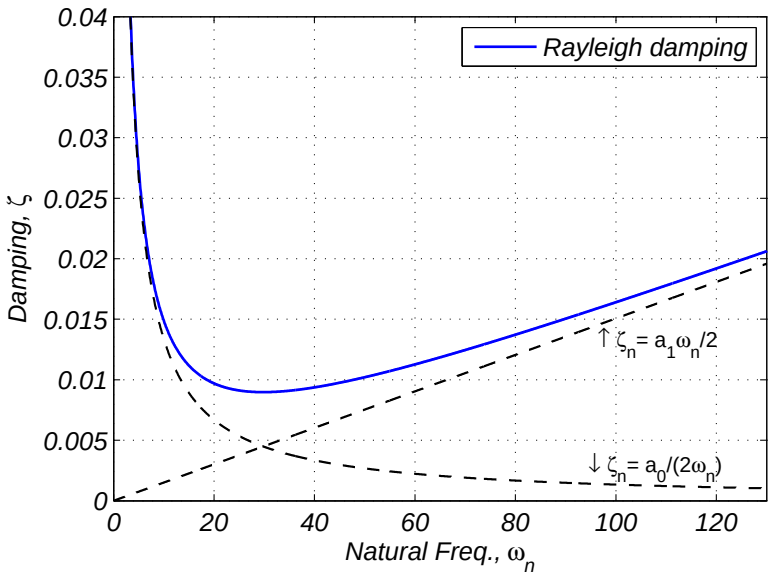

Figure 3.18 Rayleigh damping versus natural circular frequency

A single nonlinear 1.10 m diameter reinforced concrete Type 1 Caltrans shaft (Caltrans, 2006) with uniform reinforcing steel was used for the validation of column-pile moment-curvature. The assumed length for the pile is 20 m (identical to the depth of the soil column) and the column, extending from the top of the soil to the base of the bridge deck, is 6.1 m tall. The reinforced concrete section is discretized using fiber sections with a longitudinal

steel ratio of 1.0% and 6.35 cm of unconfined concrete cover, as shown in Figure 3.17. The nonlinear reinforced concrete section was designed for an axial load of 3483 kN, which corresponds to the expected deck gravity loads being carried by the column at the column-deck interface. The expected unconfined concrete compressive strength of 28 MPa was used and increased by a factor K = 1.38, which is the ratio of confined to unconfined concrete strength (Mander et al., 1988), for the modeling confined concrete. The longitudinal reinforcing bars were specified to have expected yield strength of 475 MPa, elastic modulus of 200 GPa, and a strain hardening ratio of 3%. The material models used for confined and unconfined concrete and reinforcing steel were Concrete02 (Yassin, 1994) and Steel02 (Filippou et al., 1983), respectively.

A sensitivity of the moment-curvature response was performed by considering increasing the number fibers in the cross-section definition. Figure 3.19 shows the moment-curvature responses with a varying number of fibers in which the pile/column section is discretized. The total number of fibers is a function of the number of radial rings considered (8, 12, 16, and 20 rings) and the number of wedges (8, 12, 16, and 20 theta divisions) used for discretizing the section. The number of radial ring and theta wedge divisions were increased proportionally and their definition is illustrated in Figure 3.17. Figure 3.19 shows that the most significant difference in the moment-curvature analysis occurs from 8 to 12 divisions, and the differences in the response for the 16 and 20 divisions is negligible. To maintain computational accuracy and optimize efficiency, the discretization using 16 radial divisions 16 theta wedges was used in subsequent analyses, as illustrated in Figure 3.20.

To further validate the bridge column and pile design the calculated stiffness, k_c, from the load-displacement curve was compared to the calculated stiffness, k_b, of a cantilever column. Both stiffness equations are shown below:

$$k_c = P/u \tag{3.8}$$

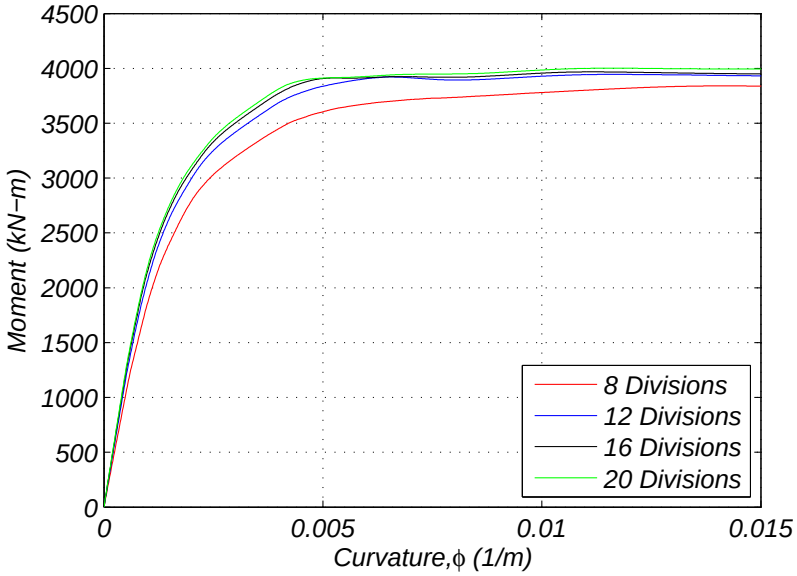

Figure 3.19 The number of radial (rings) and theta (wedges) divisions were varied to determine the most computationally efficient fiber section for the model.

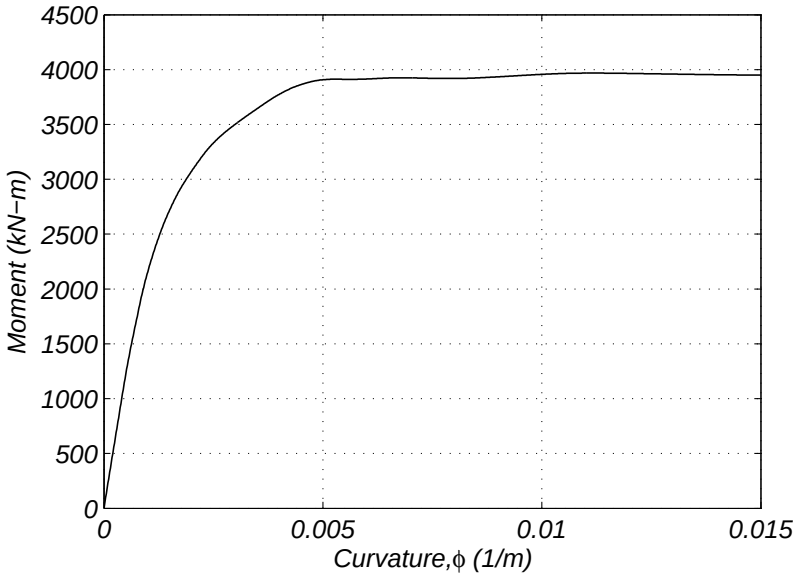

Figure 3.20 The moment-curvature response for the RC section using sixteen radial and theta divisions.

and

$$k_b = 3EI/l^3 \tag{3.9}$$

The calculated stiffness from the load-displacement curve was computed by dividing the horizontal load, P, by the displacement, u. A horizontal load, P, of 800 kN was applied at the top of the column and a displacement, u, of 2.6 m was measured. The calculated stiffness, k_c was found to be 307 kN/m. To compute k_b, the Young's modulus, E = 55 GPa, the moment of inertia, I = 5×10^{10} mm^4, and the length of the cantilever column, l = 30 m. The resulting value of k_b was found to be 306 kN/m. Because the two stiffness values were approximately equal, the bridge column design is further validated.

3.3.4 Bridge Deck

The bridge superstructure, which was modeled after Shamsabadi et al. (2007), consists of two 31.7 meters-long spans, with a total width of 10.36 meters and height of 1.67 meters. Figure 3.21 shows the bridge deck box girder cross-section and dimensions. The box girder is symmetric in the Y-direction, has a cross-sectional area of 4.56 m^2, has a moment of inertia of 5.98×10^{12} mm^4, and the centroid of the section is located 0.93 meters from the bottom face.

No inelastic response is expected from the deck, which is post-tensioned. Therefore, the box girder is modeled using linear elastic beam-column elements, located 0.93 m above the top of the column. Rheological effects of creep and shrinkage are not considered in this model.

The bridge superstructure and column are connected monolithically by a very stiff 0.93 m-long beam-column element. To connect the column to the deck, while maintaining the linear-elastic characteristics of the deck and column-deck connection, a rigid elastic beam-column element was used. This rigid element was modeled by applying a factor of 1000 to the entire stiffness (EI) (i.e. multiplying the Youngs modulus by a factor of 10 and moment

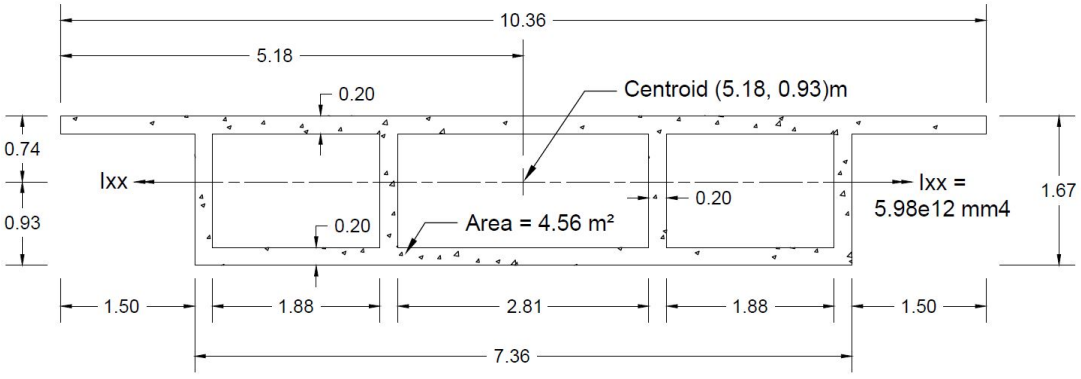

Figure 3.21 Schematic of the box girder cross-section used to model the 63.4 m linear elastic bridge deck

of inertia of the deck by 100). This stiffness factor of 1000 was used to avoid stability issues during analysis and not increase the stiffness factor by too large of a factor.

The bridge abutments are dimensioned in height and width to accommodate and support the bridge deck. Expansion joints are provided at either end of the deck. For longitudinal displacements of the deck, less than the initial opening of the gap, the supports act like rollers. Under large displacements of the deck, the gap provided by the expansion joint closes and the deck pounds on the abutments. Thus, the capacity of the abutment (backwall and backfill) as well as the stiffness of the abutment system have to be defined and are only activated once the initial gap is reduced to zero. By design, the abutment backwall is assumed to shear off and the peak capacity and stiffness is provided mainly by the backfill. The backfill is assumed to be a silty sand as specified by Caltrans (2006). More details pertaining to the strength parameters used to define the backfill response of the silty sand can be found by referring to the paper by Shamsabadi et al. (2007). Under these assumptions the gap element, defined in OpenSees, has the following parameters (Shamsabadi et al., 2007):

- Stiffness, K = 307 kN/cm/m

- Yield Force, F_y = 1397 kN
- Initial Gap Opening = 2.54 cm

The seat-type abutments were modeled in OpenSees with very stiff compressive, elasto-perfectly-plastic gap elements, as illustrated in Figure 3.22. The interaction of the deck, during dynamic loading, compresses and extends the spring elements, thus opening and closing the gap elements. This interaction of the deck with the spring and gap elements simulates the soil-structure interaction response of the backfill soil and deck. It is important to note that the backfill stiffness is inactive until complete closure of the gap.

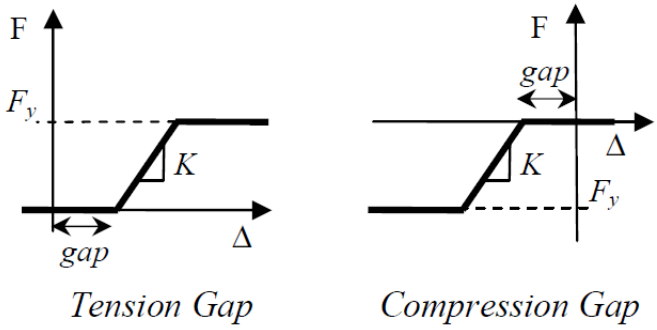

Figure 3.22 Tension and compression elastic-perfectly-plastic gap elements (Barbosa and Silva (2007))

3.4 Analysis Methodology

The nonlinear FE analysis of the soil-foundation-bridge system is divided into four stages to simulate in-situ soil conditions both pre- and post-construction and to incorporate the effects of staged construction of the structural components. The four stages are:

- Stage 1: In this stage, the geometry (nodes and connectivity) of the FE model is defined. This includes the geometry of the soil column, the bridge superstructure, and the foundation. Single and multiple point constraints are also defined in this stage.

- Stage 2: (a) In this stage, the linear elastic deck and nonlinear pile and column element nodes and connectivity are defined. In the definition of the nonlinear beam column element cross-section fiber discretization and are assigned. Nonlinear constitutive relationships are assigned to each fiber (unconfined concrete, confined concrete, and steel). (b) With respect to the soil interface models, in this stage, lateral, vertical, and end bearing nonlinear springs are created and connected to the soil column, but not to the bridge pile.

- Stage 3: In this stage, the soil gravity load is applied first to simulate pre-construction subsurface conditions. A nonlinear transient analysis is performed, in which the Krylov-Newton algorithm (Scott and Fenves, 2009) was used to solve the equilibrium equations. Before application of the structure gravity loads, the pile and soil column were connected by the nonlinear soil-interface springs. The next step included the application of the bridge gravity loading. This approach allows for the bridge dead loads to be transferred to the soil, which simulates the resistance of the soil during construction of the bridge pile foundation, column, and deck. A transient analysis was also required for the application of the gravity loading. In the application of both soil and bridge structure gravity loads, large numerical damping was introduced to simulate static loading. Therefore, during the gravity loading of both the soil and bridge, the analyses are critically damped by specifying the Newmark time integration values of 1.5 and 1.0 for β and γ, respectively. By critically damping the system, the nonlinear transient analysis simulates a quasi-static loading condition.

- Stage 4: In this final stage, the nonlinear dynamic time-history analyses are performed using the Newmark constant average acceleration method and assigning the

Table 3.7 Summary table of gravity, eigen, and dynamic analysis parameters

Type	Gravity Analysis Parameters	Eigen Analysis Parameters	Dynamic Analysis Parameters
numberer	RCM	RCM	RCM
system	ProfileSPD	ProfileSPD	ProfileSPD
test	NormDispIncr 1.e-5 50 0	NormDispIncr 1.e-5 50 0	NormDispIncr 1.e-5 50 0
constraints	Penalty 1.e18, 1.e18	Penalty 1.e18, 1.e19	Penalty 1.e18, 1.e20
rayleigh	a_0, 0.0, a_1, 0.0	a_0, 0.0, a_1, 0.0	a_0, 0.0, a_1, 0.0
γ	1.5	1.5	0.50
β	1.0	1.0	0.25
integrator	Newmark γ, β	Newmark γ, β	Newmark γ, β
algorithm	KrylovNewton	KrylovNewton	KrylovNewton
analysis	Transient	Transient	VariableTransient

iteration time step to of 0.005 sec. P-Δ effects are considered in the analysis. Table 3.7 summarizes the various analysis parameters.

For each of the fourteen completed analyses, numerical convergence was achieved for all cases. Table 3.8 provides a summary of the initial number of time steps and integration time steps for each earthquake motion. During analysis, if convergence was not achieved, the integration time step was reduced by a factor of 10 until the analysis converged. The analysis then continued using the initial integration time step.

Table 3.8 Summary table of the fourteen analyses and associated number of total and iteration analysis time steps

Type	Location	Year	Station	Component	NPTS	Motion dt	Scale Factor
CRUSTAL	Loma Prieta, CA	1989	Fremont	090	7949	0.005	2.320
	Loma Prieta, CA	1989	Salinas	250	7990	0.005	2.794
	Loma Prieta, CA	1989	Saratoga	090	7991	0.005	1.048
	Loma Prieta, CA	1989	Hollister	090	11991	0.005	1.609
	Landers, CA	1992	Yermo Fire Sta.	360	8800	0.005	1.826
	San Fernando, CA	1971	LA Hollywood	090	5600	0.005	1.451
	Loma Prieta, CA	1989	Gilroy	000	7990	0.005	1.025
SUBDUCTION ZONE	Tohoku, Japan	2011	IWTH1611	E-W	60240	0.005	2.192
	Tohoku, Japan	2011	FKSH0311	N-S	60052	0.005	2.327
	Tohoku, Japan	2011	IWTH1111	N-S	60240	0.005	2.297
	Tohoku, Japan	2011	MYGH0911	N-S	60060	0.005	0.970
	Tohoku, Japan	2011	AOMH1211	N-S	60036	0.005	2.762
	Maule, Chile	2010	Maipu	E-W	33402	0.005	0.766
	Maule, Chile	2010	Viña del Mar	N-S	25004	0.005	1.541

The response parameters that were recorded during the nonlinear dynamic time-history analyses include:

- nodal displacements relative to bedrock
- nodal absolute accelerations
- element forces in linear elastic beam-column elements (deck)
- fiber-section forces and deformations in nonlinear beam-column elements (pile and column)
- steel reinforcement, unconfined concrete, and confined concrete (nonlinear beam-column) fiber-section stress and strain at selected locations
- soil-interface spring and gap element forces and deformations (p-y, t-z, q-z, and gap)
- soil element (9-4-QuadUP) stress and strains

The recorded response parameters were further reduced to the following engineering parameters:

- Bridge deck and soil column lateral displacement envelopes: defined as the absolute maximum values of positive and negative nodal displacements relative to bedrock.
- Bridge column and pile overturning moment envelopes: defined as the absolute maximum values of positive and negative overturning moment at the formation of plastic hinges in the column and in the pile.
- Bridge column and pile shear force envelopes: defined as the absolute maximum values of positive and negative shear forces in the column and in the pile.

- Column rotation, θ_R: defined as the absolute values of peak column rotation. The yield rotation, θ_y, corresponds to the curvature at the point of first yield of the moment-curvature analysis multiplied by the effective plastic hinge length.

- Number of inelastic excursions: The number of times that the value of the column rotation exceeds the yield rotation defined in the previous bullet point.

Chapter 4 Results

The sub-components of the soil-foundation-bridge system were validated by examining the individual seismic response of each sub-component To complete this process, two earthquake motions were selected for validation purposes — one shallow, crustal earthquake motions (1992 Landers, California, Yermo Fire Station) and one subduction zone earthquake motion (2011 Tohoku, Japan, IWTH1111 Station). These two input earthquake motions were selected because of the large spectral acceleration at the first fundamental period (T_1 = 0.89 s) of the soil-foundation-bridge system. Table 4.1 lists earthquake information for the two earthquake motions.

Figures 4.1 and 4.2 display the input acceleration-, velocity-, and displacement-time series for the two scaled earthquake motions. Figure 4.1 shows that the Landers earthquake motion contains a strong velocity pulse, which indicates that it is a near-fault motion with forward-directivity effects (Somerville et al., 1997). Figure 4.2 exhibits the intensity and long-duration characteristics of the Japan earthquake motion, which was recorded approximately 240 km from the epicenter of the earthquake. The velocity pulse of the Landers motion is evident in the displacement-time series when, between the second and third peaks, the total amplitude of displacement from one peak to the other is approximately 100 cm. It is important to note that the displacement only exceeds a peak-to-peak displacement of 10 cm five times. Conversely, the Tohoku, Japan displacement-time series never exceeds a peak-to-peak displacement of 20 cm, yet exceeds a peak-to-peak displacement of 10 cm fifteen times.

4.1 Deformed Shapes

All soil-foundation-bridge nodal displacements, relative to bedrock, are presented at the various loading stages of both analyses in Figures 4.3 through 4.8. They include: gravity application to the soil column, gravity application to the bridge deck, and dynamic loading.

Table 4.1 Summary table of the two selected scaled earthquake motions. M_w, R_{rup}, PGA, S_a at the system first fundamental period, SF, I_A, and D_{5-95} are included.

Location	Date	Station	Component	M_w	R_{rup}/R_{epi} (km)	PGA (g)	S_a @ T_1=0.89 s (g)	SF	I_A (m/s)	D_{5-95} (s)
Landers, CA	1992	Yermo Fire	360	7.3	23.6	0.27	0.79	1.826	2.26	18.86
Tohoku, Japan	2011	IWTH1111	N-S	9.0	260	0.33	1.04	2.297	6.97	102.36

M_w - Moment Magnitude
R_{rup}/R_{epi} - Rupture/Epicentral distance
PGA - Peak Ground Acceleration
SF - Scale Factor
I_A - Arias Intensity
D_{5-95} - Significant Duration

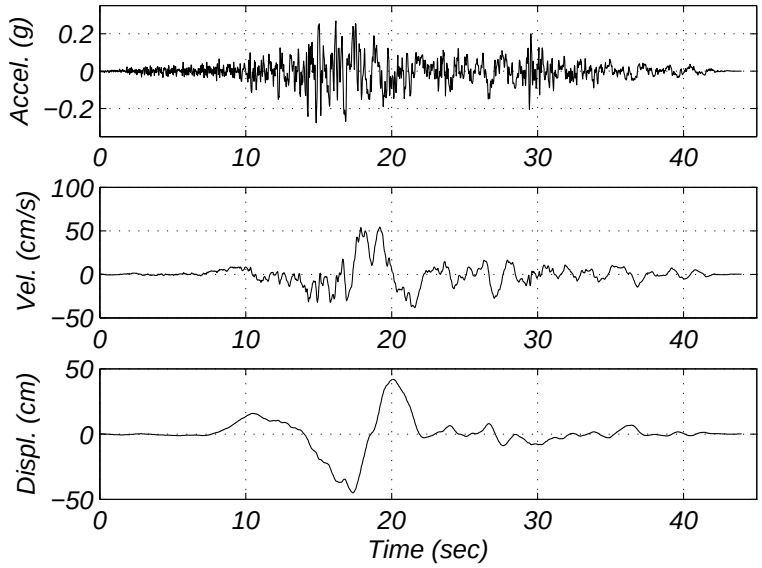

Figure 4.1 Landers, California, Yermo Fire Station, 360, input acceleration-, velocity-, and displacement-time series

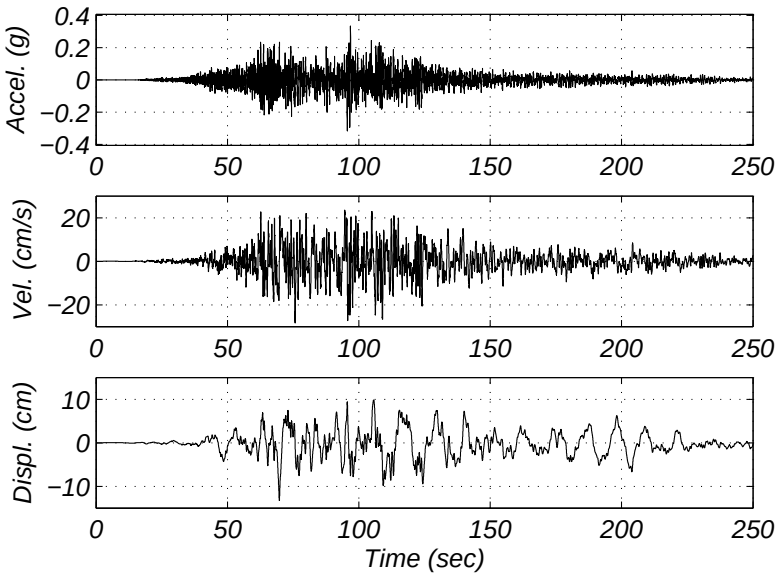

Figure 4.2 Tohoku, Japan, IWTH1111 Station, N-S, input acceleration-, velocity-, and displacement-time series

A scaling factor of 100 was used to magnify the deformations in the soil-foundation-bridge system for all deformed shape figures presented in this section. All nodes were set based on the reference point (0,0), where the base of the pile is founded on bedrock. Single lines were used to connect the bridge nodes. Green lines show the deformations in the bridge structure and the gray lines show the original, un-deformed shape of the bridge. The thickness of the lines were increased to simulate the appearance of the bridge pile, column, and deck. Because zero-length soil spring elements were used to connect the pile and soil column, the nodes for the pile and soil column are located at the same point. For this reason the line representing the pile overlaps the soil mesh. The lines connecting each soil element within the soil mesh was filled with color to represent the soil column. The yellow soil elements depict the deformed shape of the soil, and the red mesh shows the original, un-deformed shape.

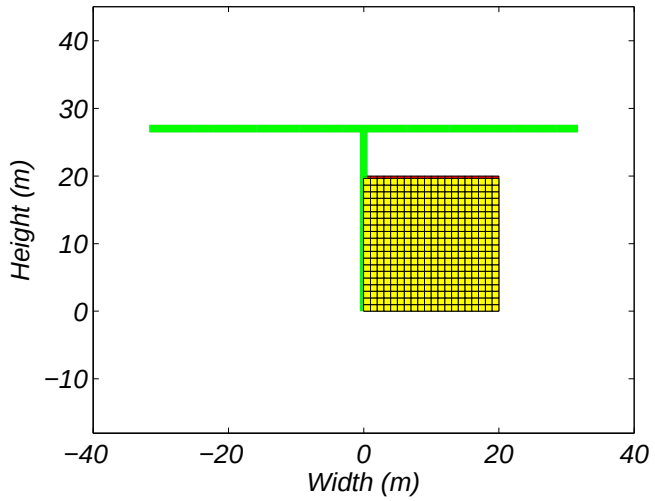

Figure 4.3 Displacement in the soil-foundation-bridge system due to applied soil gravity load (self-weight). A scaling factor of 100 was used to magnify the deformations in the soil-foundation-bridge system.

For analysis, the soil gravity load (self-weight) is applied first, to simulate pre-construction subsurface conditions, and only prior to applying the structure gravity loads (self-weight),

were the pile and soil column connected by the nonlinear soil-interface springs. Figures 4.3 and 4.4 illustrate the deformations due to soil gravity loading and bridge gravity loading, respectively.

Figures 4.5 and 4.6 show the maximum lateral deformations at the soil surface due to the 1992 Landers, California, Yermo Fire Station, shallow, crustal earthquake motion and 2011 Tohoku, Japan, IWTH1111 Station, subduction zone earthquake motion, respectively. Note the difference in magnitude of horizontal displacement of the subduction zone versus the crustal earthquake motion.

Figures 4.7 and 4.8 show the maximum lateral deformations at mid-span of the bridge deck due to the shallow, crustal and subduction zone earthquake motions, respectively. Note that, in both figures, the pile appears to form a plastic hinge at approximately a normalized depth of three.

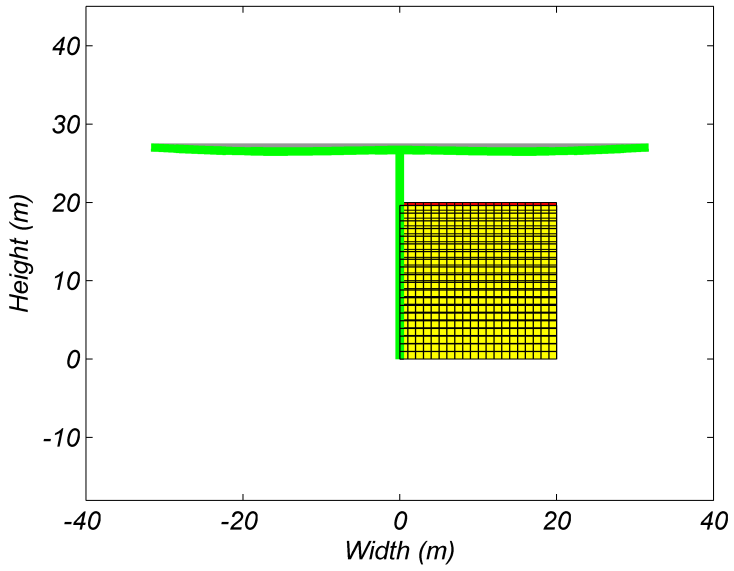

Figure 4.4 Displacement in the soil-foundation-bridge system due to applied soil and structure gravity loads (self-weight). A scaling factor of 100 was used to magnify the deformations in the soil-foundation-bridge system.

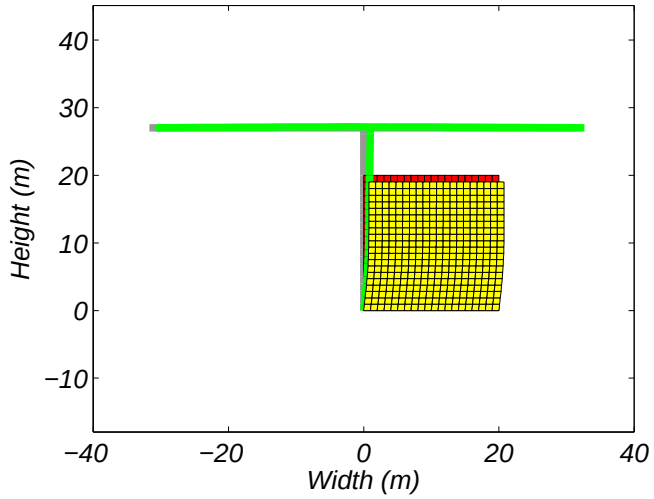

Figure 4.5 Displaced shape at the instant when peak lateral displacement is attained in soil at ground surface (t = 43.920 sec) due to 1992 Landers, California, Yermo Fire Station earthquake motion. A scaling factor of 100 was used to magnify the deformations in the soil-foundation-bridge system.

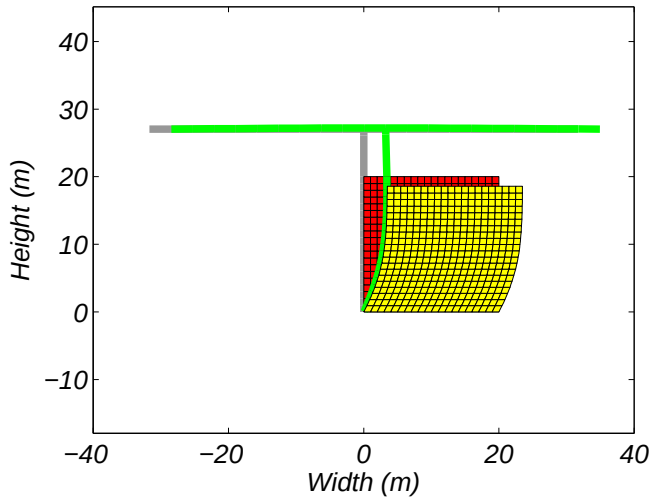

Figure 4.6 Displaced shape at the instant when peak lateral displacement is attained in soil at ground surface (t = 97.775 sec) due to 2011 Tohoku, Japan, IWTH1111 Station earthquake motion. A scaling factor of 100 was used to magnify the deformations in the soil-foundation-bridge system.

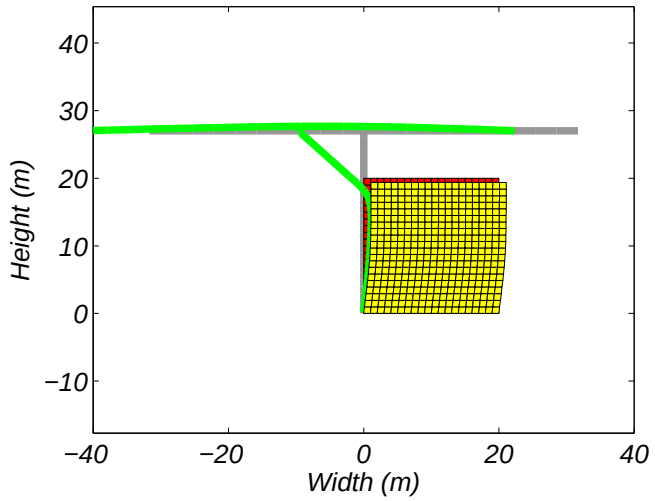

Figure 4.7 Displaced shape at the instant when peak lateral displacement is attained in soil at ground surface (t = 20.105 sec) due to 1992 Landers, California, Yermo Fire Station earthquake motion. A scaling factor of 100 was used to magnify the deformations in the soil-foundation-bridge system.

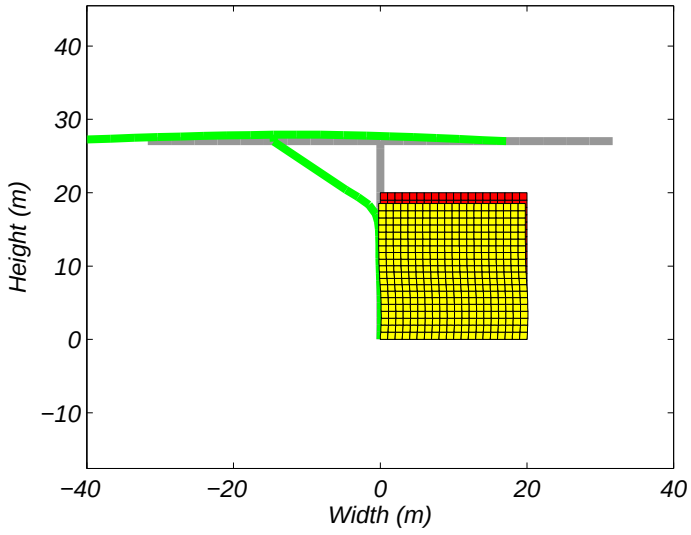

Figure 4.8 Displaced shape at the instant when peak lateral displacement is attained in soil at ground surface (t = 72.065 sec) due to 2011 Tohoku, Japan, IWTH1111 Station earthquake motion. A scaling factor of 100 was used to magnify the deformations in the soil-foundation-bridge system.

4.2 Element Forces and Deformations

This section presents the axial load, overturning moment, and shear force in the column and pile for times at which each parameter reaches a maxima. The axial load is normalized by the design axial load, P_D = 3483 kN, the overturning moment is normalized by the moment at first yield, M'_Y = 2720 kN-m, and the shear force is normalized by the seismic weight, W_S = 7180 kN. The seismic weight was taken as the weight of the structure above the ground surface. The displacement is presented as peak horizontal displacement in the column and soil, which are normalized by the maximum displacement of the column. Each parameter is plotted against the depth normalized by the column/pile diameter. Similarly, a normalized depth of zero represents the soil surface, positive normalized depth values represent the bridge column, and negative normalized depth values represent the pile/soil.

Each of Figures 4.9 through 4.14 present the peak column and pile axial load, overturning moment, shear force, and displacement for the Landers, California and Tohoku, Japan earthquake motions, respectively. It should be noted that, for the Landers earthquake motion, the peak axial force, overturning moment, and shear force in the column and pile exceed that of the Tohoku, Japan earthquake motion. The maximum bending moment in the pile for the Tohoku, Japan earthquake motion, Figure 4.13, approaches the first yielding moment, M'_y, while, in the Landers earthquake motion, Figure 4.10, the maximum bending moment in the pile exceeds the first yield moment. Therefore, a plastic hinge formed during the Landers, California earthquake and a plastic hinge began to form during the Tohoku, Japan earthquake.

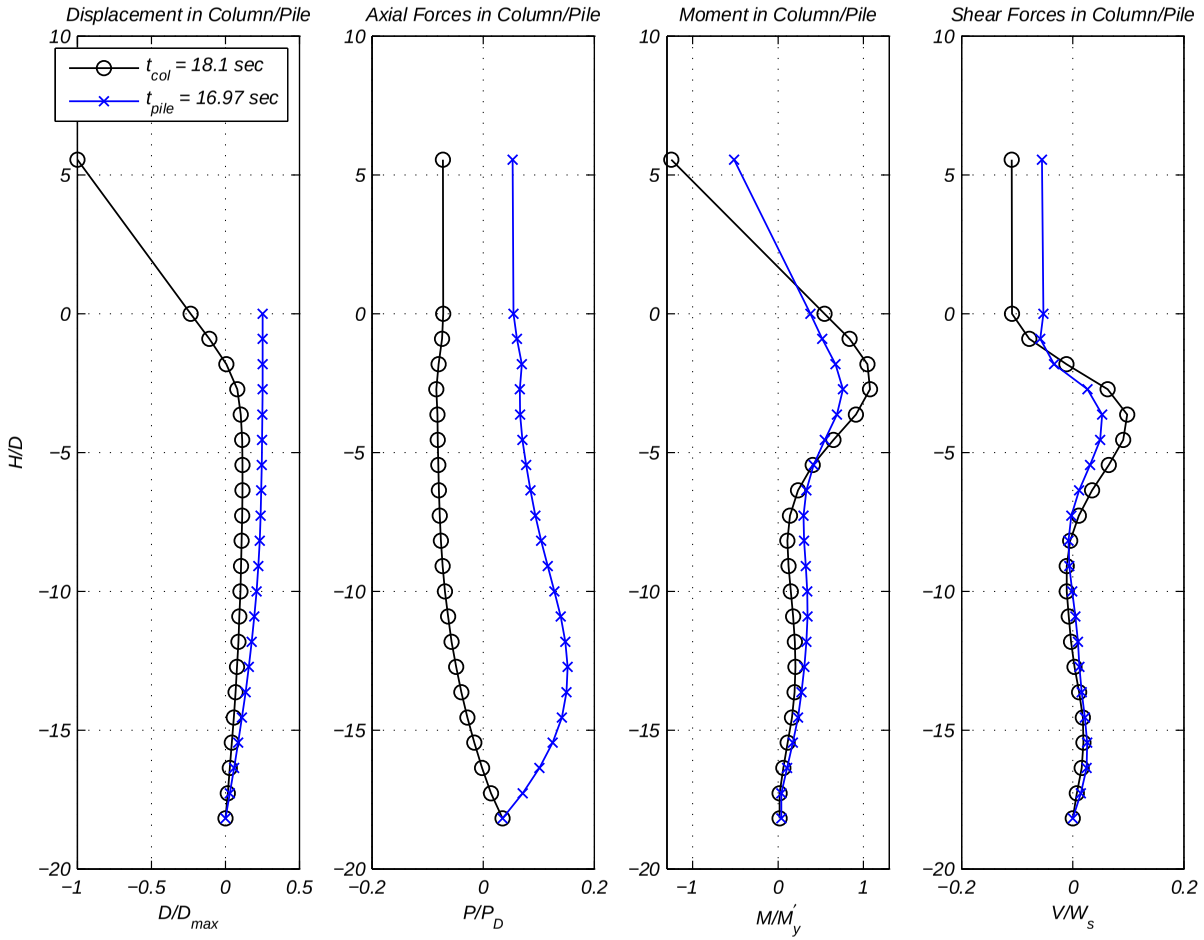

Figure 4.9 Column Forces at peak lateral displacement in soil and deck due to 1992 Landers, California, Yermo Fire Station earthquake motion. The displacements of the soil (denoted by pile subscript) and column are presented in the first figure whereas the other three figures present the forces in the column and pile.

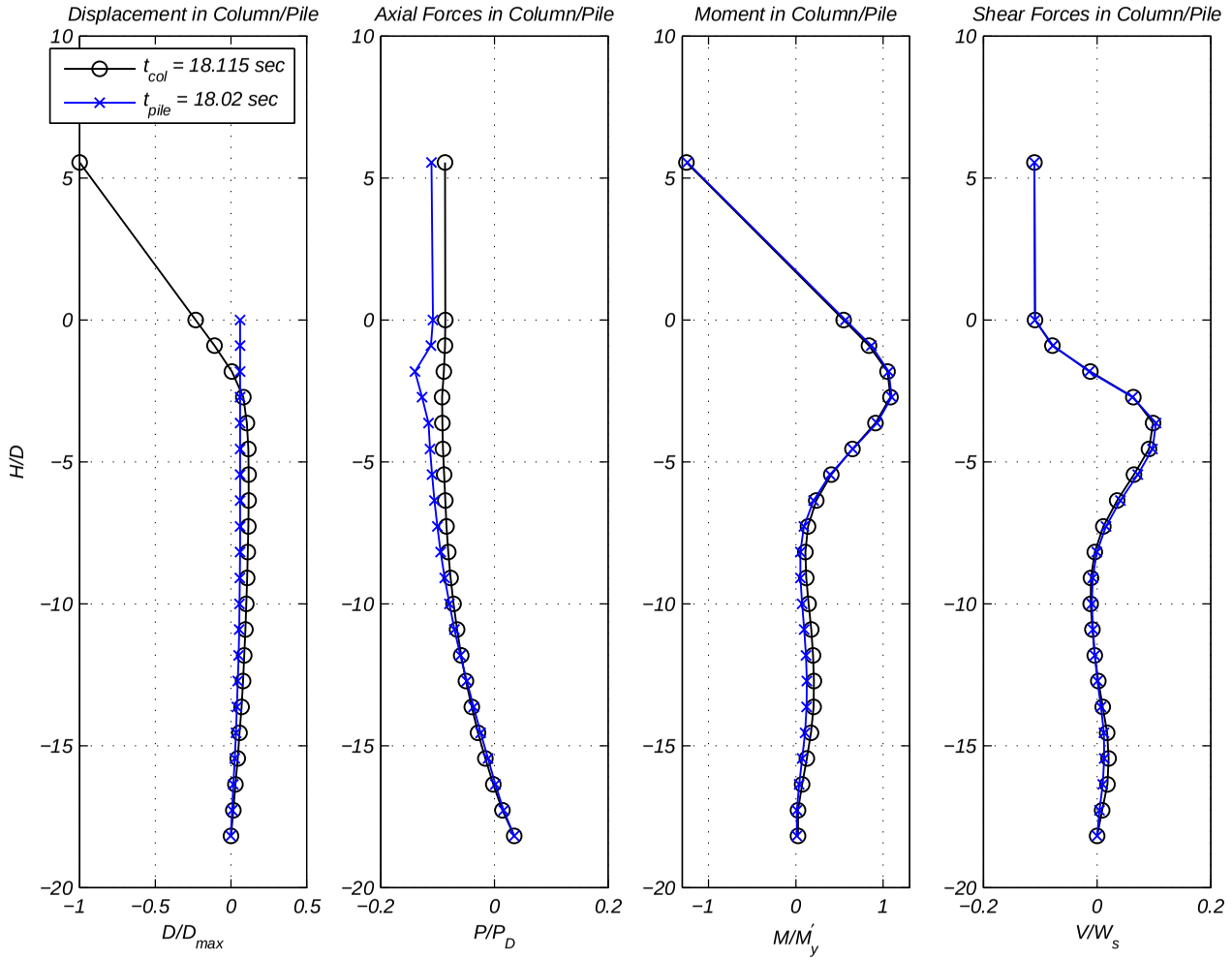

Figure 4.10 Column Forces at peak overturning moment in pile and at the top of the column due to 1992 Landers, California, Yermo Fire Station earthquake motion. The displacements of the soil (denoted by pile subscript) and column are presented in the first figure whereas the other three figures present the forces in the column and pile.

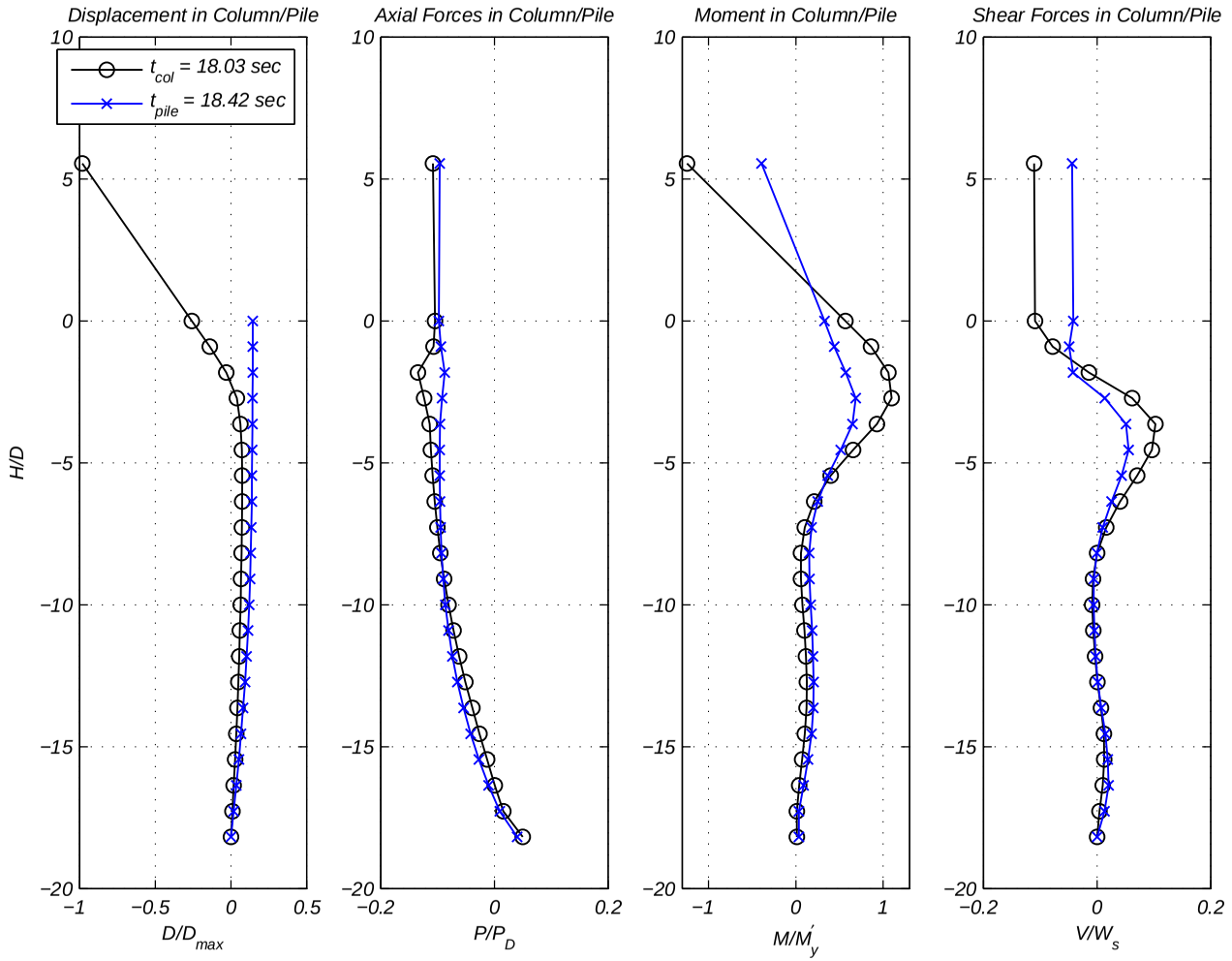

Figure 4.11 Column Forces at peak shear in pile and at the top of the column due to 1992 Landers, California, Yermo Fire Station earthquake motion. The displacements of the soil (denoted by pile subscript) and column are presented in the first figure whereas the other three figures present the forces in the column and pile.

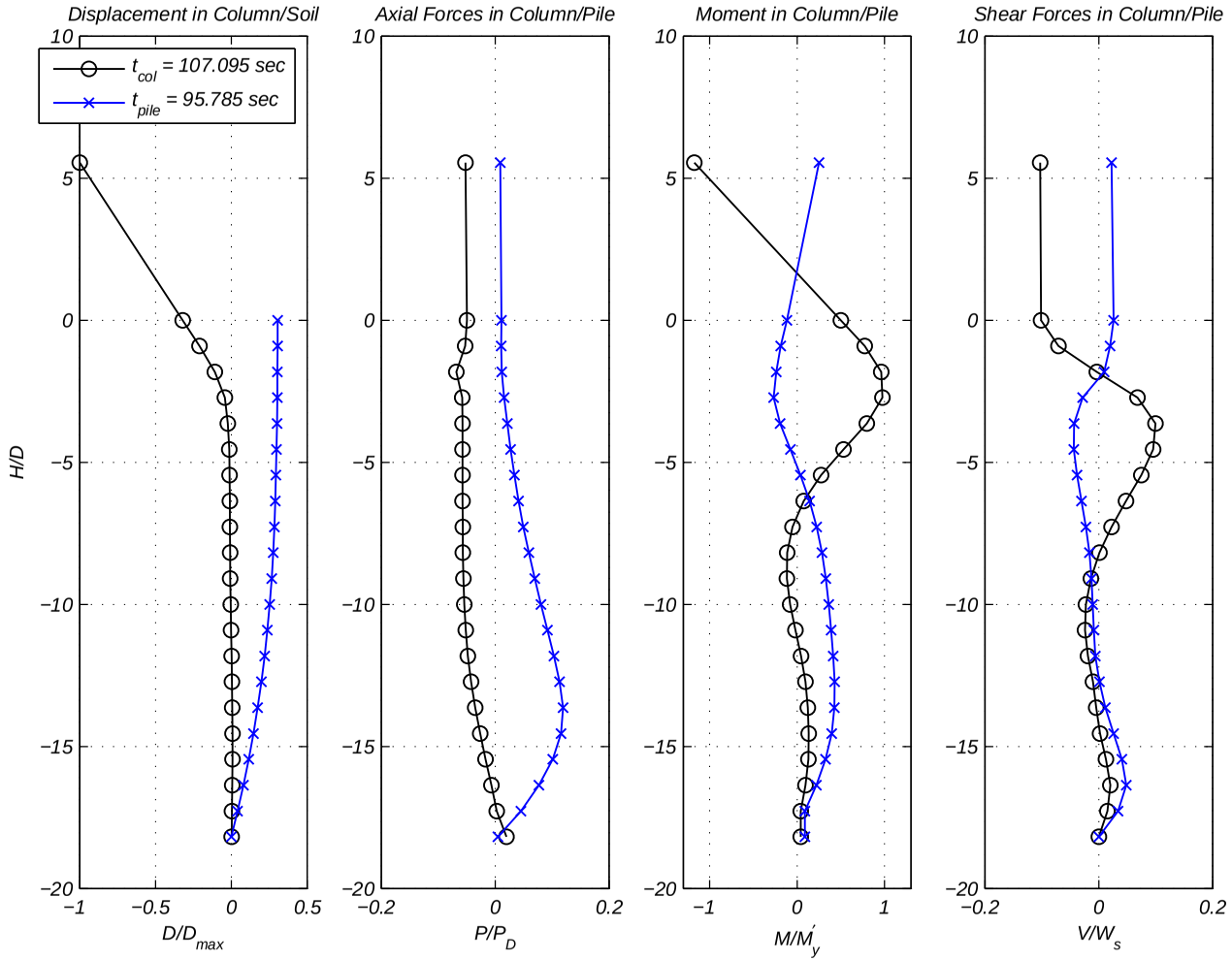

Figure 4.12 Column Forces at peak lateral displacement in soil and deck due to 2011 Tohoku, Japan, IWTH1111 Station earthquake motion. The displacements of the soil (denoted by pile subscript) and column are presented in the first figure whereas the other three figures present the forces in the column and pile.

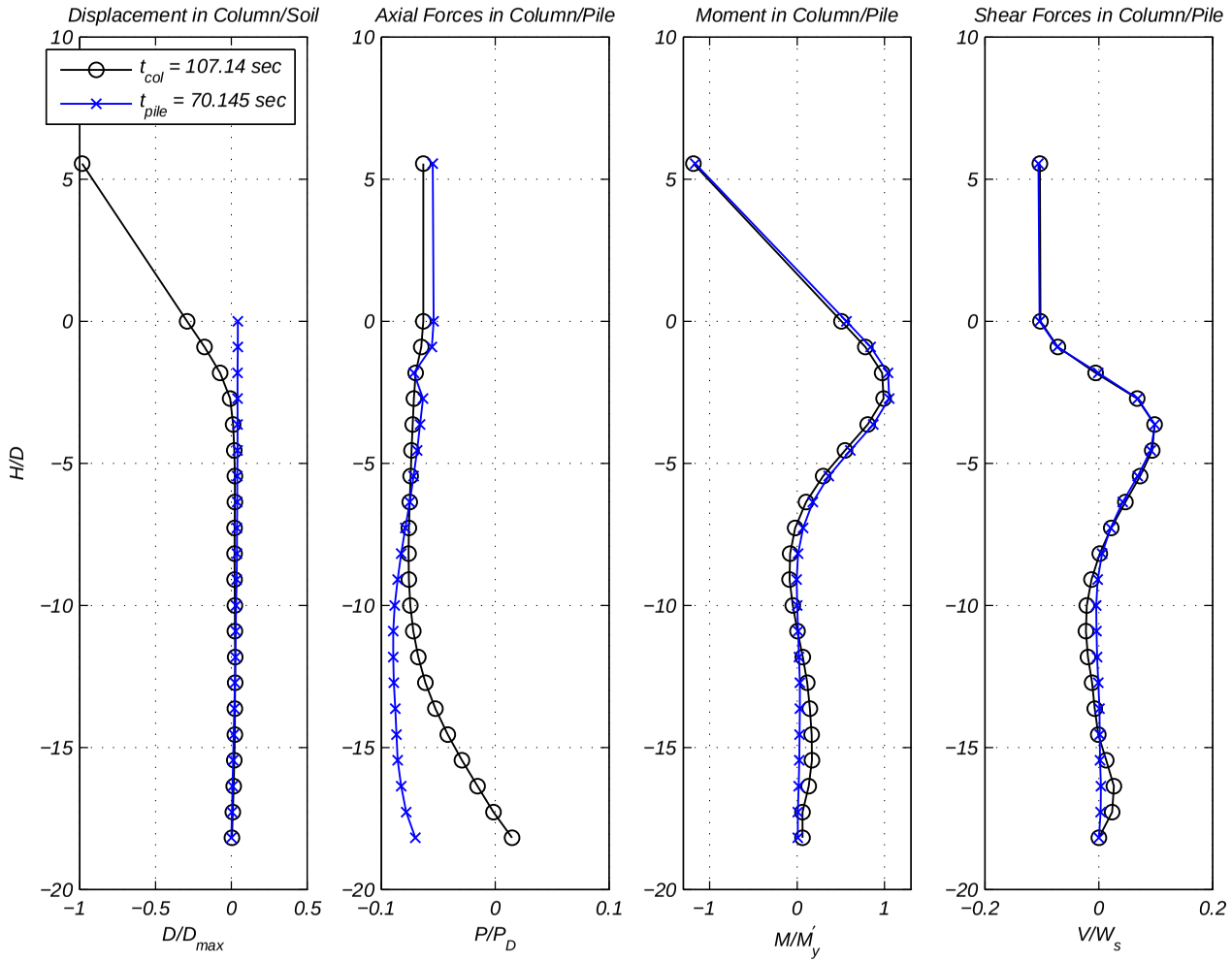

Figure 4.13 Column Forces at peak overturning moment in pile and at the top of the column due to 2011 Tohoku, Japan, IWTH1111 Station earthquake motion. The displacements of the soil (denoted by pile subscript) and column are presented in the first figure whereas the other three figures present the forces in the column and pile.

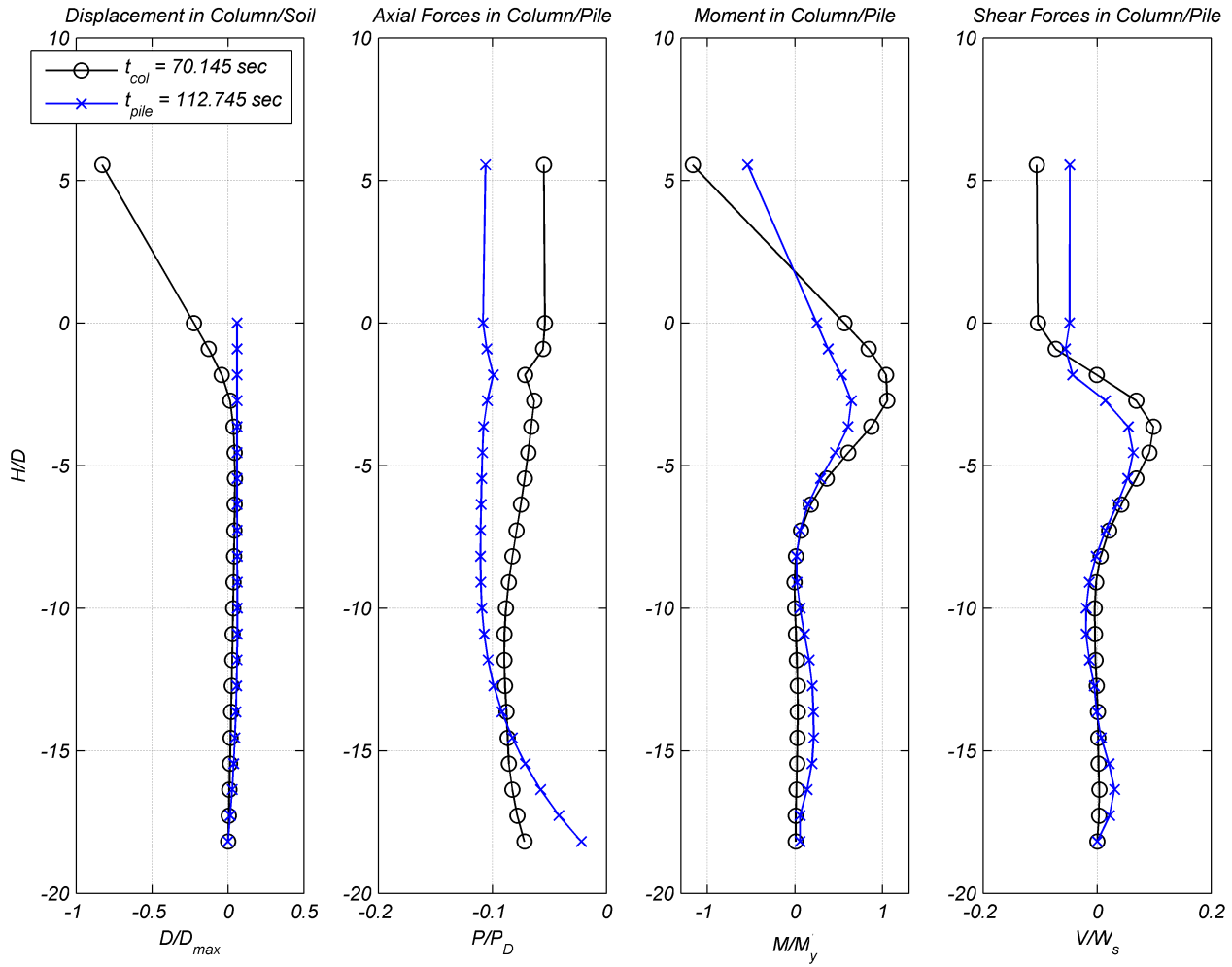

Figure 4.14 Column Forces at peak shear in pile and at the top of the column due to 2011 Tohoku, Japan, IWTH1111 Station earthquake motion. The displacements of the soil (denoted by pile subscript) and column are presented in the first figure whereas the other three figures present the forces in the column and pile.

4.3 Stress-Strain in Fiber-Section

Figures 4.15 through 4.18 show the stress-strain response of the confined and unconfined concrete for the Landers, California and Tohoku, Japan earthquake motions, respectively. It should be noted that positive stress and positive strain represent tension and negative stress and negative strain represent compression. It is apparent that the tensile capacity of the confined and unconfined concrete is exceeded for both earthquake motions. Additionally, the compressive response of the confined concrete is notable. Over 60% of the compressive capacity is experienced during the Landers earthquake motion and only 50% during the Tohoku earthquake motion.

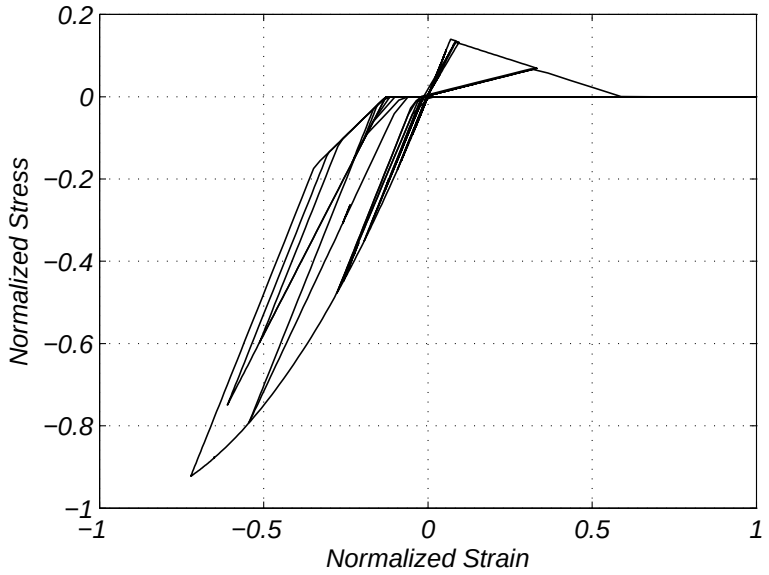

Figure 4.15 Stress-strain curve for the confined concrete fiber-section at the top of the column due to the Landers, California earthquake motion

The compressive strength of the unconfined concrete cover, shown in Figures 4.17 and 4.18, reaches 100% of its resistance and therefore the column experiences spalling of the cover. The ability to resist the dynamic loading is decreased, especially during the Landers earthquake motion, after 100% of the compressive strength is reached. The num-

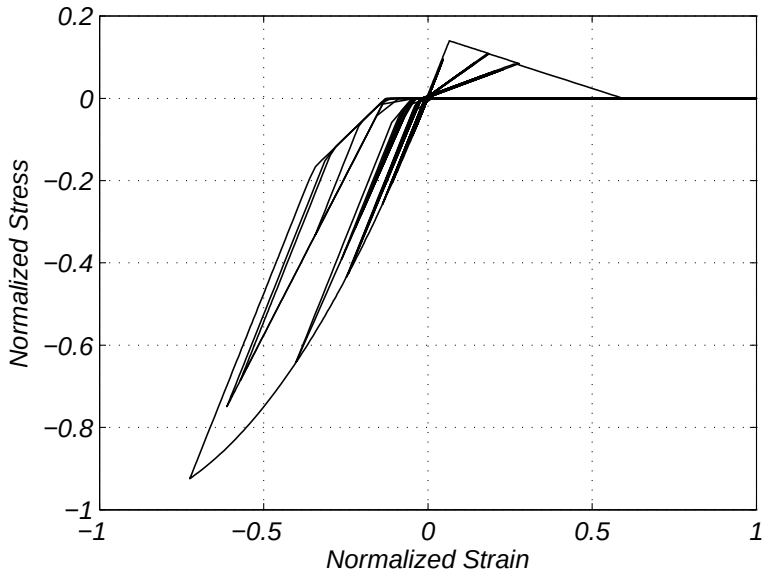

Figure 4.16 Stress-strain curve for the confined concrete fiber-section at the top of the column due to the Tohoku, Japan earthquake motion

ber of times that 100% of the strain is exceeded for the Landers earthquake motion is three and for the Tohoku earthquake motion is one.

Figures 4.19 and 4.20 illustrate the stress-strain response of the steel reinforcement at the top of the bridge column for Landers, California and Tohoku, Japan, respectively. First, the number of yielding cycles for the Tohoku earthquake motion is double that for the Landers earthquake motion. The general shape of the stress-strain curve in both figures is similar, but the Tohoku earthquake motion shows a single instant at which the response of the column changes. Additionally, the intense pulse-like characteristics of the Landers earthquake motion are apparent, because it only requires one hysteretic cycle to exceed 100% of the stress and strain in the column, while the Tohoku earthquake motion has an initial cycle preceding the yield cycle.

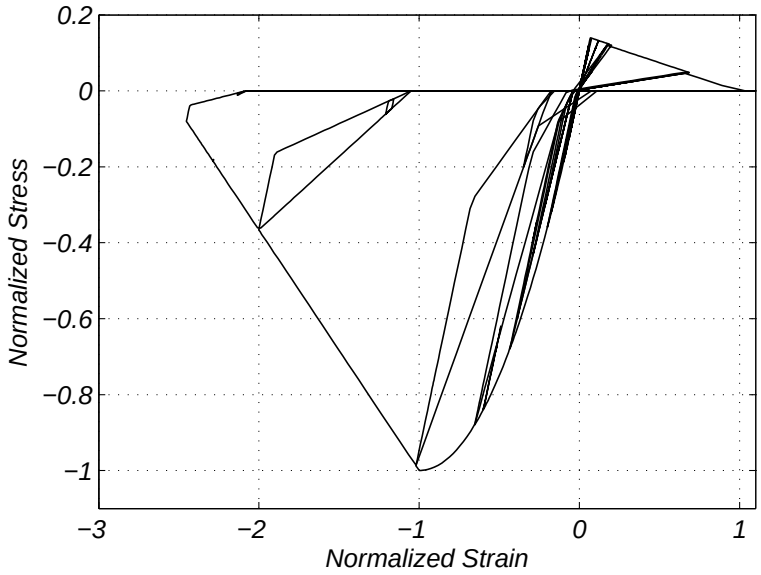

Figure 4.17 Stress-strain curve for the unconfined concrete fiber-section at the top of the column due to the Landers, California earthquake motion

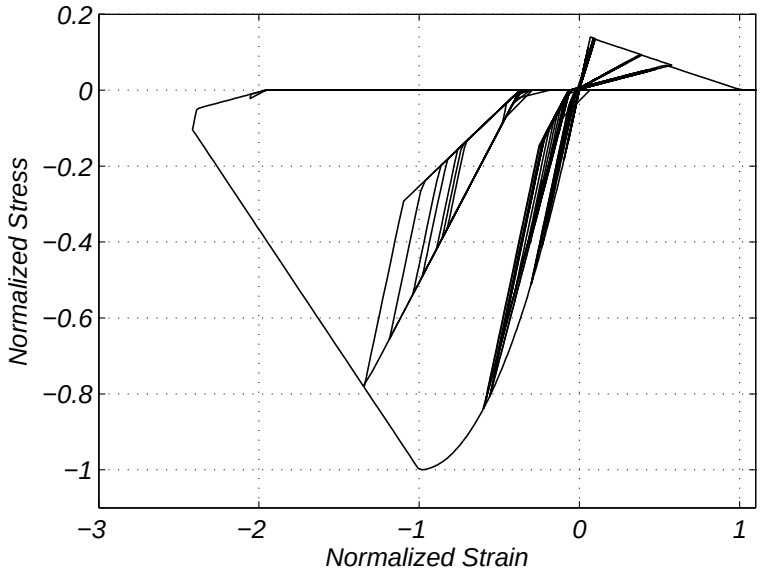

Figure 4.18 Stress-strain curve for the unconfined concrete fiber-section at the top of the column due to the Tohoku, Japan earthquake motion

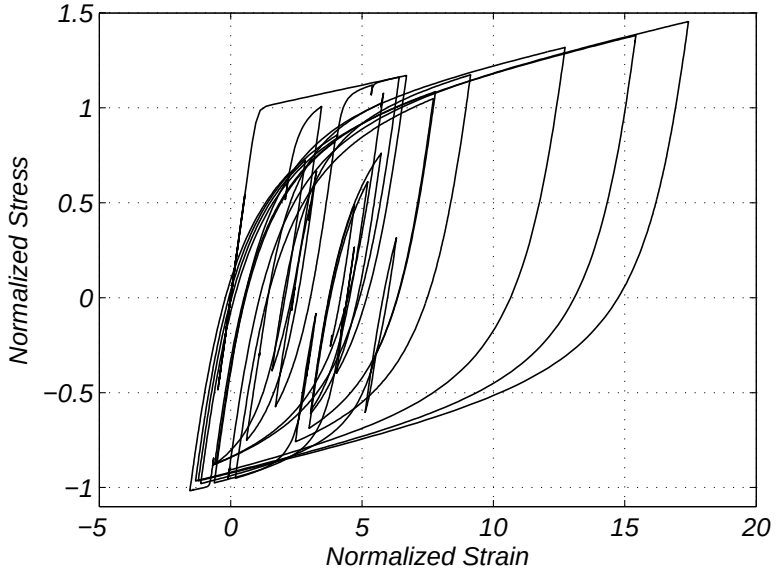

Figure 4.19 Stress-strain curve for the steel reinforcement fiber-section at the top of the column due to the Landers, California earthquake motion

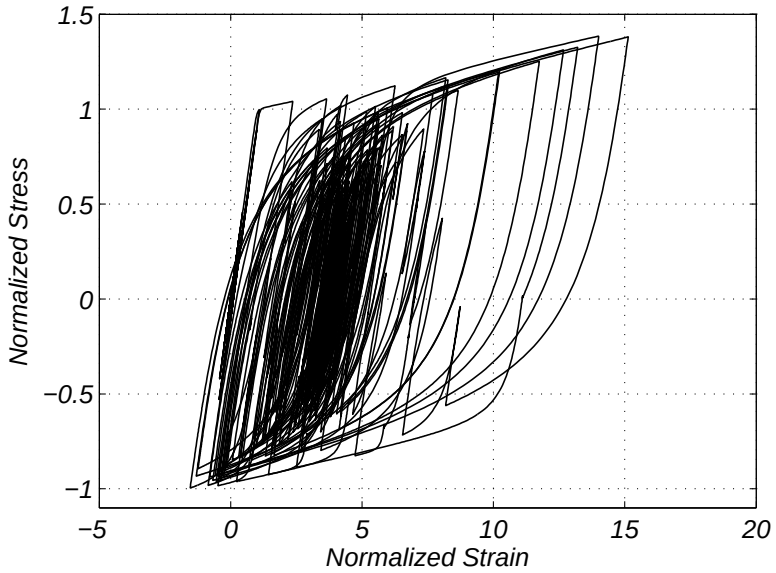

Figure 4.20 Stress-strain curve for the steel reinforcement fiber-section at the top of the column due to the Tohoku, Japan earthquake motion

4.4 Lateral Soil-Interface Springs

Figure 4.21 illustrates the lateral force, P, in the p-y soil-interface springs normalized by the ultimate resistance, p_{ult}, defined at each depth increment for both Landers and Tohoku earthquake motions at time of maximum bending moment. The point at which the lateral spring force is maximum occurs at the same depth as the plastic hinge formation in the pile. Therefore, Figure 4.21 corroborates the results that illustrate the formation of a plastic hinge in the pile (i.e. Figures 4.7 and 4.8). The largest lateral forces occur above the location of the plastic hinge, thus inducing large rotations in the pile just below the lateral load.

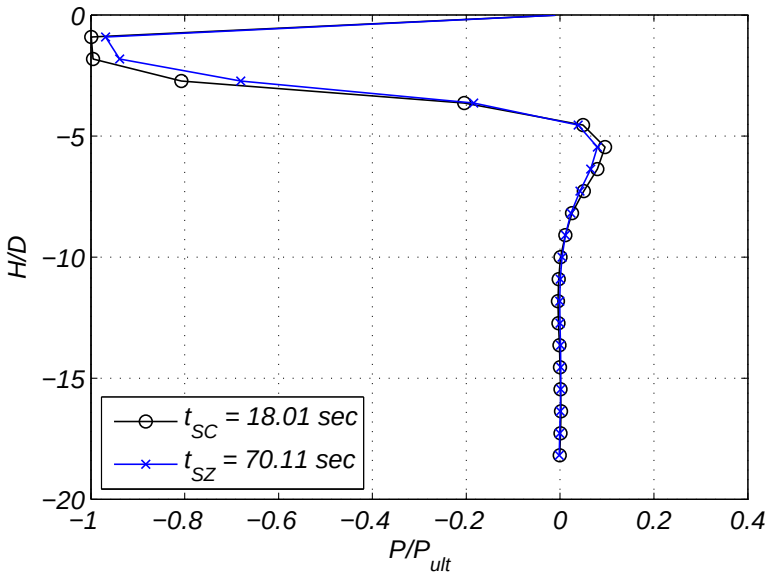

Figure 4.21 Lateral force in p-y soil-interface spring normalized by the ultimate resistance defined at each depth increment for both Landers [shallow, crustal (SC)] and Tohoku [subduction zone(SZ)] earthquake motions at time of maximum bending moment.

4.5 Yield Rotation - Number of Inelastic Excursions

Figures 4.22 through 4.35 illustrate the number of inelastic excursions with respect to the effective plastic hinge rotation, θ_{lp}, computed by,

$$\theta_{lp} = \phi \times L_p \tag{4.1}$$

where ϕ is the curvature and L_p is the effective plastic hinge length after Paulay and Priestly (1992). The yield rotation, θ_Y, corresponds to the curvature at the point of first yield, ϕ_Y, of the moment-curvature analysis multiplied by the effective plastic hinge length. The number of inelastic excursions is defined as the number of peaks exceeding the yield rotation, θ_Y, as shown in Figures 4.22 through 4.35. To illustrate the effects of duration, the number of inelastic excursions is plotted against five intensity measures: peak ground acceleration (PGA), cumulative absolute velocity (CAV), significant duration (D_{5-95}), Arias Intensity (I_A), and pseudo-spectral acceleration (S_a). Accordingly, initial implications about structural damage performance are elicited.

Table 4.2 summarizes the number of inelastic excursions and the five intensity measures for all fourteen earthquake motions used to analyze the soil-foundation-bridge system. Table 4.3 reports the mean, median, standard deviation, and coefficient of variation of the number of inelastic excursions for crustal and subduction zone earthquake motions.

Table 4.3 illustrates an important difference between the two earthquake motion types. The mean and median number of inelastic excursions for the subduction zone earthquake motions are 5 and 6 times greater than for the shallow, crustal earthquake motions, respectively. The standard deviation shows an increase in scatter for the subduction zone earthquake motions compared to that of the crustal earthquake motions. Although the coefficient of variation verifies the aforementioned conclusion, it also shows that both types

Table 4.2 Summary table of PGA, CAV, D_{5-95}, I_A, and S_a for the fourteen earthquake motions

Type	Earthquake	Year	Station	Eqke #	# of Inelastic Excursions	PGA (g)	D_{5-95} (s)	I_A (m/s)	S_a @ T_1=0.89s (g)	CAV (m/s)
CRUSTAL	Loma Prieta, CA	1989	Fremont	NGA761	28	0.43	17.24	1.67	0.56	12.49
	Loma Prieta, CA	1989	Salinas	NGA800	22	0.33	21.46	1.86	0.42	13.51
	Loma Prieta, CA	1989	Saratoga	NGA802	16	0.40	9.36	1.19	0.43	8.48
	Loma Prieta, CA	1989	Hollister	NGA776	31	0.29	28.75	2.00	0.79	16.91
	Landers, CA	1992	Yermo Fire Sta.	NGA900	24	0.27	18.86	2.26	0.79	15.97
	San Fernando, CA	1971	LA Hollywood	NGA068	21	0.32	11.17	1.37	0.63	9.04
	Loma Prieta, CA	1989	Gilroy	NGA768	25	0.42	13.84	1.24	0.50	9.50
SUBDUCTION ZONE	Tohoku, Japan	2011	IWTH1611	67	176	0.35	95.08	6.08	0.65	60.77
	Tohoku, Japan	2011	FKSH0311	26	141	0.31	96.33	5.04	0.75	52.64
	Tohoku, Japan	2011	IWTH1111	64	161	0.33	102.36	6.97	1.04	64.96
	Tohoku, Japan	2011	MYGH0911	96	124	0.31	104.68	4.91	0.96	50.49
	Tohoku, Japan	2011	AOMH1211	14	173	0.34	106.04	6.88	0.51	65.95
	Maule, Chile	2010	Maipu	1	37	0.37	33.77	2.88	0.43	24.91
	Maule, Chile	2010	Viña del Mar	4	48	0.34	30.62	4.50	1.19	35.86

PGA - peak ground acceleration

D_{5-95} - significant dutation

I_A - Arias Intensity

S_a - pseudo-spectral acceleration at the first fundamental period

CAV - cumulative absolute velocity

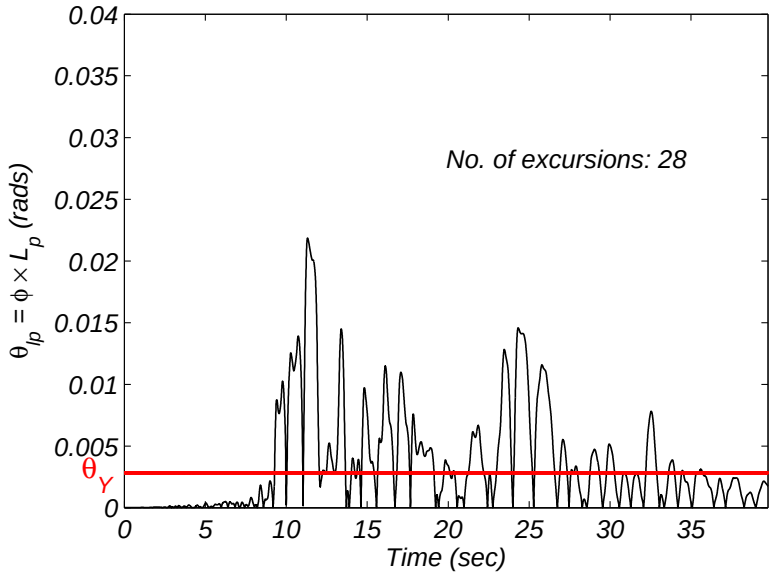

Figure 4.22 Effective plastic hinge rotation, θ_{lp}, for the Loma Prieta, California, Fremont Station earthquake motion. The yield rotation, θ_Y, corresponds to the curvature at the point of first yield, ϕ_Y, of the moment-curvature analysis multiplied by the effective plastic hinge length.

have a acceptable scatter.

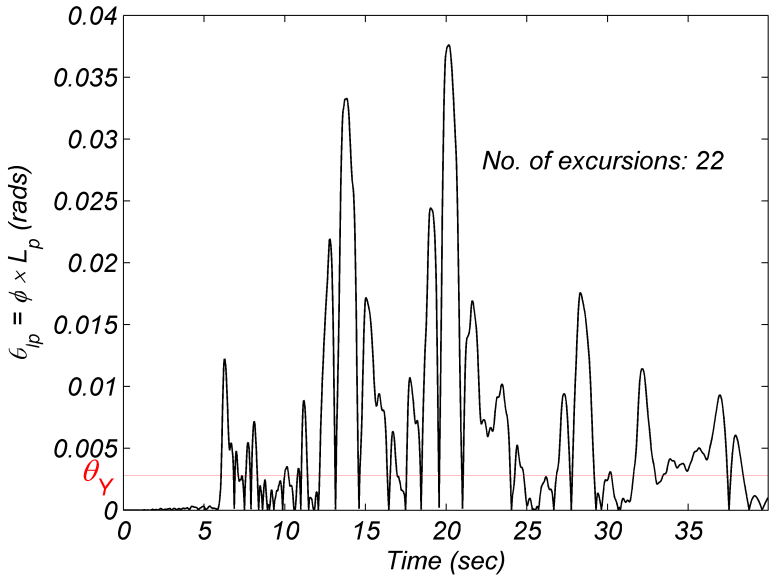

Figure 4.23 Effective plastic hinge rotation, θ_{lp}, for the Loma Prieta, California, Salinas Station earthquake motion. The yield rotation, θ_Y, corresponds to the curvature at the point of first yield, ϕ_Y, of the moment-curvature analysis multiplied by the effective plastic hinge length.

Table 4.3 Summary table of the mean, median, standard deviation, and coefficient of variation of the number of inelastic excursions for both crustal and subduction zone earthquake suites.

Earthquake Type	Mean	Median	Standard Deviation	COV
CRUSTAL	23.9	24.0	4.88	0.205
SUBDUCTION ZONE	122.9	141.0	57.9	0.471

COV - coefficient of variation

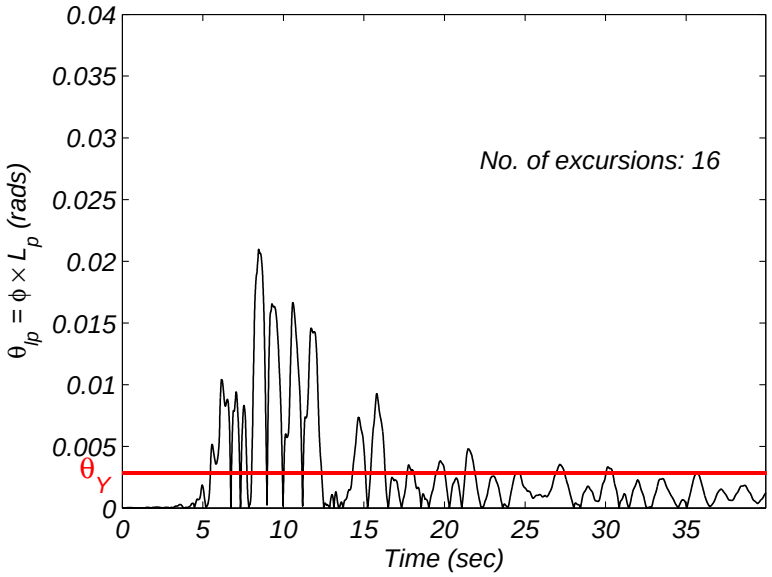

Figure 4.24 Effective plastic hinge rotation, θ_{lp}, for the Loma Prieta, California, Saratoga Station earthquake motion. The yield rotation, θ_Y, corresponds to the curvature at the point of first yield, ϕ_Y, of the moment-curvature analysis multiplied by the effective plastic hinge length.

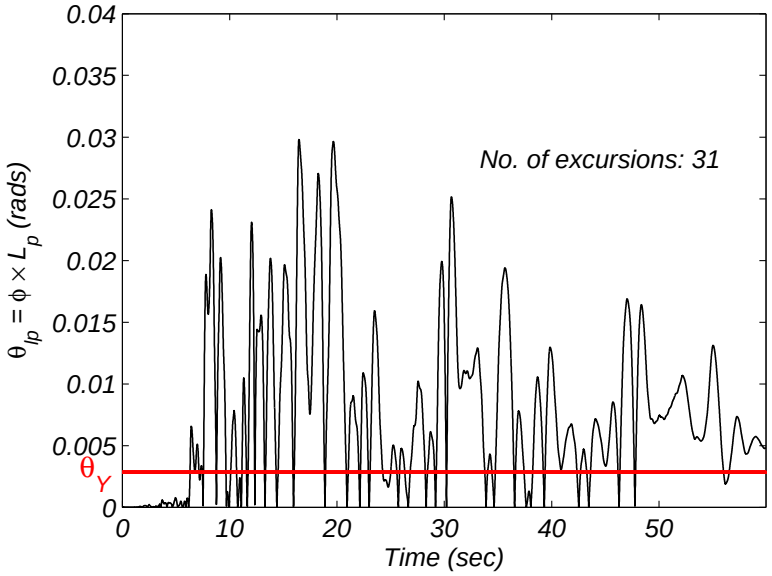

Figure 4.25 Effective plastic hinge rotation, θ_{lp}, for the Loma Prieta, California, Hollister Station earthquake motion. The yield rotation, θ_Y, corresponds to the curvature at the point of first yield, ϕ_Y, of the moment-curvature analysis multiplied by the effective plastic hinge length.

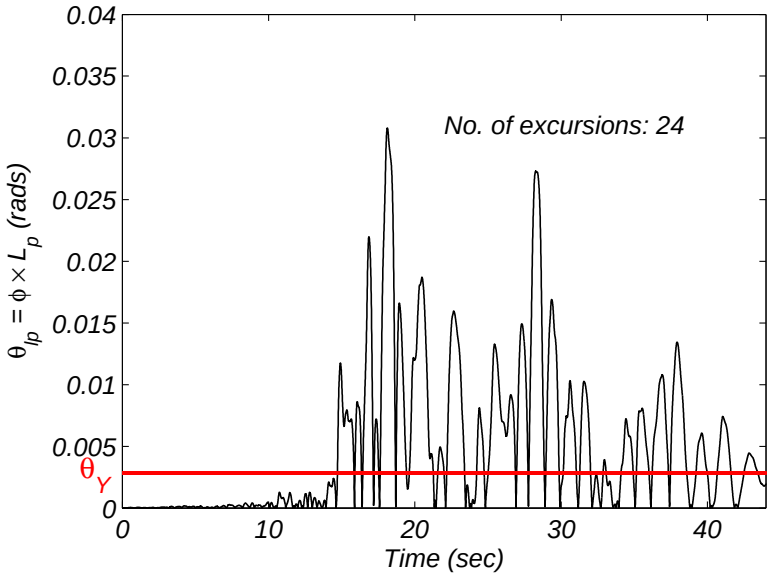

Figure 4.26 Effective plastic hinge rotation, θ_{lp}, for the Landers, California, Yermo Fire Station earthquake motion. The yield rotation, θ_Y, corresponds to the curvature at the point of first yield, ϕ_Y, of the moment-curvature analysis multiplied by the effective plastic hinge length.

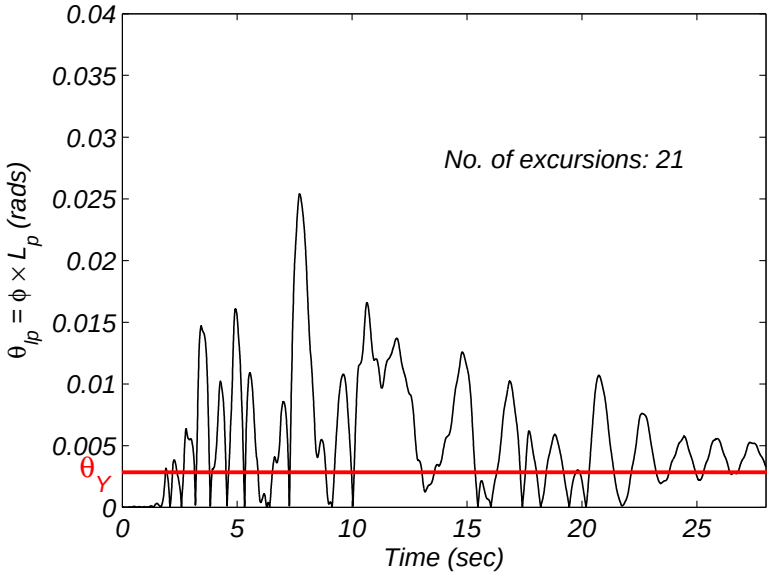

Figure 4.27 Effective plastic hinge rotation, θ_{lp}, for the San Fernando, California, LA Hollywood Station earthquake motion. The yield rotation, θ_Y, corresponds to the curvature at the point of first yield, ϕ_Y, of the moment-curvature analysis multiplied by the effective plastic hinge length.

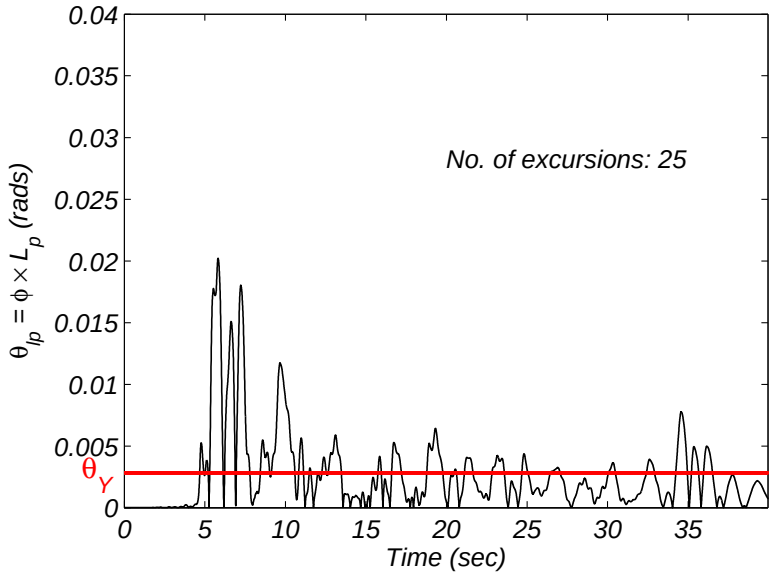

Figure 4.28 Effective plastic hinge rotation, θ_{lp}, for the Loma Prieta, California, Gilroy Station earthquake motion. The yield rotation, θ_Y, corresponds to the curvature at the point of first yield, ϕ_Y, of the moment-curvature analysis multiplied by the effective plastic hinge length.

Figures 4.36 through 4.40 illustrate the correlation of the number of inelastic excursions versus PGA, CAV, D_{5-95}, I_A, and S_a to both shallow, crustal earthquake motions and subduction zone earthquake motions. Figures 4.36 and 4.37 show no strong correlation between the two earthquake motion types to PGA or S_a. Conversely, CAV, D_{5-95}, and I_A show a definite distinction between the two types of earthquake motions. Notice, the majority of the subduction zone earthquake motions plot in the upper right-hand corner, and the shallow, crustal earthquake motions plot much closer to the origin.

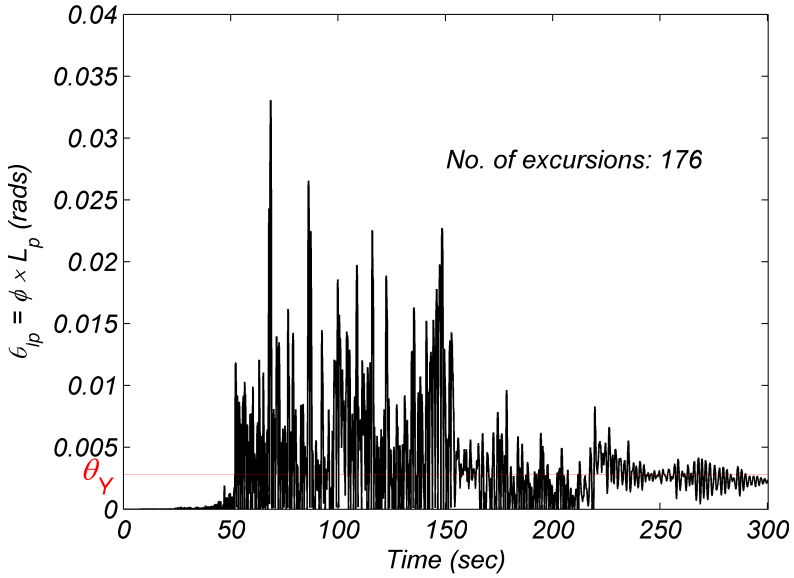

Figure 4.29 Effective plastic hinge rotation, θ_{lp}, for the Tohoku, Japan, IWTH1611 Station earthquake motion. The yield rotation, θ_Y, corresponds to the curvature at the point of first yield, ϕ_Y, of the moment-curvature analysis multiplied by the effective plastic hinge length.

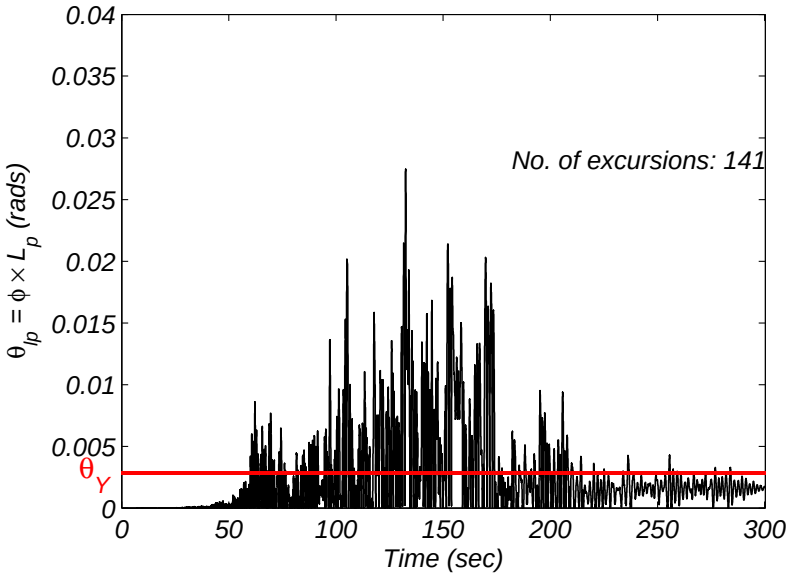

Figure 4.30 Effective plastic hinge rotation, θ_{lp}, for the Tohoku, Japan, FKSH0311 Station earthquake motion. The yield rotation, θ_Y, corresponds to the curvature at the point of first yield, ϕ_Y, of the moment-curvature analysis multiplied by the effective plastic hinge length.

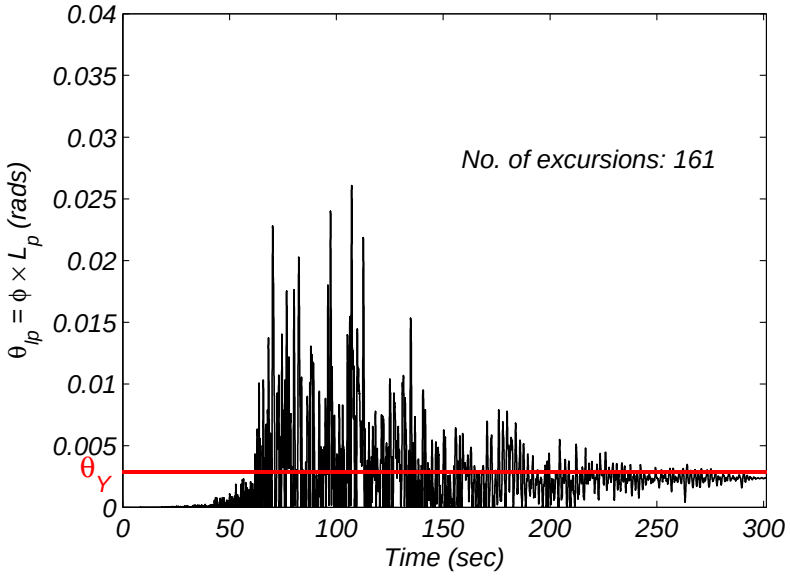

Figure 4.31 Effective plastic hinge rotation, θ_{lp}, for the Tohoku, Japan, IWTH1111 Station earthquake motion. The yield rotation, θ_Y, corresponds to the curvature at the point of first yield, ϕ_Y, of the moment-curvature analysis multiplied by the effective plastic hinge length.

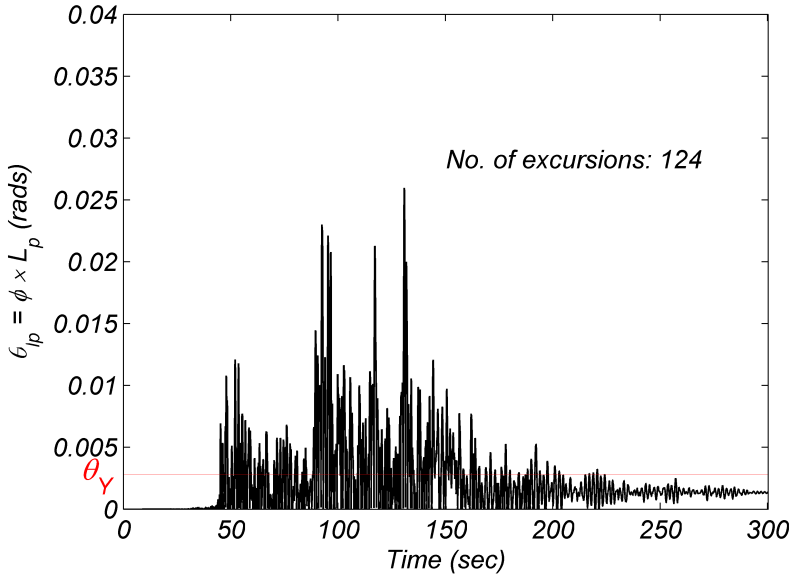

Figure 4.32 Effective plastic hinge rotation, θ_{lp}, for the Tohoku, Japan, MYGH0911 Station earthquake motion. The yield rotation, θ_Y, corresponds to the curvature at the point of first yield, ϕ_Y, of the moment-curvature analysis multiplied by the effective plastic hinge length.

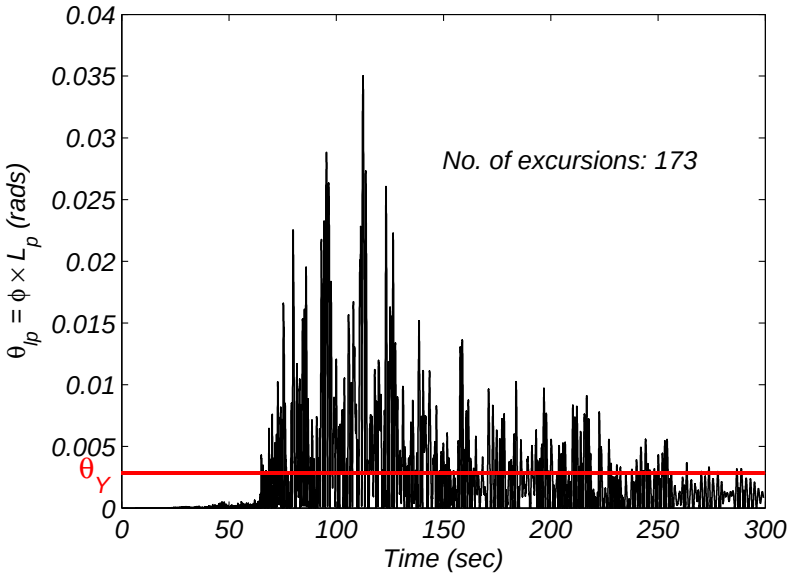

Figure 4.33 Effective plastic hinge rotation, θ_{lp}, for the Tohoku, Japan, AOMH1211 Station earthquake motion. The yield rotation, θ_Y, corresponds to the curvature at the point of first yield, ϕ_Y, of the moment-curvature analysis multiplied by the effective plastic hinge length.

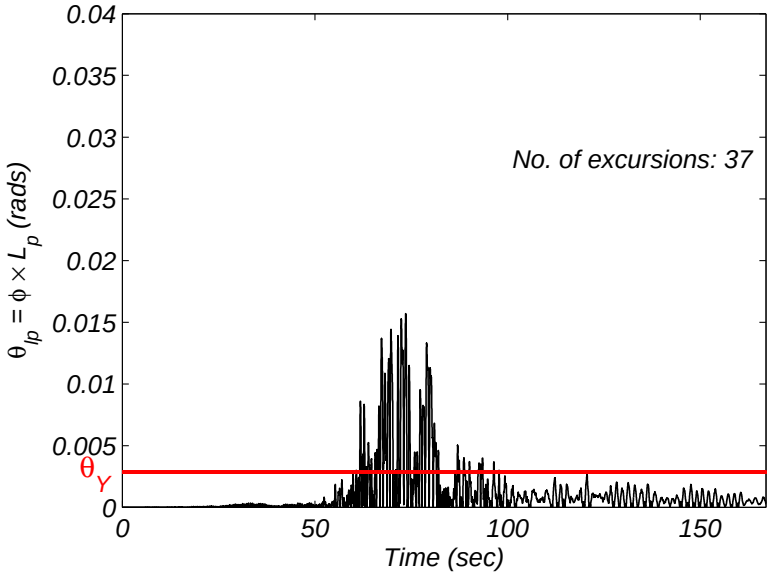

Figure 4.34 Effective plastic hinge rotation, θ_{lp}, for the Maule, Chile, Maipu Station earthquake motion. The yield rotation, θ_Y, corresponds to the curvature at the point of first yield, ϕ_Y, of the moment-curvature analysis multiplied by the effective plastic hinge length.

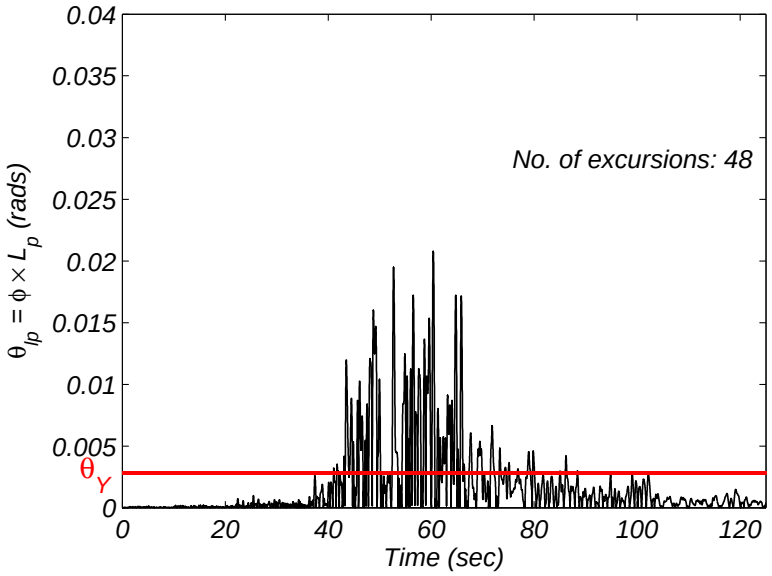

Figure 4.35 Effective plastic hinge rotation, θ_{lp}, for the Maule, Chile, Vina del Mar Station earthquake motion. The yield rotation, θ_Y, corresponds to the curvature at the point of first yield, ϕ_Y, of the moment-curvature analysis multiplied by the effective plastic hinge length.

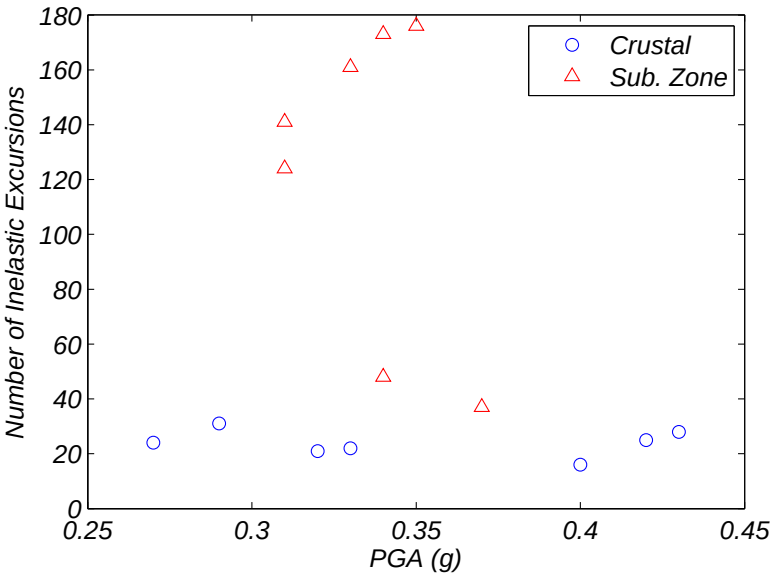

Figure 4.36 Peak ground acceleration for all earthquake motions relating to number of inelastic excursions

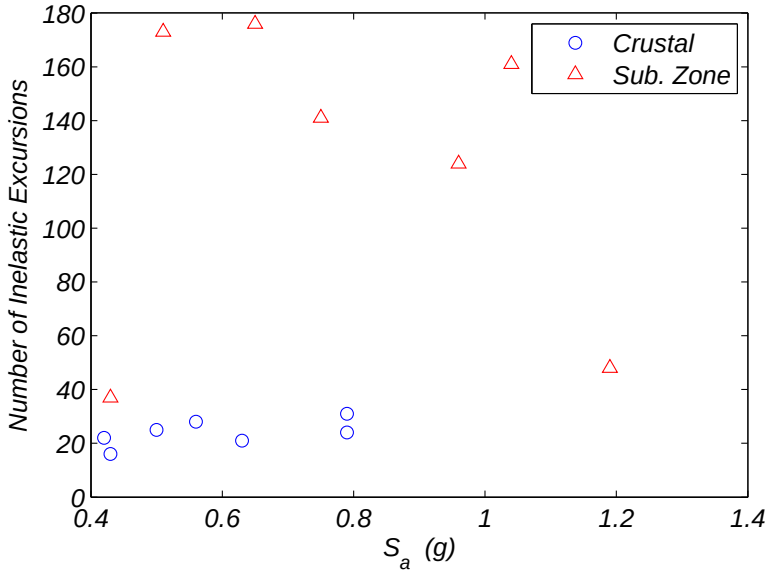

Figure 4.37 Pseudo-spectral acceleration for all earthquake motions relating to number of inelastic excursions

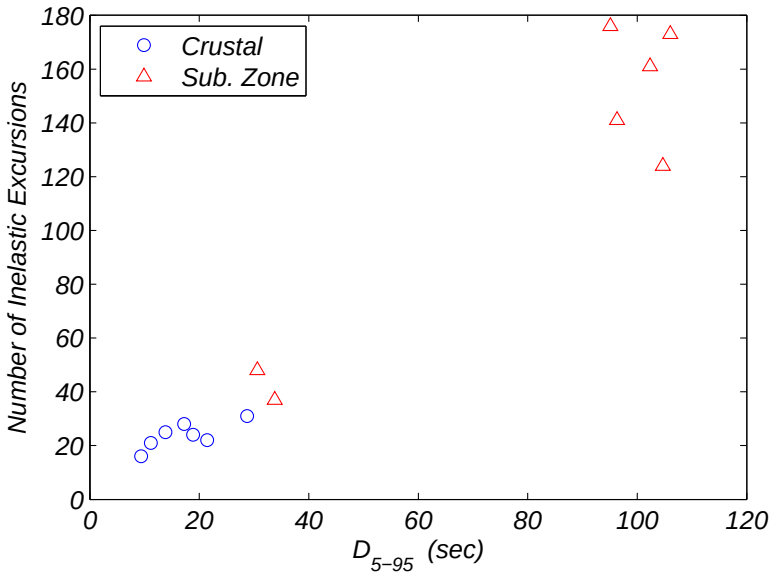

Figure 4.38 Significant duration for all earthquake motions relating to number of inelastic excursions

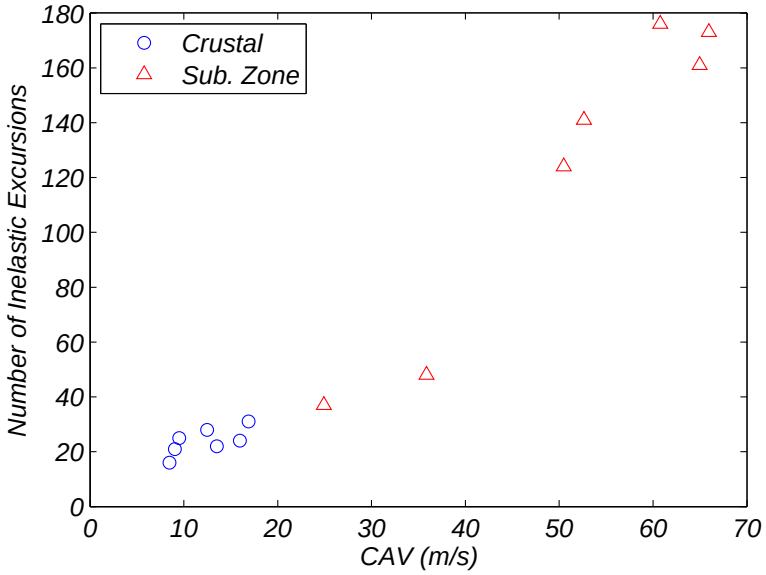

Figure 4.39 Cumulative absolute velocity for all earthquake motions relating to number of inelastic excursions

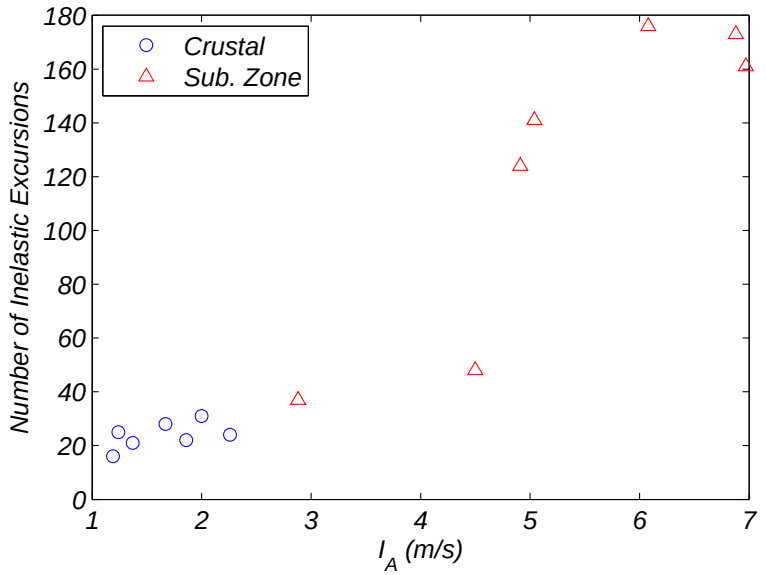

Figure 4.40 Arias intensity for all earthquake motions relating to number of inelastic excursions

Chapter 5 Conclusions

Historically, soil-foundation-bridge systems have not been designed for subduction zone earthquake motions. In the Pacific Northwest, where subduction zone earthquake motions are expected, many of the bridges have not been designed with any consideration of earthquake motion. As a consequence, many soil-foundation-bridge systems are seismically vulnerable, and this has enormous social and economic implications at local, regional, and national scales.

In this study, the primary goal was to develop an understanding of the effects of duration on the seismic response of a soil-foundation-bridge system. To accomplish this goal, a suite of fourteen earthquake motions was selected. Seven of the earthquake motions were from shallow, crustal seismic sources, such as those found prevalently in California. The other seven earthquake motions were from subduction zone sources (i.e. Japan and Chile). The earthquake motions were scaled so that their amplitudes and frequency contents were similar; thus, the distinguishing factor between the two types of earthquake motions was the duration. The subduction zone earthquake motions used had longer durations, as is typical, and this means that they had more cycles of loading.

Examining the results, it was found that the displacement, shear force, and bending moment versus depth profiles were similar when shallow, crustal or subduction zone earthquake motions were considered. In addition, the plastic hinging in the bridge column/pile occurred at nearly the same location (i.e. under the soil surface, $D/B \approx 3.0$), and, in some cases, plastic hinging was worse for the shallow, crustal earthquake motions than the subduction zone earthquake motions. This result is interesting, however, it is expected. The earthquake motions were scaled to have nearly the same amplitudes and frequency contents. The displacements, shear forces, and bending moments were not as sensitive to duration, because peak values were being examined.

When the number of inelastic excursions was examined, the effects of duration became more apparent. In this study, an inelastic excursion is defined as the exceedance of a normalized yielding curvature ductility. The number of inelastic excursions recorded during the subduction zone earthquake motions was on the order of four times greater than the number of inelastic excursions recorded during the shallow, crustal earthquake motions. This indicates that expected damage in the bridge columns, primarily due to low-cycle and extremely low-cycle fatigue, is expected to be much greater during the subduction zone earthquake motions. Further quantification of this effect is the topic of important future research.

The number of inelastic excursions was compared to earthquake motion intensity measures to start framing this problem within the performance-based earthquake engineering (PBEE) framework (Kramer, 2011). The earthquake motion intensity measures examined are peak ground acceleration (*PGA*), the spectral acceleration at the fundamental period of the soil-foundation-bridge system [$S_a(T_1)$], the significant duration (D_{5-95}), the Arias intensity (I_a), and the cumulative absolute velocity (*CAV*). It was found that *PGA* and $S_a(T_1)$ were poor indicators of the expected number of inelastic excursions caused by an earthquake motion, which was expected, because the ground motions were selected to have similar spectral acceleration values. D_{5-95}, I_a, and *CAV* were much better indicators. This is expected, because these three intensity measure implicitly (I_a and *CAV*) or explicitly (D_{5-95}) include the effects of earthquake motion duration. Fourteen earthquake motions are not enough to start drawing statistically significant distinctions regarding the sufficiency and efficiency of the chosen earthquake motion intensity measures for predicting the number of inelastic excursions. This will be the topic of a much larger future research program, as this work moves closer to completing the PBEE analysis, and finally predicting expected losses caused by subduction zone earthquake motions.

In the process of writing this report, other practical contributions were made, as outlined below:

- scripts for a working soil-foundation-bridge model were created in the finite element framework OpenSees, and these scripts are easily adaptable to consider other bridges, other soil types, other foundation types, and other earthquake motions;
- extensive MATLAB files were developed for post-processing of recorded response parameters, and these files can be easily adapted to consider other important cases, as highlighted in the previous bullet.

The work performed during this study opened many avenues for future research topics. Two potential topics have already been mentioned previously in this chapter (i.e. quantifying the effects of low-cycle fatigue on soil-foundation-bridge systems, and expanding this work to consider PBEE). Other potential future research topics are listed below, and it should be noted that this list is not exhaustive.

1. Selecting earthquake motions linearly scaled over a smaller period range by bracketing the first fundamental period of the soil-foundation-bridge system would further isolate the effects of duration by strengthening the earthquake motion selection process. The spectral acceleration value for the subduction zone median response spectrum is currently greater than the spectral acceleration value for the shallow, crustal median response spectrum by 0.2 g.
2. In realistic scenarios, the soil-foundation-bridge system will be subjected to both horizontal, vertical, and rotational accelerations during an earthquake event. Including the vertical components of the earthquake motions and analyzing the soil-foundation-bridge system with the combination of both components would provide a more complete understanding of the demands placed thereon.

3. A more sophisticated model would consider a non-homogeneous soil column and incorporate the effects of liquefaction and lateral spreading. Incorporating local (i.e. Willamette Valley) stratigraphy and strength parameters from lab tests into the model would provide meaningful results for local design engineers.

4. Development of additional soil-foundation-bridge models to account for variations in bridge stock would provide valuable information for local design engineers. Variations in bridge stock could include: number of bridge columns, column-deck connections, and abutment foundations and materials.

5. Conducting additional sensitivity analyses on soil and structural components would indicate which parameters have the greatest influence on the results and would improve computational efficiency (i.e. shorter run times).

6. Developing a 3D nonlinear model of soil and structural components could elucidate the limitations of 2D modeling related to the effects of duration on the soil-foundation-bridge system.

Bibliography

API American Petroleum Institute. *Recommended Practice for Planning, Designing and Construction Fixed Offshore Platforms*. American Petroleum Institute, Washington, DC., 1993.

R.D. Andrus, C.D. Fairbanks, J. Zhang, W.M. Camp, T.J. Casey, T.J. Cleary, and W.B. Wright. Shear-wave velocity and seismic response of near-surface sediments in Charleston, South Carolina. *Bulletin of the Seismological Society of America*, 96(5): 1897–1914, 2006.

A. Arias. Measure of earthquake intensity. Technical report, Massachusetts Inst. of Tech., Cambridge. Univ. of Chile, Santiago de Chile, 1970.

ASCE 7-10. *Minimum Design Loads of Buildings and Other Structures*. American Society of Civil Engineers, Reston, VA, 2010.

B. Aygün, L. Dueñas-Osorio, J.E. Padgett, and R. DesRoches. Efficient longitudinal seismic fragility assessment of a multispan continuous steel bridge on liquefiable soils. *Journal of Bridge Engineering*, 16(1):93–107, 2010.

J.W. Baker, T. Lin, S.K. Shahi, and N. Jayaram. *New Ground motion selection procedures and selected motions for the PEER transportation research program*. Pacific Earthquake Engineering Research Center, 2011.

André R Barbosa and Manuel AG Silva. Bridge abutment interaction under seismic loading. *2nd International Conference on Structural Condition Assessment, Monitoring and Improvement, Changsha, China*, pages 19–21, 2007.

R.L. Boroschek, V. Contreras, D.Y. Kwak, and J.P. Stewart. Strong ground motion attributes of the 2010 Mw 8.8 Maule, Chile, earthquake. *Earthquake Spectra*, 28(1):19–38, 2012.

R.W. Boulanger, C.J. Curras, B.L. Kutter, D.W. Wilson, and A. Abghari. Seismic soil-pile-structure interaction experiments and analyses. *Journal of Geotechnical and Geoenvironmental Engineering*, 125(9):750–759, 1999.

M.E. Bowers. *Seismic fragility curves for a typical highway bridge in Charleston, SC considering soil-structure interaction and liquefaction effects*. PhD thesis, Clemson University, 2007.

S.J. Brandenberg, R.W. Boulanger, B.L. Kutter, and D. Chang. Behavior of pile foundations in laterally spreading ground during centrifuge tests. *Journal of Geotech. and Geoenv. Engng*, 131(11):1378–1391, 2005.

M.M. Chiaramonte. An analysis of conventional and improved marginal wharves. Master's thesis, University of Washington, 2011.

A.K. Chopra. *Dynamics of structures: Theory and applications to earthquake engineering*, volume 4. Prentice Hall Saddle Riverˆ eNY NY, 2012.

M. Ciampoli and P.E. Pinto. Effects of soil-structure interaction on inelastic seismic response of bridge piers. *Journal of structural engineering*, 121(5):806–814, 1995.

R.D. Cook, D.S. Malkus, M.E. Plesha, and R.J. Witt. *Concepts and applications of finite element analysis*. Wiley, New York, 2002.

A. Elgamal, Z. Yang, and E. Parra. Computational modeling of cyclic mobility and post-liquefaction site response. *Soil Dynamics and Earthquake Engineering*, 22(4):259–271, 2002.

F.C. Filippou, V.V. Bertero, and E.P. Popov. *Effects of bond deterioration on hysteretic behaviour of reinforced concrete joints*. University of California, Berkeley, California, 1983.

National Research Institute for Earth Science and Disaster Prevention. Strong-motion seismograph networks (k-net,kik-net), 2012. URL `http://www.k-net.bosai.go.jp/`.

M.M. Karthik and J.B. Mander. Stress-block parameters for unconfined and confined concrete based on a unified stress-strain model. *Journal of Structural Engineering*, 137(2): 270–273, 2010.

E. Kausel. Early history of soilstructure interaction. *Soil Dynamics and Earthquake Engineering*, 30(9):822–832, 2010.

D.C. Kent and R. Park. Flexural members with confined concrete. *Journal of the Structural Division*, 97(7):1969–1990, 1971.

A. Khosravifar. *Analysis and design for inelastic structural response of extended pile shaft foundations in laterally spreading ground earthquakes*. PhD thesis, University of California, Davis, 2012.

A. Kottke and E.M. Rathje. A semi-automated procedure for selecting and scaling recorded earthquake motions for dynamic analysis. *Earthquake Spectra*, 24(4):911–932, 2008.

S.L. Kramer. *Geotechnical earthquake engineering*, volume 1. Prentice-Hall Civil Engineering and Engineering Mechanics Series, Upper Saddle River, NJ: Prentice Hall,—c1996, 1996.

S.L. Kramer. Performance-based design in geotechnical earthquake engineering practice. In *Fifth International Conference on Earthquake Geotechnical Engineering*, volume 1, 2011.

E.L. Krinitzsky and F.K. Chang. *Parameters for Specifying Intensity-Related Earthquake Ground Motions*. Department of the Army, Waterways Experiment Station, Corps of Engineers, 1987.

Advanced Civil Engineering Materials Research Lab. Ace-mrl, university of michigan, June 2013. URL $http://ace-mrl.engin.umich.edu/NewFiles/seis_project_ecc.html$.

J.B. Mander, N. Priestley, and R. Park. Theoretical stress-strain model for confined concrete. *Journal of structural engineering*, 114(8):1804–1826, 1988.

H. Matlock. Correlations for design of laterally loaded piles in soft clay. In *Offshore Technology in Civil Engineering's Hall of Fame Papers from the Early Years*, pages 77–94. ASCE, 1970.

F. McKenna, G.L. Fenves, and M.H. Scott. Open system for earthquake engineering simulation. *Pacific Earhtquake Engineering Research Center*, 2000.

M. Menegotto and P.E. Pinto. Method of analysis of cyclically loaded R. C. frames including changes in geometry and nonelastic behavior of elements under combined normal force and bending moment. In *International Association for Bridge and Structural Engineers Proceedings*, 1973.

R.L. Mosher. Load-transfer criteria for numerical analysis of axially loaded piles in sand. *Final Report Army Engineer Waterways Experiment Station, Vicksburg, MS.*, 1, 1984.

J.R. Murphy and L.J. O'Brien. The correlation of peak ground acceleration amplitude with seismic intensity and other physical parameters. *Bulletin of the Seismological Society of America*, 67(3):877–915, 1977.

G. Mylonakis and G. Gazetas. Seismic soil-structure interaction: beneficial or detrimental? *Journal of Earthquake Engineering*, 4(03):277–301, 2000.

A. Neuenhofer and F.C. Filippou. Geometrically nonlinear flexibility-based frame finite element. *Journal of Structural Engineering*, 124(6):704–711, 1998.

California Department of Transportation. Memorandum, humboldt bay middle channel bridge. Technical report, 2000.

California Department of Transportation. Seismic design criteria. Technical report, 2006.

D. Park and Y.M.A. Hashash. Soil damping formulation in nonlinear time domain site response analysis. *Journal of Earthquake Engineering*, 8(02):249–274, 2004.

T. Paulay and M.J.N. Priestly. *Seismic design of reinforced concrete and masonry buildings*. Wiley Online Library, 1992.

M. Power, B. Chiou, N. Abrahamson, Y. Bozorgnia, T. Shantz, and C. Roblee. An overview of the NGA project. *Earthquake Spectra*, 24(1):3–21, 2008.

M.J.N. Priestley and R. Park. Strength and ductility of concrete bridge columns under seismic loading. *ACI Structural Journal*, 84(1):61–76, 1987.

L.C. Reese and M.W. O'Neill. *Drilled shafts: Construction procedures and design methods*. Prepared for US Department of Transportation, Federal Highway Administration, Office of Implementation, 1975.

Lymon C. Reese, William R. Cox, and Francis D. Koop. Analysis of laterally loaded piles in sand. In *Offshore Technology in Civil Engineering Hall of Fame Papers from the Early Years*, pages 95–105, 1974.

D. Resendiz and J.M. Roesset. Soil-structure interaction in Mexico City during the 1985 Earthquake. In *Proc. of Int'l. Conf. on The Mexico Earthquakes - 1985, ASCE*, volume Factors Involved and Lessons Learned, pages 193–203, 1987.

B.D. Scott, R. Park, and M.J.N. Priestley. Stress-strain behavior of concrete confined by overlapping hoops at low and high strain rates. In *ACI Journal Proceedings*, volume 79. ACI, 1982.

M.H. Scott and G.L. Fenves. Krylov subspace accelerated newton algorithm: application to dynamic progressive collapse simulation of frames. *Journal of Structural Engineering*, 136(5):473–480, 2009.

H.B. Seed. Design problems in soil liquefaction. *Journal of Geotechnical Engineering*, 113(8):827–845, 1987.

H.B. Seed, M.P. Romo, J.I. Sun, A. Jaime, and J. Lysmer. The Mexico Earthquake of September 19, 1985-relationships between soil conditions and earthquake ground motions. *Earthquake Spectra*, 4(4):687–729, 1988.

A. Shamsabadi, K.M. Rollins, and M. Kapuskar. Nonlinear soil–abutment–bridge structure interaction for seismic performance-based design. *Journal of Geotechnical and Geoenvironmental Engineering*, 133(6):707–720, 2007.

P.G. Somerville, N.F. Smith, R.W. Graves, and N.A. Abrahamson. Modification of empirical strong ground motion attenuation relations to include the amplitude and duration effects of rupture directivity. *Seismological Research Letters*, 68(1):199–222, 1997.

M.D. Trifunac and A.G. Brady. On the correlation of seismic intensity scales with the peaks of recorded strong ground motion. *Bulletin of the Seismological Society of America*, 65 (1):139–162, 1975.

V.N. Vijayvergiya. Load-movement characteristics of piles. In *Ports'77. 4 th annual symposium of the American Society of Civil Engineers, Waterway, Port, Coastal and Ocean Division, Long Beach, California, v. 2*, pages 269–284, 1977.

S.D. Werner, J.L. Beck, and M.B. Levine. Seismic response evaluation of Meloland Road Overpass using 1979 Imperial Valley Earthquake records. *Earthquake Engineering and Structural Dynamics*, 15:249–274, 1987.

S.D. Werner, J.L. Beck, and A. Nisar. Dynamic tests and seismic excitation of a bridge structure. In *Proceedings of the Fourth U.S. National Conference on Earthquake Engineering, Palm Springs, EERI, California*, 1990.

S.D. Werner, C.B. Crouse, L.S. Katatfygiotis, and J.L. Beck. Use of strong motion records for model evaluation and seismic analysis of a bridge structure. In *Proceedings of the Fifth U.S. National Conference on Earthquake Engineering, Chicago, EERI, California*, 1994.

J.C. Wilson and B.S. Tan. Bridge abutments: assessing their influence on earthquake response of meloland road overpass. *Journal of Engineering Mechanics*, 116(8):1828–1837, 1990a.

J.C. Wilson and B.S. Tan. Bridge abutments: assessing their influence on earthquake response of meloland road overpass. *Journal of Engineering Mechanics*, 116(8):1838–1856, 1990b.

Z. Yang. *Numerical modeling of earthquake site response including dilation and liquefaction*. PhD thesis, University of California at San Diego, Dept. of Structural Engineering, 2000.

M.H.M. Yassin. *Nonlinear Analysis of Prestressed Concrete Structures under Monotonic and Cycling Loads*. PhD thesis, University of California, Berkeley, 1994.

Y. Zhang, Z. Yang, J. Bielak, J.P. Conte, and A. Elgamal. Treatment of seismic input and boundary conditions in nonlinear seismic analysis of a bridge ground system. In *16th ASCE Engineering Mechanics Conference*, pages 16–18, 2003.

Y. Zhang, J.P. Conte, Z. Yang, A. Elgamal, J. Bielak, and G. Acero. Two-dimensional nonlinear earthquake response analysis of a bridge-foundation-ground system. *Earthquake Spectra*, 24(2):343–386, 2008.

APPENDIX

Column C1 Spiral Design:

This Mathcad script is for column C1, however the equations and design process are identical for all experimental test columns.

Need to check value according to instructions highlighted.

Input Values.

Step 1.) Adjust input values according to the column properties and loading conditions

Material Properties:

Maximum size aggregate. $MSA := 0.75in$

Diameter of longitudinal reinforcing steel. $D_{bl} := 1.25in$

Nominal concrete compressive strength. $f'_c := 4000psi$

Diameter of transverse reinforcing steel. $D_{bt} := 0.625in$

Yield stress of transverse reinforcement. $f_{yt} := 60ksi$

Cross-sectional area of transverse steel. $A_{st} := 0.30in^2$

Moment over strength factor. $\lambda := 1.4$

Column Properties:

Diameter of column. $D_c := 43in$

Column height. $h_c := 20ft$

Column clear cover. $c_c := 2.5in$

Effective web width. $b_v := 43in$

Number of spirals within column. $n := 1$

Loading Conditions:

Strength reduction factor defined by ODOT Sec. 5.5.4.2.1. $\phi := 0.75$

Prestressing force resisting shear. $V_p := 0kip$

Expected moment capacity. $M_e := 4159kip \cdot ft$

Applied axial load on column. $P := 783kip$

Global displacement ductility demand ratio. $\mu_D := 4$

Step 2.) Determine the shear force demand according to AASHTO LRFD Bridge Design Specifications 6th Ed. Sec. 5.8.2.9

$D_r := D_c - 2\cdot\left[c_c + D_{bt} + \left(\frac{D_{bl}}{2}\right)\right] = 35.5\cdot in$ — Diameter of the core, taken from center-to-center of the longitudinal reinforcement.

$d_e := \left(\frac{D_c}{2}\right) + \left(\frac{D_r}{\pi}\right) = 32.8\cdot in$ — Defined by AASHTO 2012 C5.8.2.9-2.

$d_v := 0.9\cdot d_e = 29.52\cdot in$ — Effective shear depth.

$V_e := \frac{M_e}{h_c} = 207.9\cdot kip$ — Expected peak shear force.

$V_n := \frac{V_e}{\lambda} = 148.5\cdot kip$ — Nominal shear force.

$V_u := \phi\cdot V_n = 111.4\cdot kip$ — Factored shear force.

$v_u := \frac{\left|V_u - \phi\cdot V_p\right|}{\phi\cdot b_v\cdot d_v} = 0.117\cdot ksi$ — Shear stress on the concrete section.

$A_g := \left(\frac{\pi}{4}\right)\cdot D_c^{\,2} = 1.45\times 10^3\cdot in^2$ — Gross cross-sectional area of column.

$V_{uA} := v_u\cdot A_g = 169.9\cdot kip$ — Factored shear force defined by AASHTO.

Step 3.) Determine the maximum and minimum spiral spacing/pitch according to the applicable AASHTO code requirements

Note that according to AASHTO 2012 Sec. 5.10.6.2, spiral reinforcement shall consist of one or more evenly spaced continuous spirals of either deformed or plain bar or wire with a minimum diameter of 0.375 in. Therefore the limits for maximum and minimum spiral reinforcing spacing/pitch for the plastic hinge zone will be applied to the entire length of the column.

$Check\_diameter\_of\_deformed\_bar := \max\left(D_{bt}, 0.375in\right) = 0.625\cdot in$

If the above value is less than 0.375 in, then select a larger bar size for the spiral reinforcement.

A.) Maximum and minimum spiral spacing/pitch according to AASHTO LRFD Bridge Design Specifications 6th Ed Sec. 5.10.6.2

Minimum clear spacing is equal to the lesser of one inch or 1.33 multiplied by the maximum size aggregate.

$c_{smin} := \max(1.0in, 1.33 \cdot MSA) = 1 \cdot in$ Minimum clear spacing of spiral for part A.

$s_{minA} := c_{smin} + D_{bt} = 1.63 \cdot in$ Minimum spiral spacing/pitch for part A.

$s_{maxA} := \min\left(6.0in, 6.0 \cdot D_{bl}\right) = 6 \cdot in$ Maximum spiral spacing/pitch for part A.

B.) Determine the maximum spiral spacing/pitch according to AASHTO LRFD Bridge Design Specifications 6th Ed Sec. 5.8.2.7

$v_u = 0.117 \cdot ksi$ $0.125 \cdot f'_c = 0.5 \cdot ksi$

$s_{maxB1} := \min\left(0.8d_v, 24in\right) = 23.62 \cdot in$ If $v_u < 0.125*f'_c$

$s_{maxB2} := \min\left(0.4d_v, 12in\right) = 11.81 \cdot in$ If $v_u >= 0.125*f'_c$

If $v_u < 0.125*f'_c$ set $s_{maxB} = s_{maxB1}$ if not set equal to s_{maxB2}

$s_{maxB} := s_{maxB1} = 23.62 \cdot in$

C.) Determine the maximum spacing/pitch according to AASHTO LRFD Bridge Design Specifications 6th Ed Sec. 5.7.4.6

$D_{cc} := D_c - 2 \cdot c_c = 38 \cdot in$ Diameter of core, measure out-to-out of spiral.

$A_c := \frac{\pi \cdot D_{cc}^2}{4} = 1.13 \times 10^3 \cdot in^2$ Area of core measured to the outside diameter of the spiral.

$min\_C\_\rho_t := 0.45\left[\left(\frac{A_g}{A_c}\right) - 1\right]\left(\frac{f'_c}{f_{yt}}\right) = 0.008$ Eq. 5.7.4.6-1 for general conditions.

$s_{maxC} := 4 \cdot \frac{A_{st}}{D_{cc} \cdot min\_C\_\rho_t} = 3.75 \cdot in$

D.) Determine the maximum spacing/pitch according to AASHTO LRFD Bridge Design Specifications 6th Ed Sec. 5.10.11.4.1d

$$min\_D\_\rho_t := 0.12\left(\frac{f'_c}{f_{yt}}\right) = 0.008$$

Eq. 5.10.11.4.1d-1 for confinement of plastic hinge zones for seismic zones 3 and 4.

$$s_{maxD} := 4\cdot\frac{A_{st}}{D_{cc}\cdot min\_D\_\rho_t} = 3.95\cdot in$$

E.) Determine the maximum spacing/pitch according to AASHTO LRFD Bridge Design Specifications 6th Ed Sec. 5.8.2.5

$$A_v := n\cdot\left(\frac{\pi}{2}\right)\cdot A_{st} = 0.47\cdot in^2$$

Area of shear reinforcement perpendicular to flexural tension reinforcing.

$$s_{maxE} := \frac{\left(f_{yt}\cdot A_v\right)}{\left(0.0316\cdot\sqrt{psi\cdot f'_c}\cdot b_v\right)} = 329.008\cdot in$$

F.) Determine the maximum spacing/pitch according to AASHTO LRFD Bridge Design Specifications 6th Ed Sec. 5.10.11.4.3

$$s_{maxF} := \min\left(4in, \frac{D_c}{4}\right) = 4\cdot in$$

G.) Determine the maximum spacing/pitch according to AASHTO ASHTO Guide Specifications for LRFD Seismic Bridge Design 2nd Ed. Sec. 8.6.5

$$min\_G\_\rho_t := .005$$

Eq. 8.6.5-3

$$s_{maxG} := 4\cdot\frac{A_{st}}{D_{cc}\cdot min\_G\_\rho_t} = 6.32\cdot in$$

H.) Determine the maximum spacing/pitch according to AASHTO ASHTO Guide Specifications for LRFD Seismic Bridge Design 2nd Ed. Sec. 8.8.9

$$s_{maxH} := \min\left(6\cdot D_{bl}, 6in, \frac{D_c}{5}\right) = 6\cdot in$$

I.) Determine the controlling maximum and minimum spiral spacing/pitch from steps A. through H

$s_{min} := s_{minA} = 1.63 \cdot in$

$s_{max} := \min\left(s_{maxA}, s_{maxB}, s_{maxC}, s_{maxD}, s_{maxE}, s_{maxF}, s_{maxG}, s_{maxH}\right) = 3.75 \cdot in$

Step 4.) Calculate V_c according to AASHTO Guide Specifications for LRFD Seismic Bridge Design 2nd Ed. Sec. 8.6.2

guess_s := 3.75in Use the maximum spacing and adjust until the final spacing and this guess are the same value.

$D' := D_c - 2 \cdot c_c - D_{bt} = 37.38 \cdot in$ Cross-section dimension of the confined concrete core measure between the centerline of the spiral.

$guess\_\rho_{st} := 4 \cdot \frac{A_{st}}{guess\_s \cdot D'} = 0.009$ Eq. 8.6.2-6

$A_e := 0.8 \cdot A_g = 1.16 \times 10^3 \cdot in^2$ Eq. 8.6.2-2

$f_s := guess\_\rho_{st} \cdot f_{yt} = 0.514 \cdot ksi$ Eq. 8.6.2-6

$\mu_D = 4$ Determined in Sec. 4.9 as the maximum value for a multiple-column bent.

$\alpha' := \left(\frac{f_s}{0.15ksi}\right) + 3.67 - \mu_D = 3.1$ Eq. 8.6.2-5

$v_c := \min\left[.11 \cdot \sqrt{ksi \cdot f'_c}, 0.047 \cdot \alpha' \cdot \sqrt{ksi \cdot f'_c}, 0.032 \sqrt{ksi \cdot f'_c} \cdot \alpha' \cdot \left[1 + \left(\frac{P \cdot in^2}{2 \cdot A_g \cdot kip}\right)\right]\right] = 220\,psi$

$V_c := \frac{\left(v_c \cdot A_e\right)}{2} = 127.8 \cdot kip$ Eq. 8.6.2-1

The above equation is divided by 2 according to AASHTO LRFD Bridge Design Specifications 6th Ed Sec. 5.10.11.4.1c, since the compression force is equal to 0.05 f'_c A_g which is half the limit.

Step 5.) Calculate the maximum allowed V_s according to AASHTO Guide Specifications for LRFD Seismic Bridge Design 2nd Ed. Sec. 8.6.4

$max\_V_s := 0.25 \cdot A_e \cdot \sqrt{ksi \cdot f'_c} = 580.9 \cdot kip$ Eq. 8.6.4-1

Step 6.) Calculate V_s according to AASHTO Guide Specifications for LRFD Seismic Bridge Design 2nd Ed. Sec. 8.6.1 and check against the maximum shear reinforcement calculated in step 5.)

$V_s := \left(\frac{V_{uA}}{0.9}\right) - V_c = 61 \cdot kip$ Rearranging Eq. 8.6.1-1 and Eq. 8.6.1-2 to solve for V_s

$Check\_V_s := V_s - max\_V_s = -519.9 \cdot kip$ If this value is greater than zero try a smaller spacing/pitch for the initial guess.

Step 7.) Calculate the required spacing/pitch according to AASHTO Guide Specifications for LRFD Seismic Bridge Design 2nd Ed. Sec. 8.6.3

$s_{req} := \frac{\left[\left(\frac{\pi}{2}\right) \cdot n \cdot A_{st} \cdot f_{yt} \cdot D'\right]}{V_s} = 17.32 \cdot in$ Rearranged Eq. 8.6.3-1 to solve for s.

Step 8.) Determine the final spacing/pitch to be used over the entire height of the column and the corresponding transverse reinforcement ratio.

$s_{min} = 1.63 \cdot in$ $s_{max} = 3.75 \cdot in$ $s_{req} = 17.32 \cdot in$ $pitch := 3.25in$

The final spacing/pitch will be set at 3.25 inches to produce a constructible design.

$\rho_t := \frac{\left(4 \cdot A_{st}\right)}{\left(pitch \cdot D_{cc}\right)} = 0.01$ Ratio of spiral reinforcement to total volume of concrete core, measured out-to-out of spirals.